11-1-2012

# Lamination of Inverted Organic Photovoltaics and Associated Physical Properties

Brian A. Bailey
*University of Denver*

# LAMINATION OF INVERTED ORGANIC PHOTOVOLTAICS AND ASSOCIATED PHYSICAL PROPERTIES

_____

A Dissertation

Presented to

the Faculty of Natural Sciences and Mathematics

University of Denver

_____

In Partial Fulfillment

of the Requirements for the Degree

Doctor of Philosophy

_____

by

Brian A. Bailey

November 2012

Advisor: Sean Shaheen

Author: Brian A. Bailey
Title: LAMINATION OF INVERTED ORGANIC PHOTOVOLTAICS AND ASSOCIATED PHYSICAL PROPERTIES
Advisor: Sean Shaheen
Degree Date: November 2012

**Abstract**

This dissertation is the result of a series of studies involving hot press lamination of inverted organic photovoltaics. It first gives background and develops a lamination process for fabrication. Then, the process is used to answer fundamental questions about organic photovoltaics and to fabricate previously impossible or overly complicated devices. Finally, the author examines the scientific theory which describes the process and aligns that theory with related measurements.

The field of organic photovoltaics is introduced and the lamination process is developed and optimized. In the lamination process, part of the solar cell is deposited onto a rigid substrate, and the rest is deposited onto a flexible one. The two substrates are pressed together under heat to complete the device. Laminated devices are shown to perform as well or better than those made with standard fabrication methods, and the process shows benefits to both large scale production and scientific exploration of OPV devices.

The lamination process is then used to answer physical questions and solve problems related to OPV. After diversifying the procedure to include lamination at either the electron or hole contact, a series of semitransparent electrode materials are integrated into devices. These materials are difficult or impossible to integrate into inverted devices without lamination. Then bare metal

contacts are pretreated and laminated into devices in order to investigate the mechanisms for time evolution in inverted devices. Finally, two active layers are laminated to make a tandem device. It is shown that the performance of the tandem is limited not by the procedure, but by the materials used in the interconnect layer between the two subcells.

An investigation is performed that explores the physics behind the basis of lamination: adhesion. Different mechanisms of adhesion are proposed, and calculations of adhesion forces based on known materials properties are made. The resulting range of calculated forces is quite large, but within the range of measured values for adhesion force. A general picture of the physics involved in lamination processes and their adhesion forces emerges.

**Acknowledgements**

Thank you to Dr. Art Frank and his lab for the use of their hydraulic lamination press. That piece of equipment has been crucial to this work. Thank you to Dr. Sarah Cowan, Dr. Matt Beard, Dr. Josh Holt, Dr. Ocatavi Semonin, Dr. Joseph Luther and Dr. Jao Van de Lagemaat for use of their optical model program. Thank you to my advisors at the University of Denver, and at the National Renewable Energy Lab. Dr. Sean Shaheen and Dr. Nikos Kopidakis have always been available and helpful at every step of my graduate research. Dr. Dana Olson and Dr. Joe Berry are responsible for my early development at NREL, and have put up with a plethora of inquiries and questions since. Dr. Jeff Blackburn and Dr. Brian A. Larsen produced and characterized SWCNT and AgNW films that were made into electrodes, and have shared wisdom and information. Dr. Teresa Barnes was patient and helpful with my many requests and favors. Dr. Matthew Reese has been more of a mentor than a coworker, and has given lots of his time to teaching me anything I was willing to ask about. Dr. Scott Hammond has been in the unfortunate position of having work similar to mine, but with more knowledge; and as a result has fielded constant requests for help in many areas. Alex Dixon made all of the AFM images used in this work. Nicodemus Edwin Widjonarko, Aj Sigdel, Dr. Sarah Cowan, Dr. Paul Ndione, Dr. Jao van de Lagemaat, Dr. Brian Gregg, Dr. Octavi Semonin, Dr. Jianbo Gao, Dr. Joseph Luther, Dr. Jeremy Bergeson, Robert Nawrocki and Dr. Brad MacLeod have all contributed significantly. Finally, I would like to thank my wife Michelle for her unending support and understanding in this and all of my endeavors.

## Table of Contents


Chapter 1. Introduction to Organic Photovoltaics 1
1.1 Organic Photovoltaics Background 1
1.2. Characterization of Photovoltaic Devices 3
1.3. Physics of Organic Photovoltaics 7
1.3.1. Excitonic Systems and Charge Generation 7
1.3.2. The Bulk Heterojunction 11
1.3.3. Inverted vs. Traditional Geometry 13
1.3.4. Contacts and Transport Layers 16
1.4. Motivation for Lamination 19
1.5. Tandem OPV 21
1.5.1. Optical Modeling 23
1.6. Dissertation Outline 25

Chapter 2. Hot Press Lamination 27
2.1. Introduction 27
2.2. Background & Motivation 28
2.3. Experimental 29
2.4. Results and Discussion 31
2.5. Conclusions 39

Chapter 3. Transparent Back Electrodes and Alternative Adhesives 40
3.1 Introduction 40
3.1.1. Lamination Without PEDOT:PSS 44
3.1.2. PEDOT:PSS as a Transparent Electrode 44
3.1.3. Single Walled Carbon Nanotubes 46
3.1.4. Silver Nanowires 47
3.2. Experimental 48
3.3. Results and Discussion 50
3.3.1. D-Sorbitol as an Adhesive Layer for solid Ag Film Electrodes 50
3.3.2. PEDOT:PSS:d-Sorbitol Electrodes 52
3.3.3. Single Walled Carbon Nanotube Electrodes 53
3.3.4. Silver Nanowire PEDOT:PSS Hybrid Electrodes 55
3.4. Comparisons, and Conclusions General to All Contacts 57

Chapter 4. Contact Evolution 61
4.1. Introduction 61
4.2. Background 62
4.3. Experimental 64

4.4. Results 65
4.5. Conclusions 70

Chapter 5. Laminated Tandems 72
5.1. Introduction 72
5.2. Experimental 74
5.3. Results and Discussion 78
5.4. Conclusions 84

Chapter 6. Adhesion at the Laminated Interface 86
6.1. Introduction 86
6.2. Background Information 87
6.2.1. Lamination Interface Background 87
6.2.2. Dipole - Dipole Bonding 88
6.2.3. Van der Waals interactions 90
6.3. Macroscopic Delamination Force Measurement 91
6.4. Bonding Mechanisms between Lamination Interfaces 93
6.4.1. P3HT Packing and Surface Density 94
6.4.2. Minimum Separation Distance 96
6.4.3. Keesom Force Calculation 97
6.4.4. Debye and London Dispersion Force Calculation 101
6.5. Adhesion Force from Surface Tension and Contact Angles 103
6.6. Conclusions 104

Bibliography 107

Appendix A: Tips, Tricks, Superstitions, Unfinished and Supplemental Work 117

## List of Figures


Figure

1.2.1. Explanation of J-V curves, $V_{oc}$, $J_{sc}$, $\eta$, and *FF* 4

1.2.2. The solar spectrum at the surface of the earth 7

1.3.1.1 Chemical structures of P3HT, ICBA and PCBM 11

1.3.3.1. Current flow and band structure of traditional and inverted OPV 14

1.3.3.2. *J-V* of optimized traditional and inverted geometry devices 16

1.3.4.1. Chemical structures for PEDOT and PSS 17

1.4.1. Basic structure of the lamination process 20

1.5.1. Energy Level Diagram depicting the motivation for tandem OPV 21

2.3.1. Laminated device structure 30

2.4.1. *J-V* of devices made by lamination vs evaporated ones 32

2.4.2. EQE of laminated OPV, verifying $J_{sc}$ 33

2.4.3. *J-V* of devices with various layers at the lamination interface 36

2.4.4. Performance of pre-lamination treatments on the PEDOT interlayer 38

3.1.1. (A) The lamination process
(B) Device geometry of ITO racetrack and six finger pattern
(C) Bus bar pattern 42

3.3.1.1. *J-V* of adhesive layers made from water, d-sorbitol, and IPA 51

3.3.2.1. (A) *J-V* of PEDOT:PSS as a transparent contact
(B) Optical transmission of PEDOT:PSS 53

3.3.3.1. (A) *PV* performance of devices with SWCNT contacts
(B) AFM images of SWCNT films with and without PEDOT:PSS
(C) Optical transmission of an OPV device with SWCNT back contact 55

3.3.4.1. (A) *PV* performance of devices with Ag NW contacts
(B) AFM images of bare NW film and one coated with PEDOT:PSS
(C) Resistivity vs. transparency and optical transmission for Ag NWs 56

4.2.1. Energy Levels of Silver and Silver Oxide 63

4.2.2. Time evolution of devices with Ag contacts compared to PEDOT:PSS 64

4.3.1. Various device structures used in the contact evolution study 65

4.4.1. *J-V* comparison of different electrodes used 66

4.4.2. *J-V* of old Ag, New Ag, and $Ag_xO$ contacts are indistinguishable 68

4.4.3. Work functions of the electrodes used 69

4.4.4. The measured work function of Ag changes in air 70

5.2.1. Structure and ordering of layers in devices made in this work 78
(A) Standard inverted single junction
(B) Tandem Structure
(C) Single junction cell with an ICL with DEZ grown on PEDOT
(D) Single junction cell with an ICL with DEZ grown on top of Ag

5.3.1. *J-V* curves for single junction cells 80

5.3.2. (A) Photoluminescence of ZnO NPs and ZnO formed from DEZ 81
(B) Band structure of ZnO NPs showing the location and approximate width of the defect state

5.3.3. Calculated $J_{sc}$ vs. Active layer thickness via optical absorption modeling compared to actual $J_{sc}$ data from various active layer thicknesses 82

5.3.4. Predicted short circuit currents in a tandem junction device 83

5.3.5. *J-V* curves of tandem devices 84

6.1.1. Chemical structures of P3HT, ICBA, PCBM, and d-sorbtiol 87

6.2.1.1. Lamination structures which produce efficient PV devices 89

6.2.2.1. Hydrogen bonding between water molecules 91

6.3.1. Cartoon of delamination apparatus 92

6.3.2. Representative Force vs. Time curves for delamination tests 92

6.4.1.1. Lamellar stacking structure of P3HT 96

## List of Tables

Table

2.4.1. Performance characteristics of laminated contact devices compared to evaporated contact ones 33

3.3.1.1. Properties of devices made with d-sorbitol as a contact adhesive 52

3.3.4.1. Characteristics and device properties for semitransparent electrodes with different treatments 59

4.4.1. Peak performance characteristics of device contacts 67

5.2.1. Performance characteristics of P3HT:PCBM and P3HT:ICBA single junction cells 76

5.3.1. Performance characteristics of devices explored in tandem work 84

6.3.1. Delamination force statistics for 10 devices of area 1 $cm^2$ 93

6.4.1.1. Properties of the simple cubic unit cell of a P3HT crystal 97

6.4.3.1. Pauling electronegativity differences of relevant elements showing the polar component of each bond 98

6.4.3.2. Estimated surface energy of hydrogen bonds between water molecules and dipole bonds between water and thiophene sulfur 102

6.4.4.1. Representative surface energies and forces of induced van der Waals interactions at various separation distances 103

## List of Abbreviations

| | |
|---|---|
| AgNW | Silver Nanowire |
| BHJ | Bulk Heterojunction |
| BIPV | Building Integrated Photovoltaics |
| CMC | Carboxylmethylcellulose |
| CT state | Charge Transfer State |
| DEZ | Diethylzinc |
| ETL | Electron Transport Layer |
| EQE | External Quantum Efficiency |
| HTL | Hole Transport Layer |
| *FF* | Fill Factor |
| HOMO | Highest Occupied Molecular Orbital |
| ICBA | Indene-$C_{60}$ bisadduct |
| ICL | Interconnect Layer |
| IPA | Isopropyl alcohol (also isopropanol) |
| ITO | Indium Doped Tin Oxide |
| $J_{sc}$ | Short Circuit Current |
| *J-V* | Current Density - Voltage |
| LUMO | Lowest Unoccupied Molecular Orbital |
| NP | Nanoparticle |
| NW | Nanowire |
| OPV | Organic Photovoltaics |
| P3HT | Poly(3-hexylthiophene) |
| PEDOT | Polyethylene dioxythiophene |
| PET | Polyethylene terephthalate |
| PEN | Polyethelyne napthalate |
| PCBM | [6,6]-phenyl-C-61-butyric acid methyl ester |
| PCE | Power Conversion Efficiency |
| PCDTBT | Poly[N-900-hepta-decanyl- 2,7-carbazole-alt-5,5-(40 ,70 -di-2-thienyl-20 ,10 ,30 -benzothia- diazole)] |
| PCPDTBT | Poly[2,6-(4,4-bis(2-ethylhexyl)-4H-cyclopenta[2,1-b;3,4- b0 ] dithiophene)-alt-4,7-(2,1,3-benzothiadiazole)] |
| PSS | Polystyrene sulfonate |
| PV | Photovoltaic |
| SWCNT | Single Walled Carbon Nanotube |
| TC | Transparent Conductor |
| TCO | Transparent Conducting Oxide |
| TGA | Thermal Gravimetric Analysis |
| THF | Tetrahydrofuran |
| UV | Ultraviolet |
| UV-Vis | Transmission Spectroscopy of light in the UV and Visible ranges |
| $V_{oc}$ | Open Circuit Voltage |
| ZnAc | Zinc Acetate (anhydrous) |
| $\eta$ | Power Conversion Efficiency |

# Chapter 1. Introduction to Organic Photovoltaics

## 1.1 Organic Photovoltaics Background

The field of Organic Photovoltaics, first introduced in the 1958 with a laminated magnesium pthalocyanine device [1], produced a 1% efficient device in 1986 [2], and has become a promising prospect for solar energy production ever since [3-6]. OPV devices are based on pi-conjugated organic semiconductors, a class of organic compounds which can conduct electrons on a backbone of alternating C-C and C=C bonds. Excited electrons delocalize across these bonds causing the molecule to behave like a semiconductor [7].

The two main categories of organic semiconductors are polymers and small molecules. Small molecules are monodisperse, and can be very crystalline, but can have poor carrier transport due to short conjugation lengths [8-15]. Small molecules can be thermally evaporated, or functionalized to be solvent processable. Polymers by comparison, are generally very large molecules that will be polycrystalline at best, and have a polydispersity that will introduce unknown parameters to the system. Polymers cannot be thermally evaporated due to their relatively large size, and are generally solution processed. The rest of this thesis will focus on polymeric OPV.

Although less efficient at converting sunlight into electrical energy, polymer based OPV has benefits that allow for lower cost manufacturing, and possibly lower cost per watt of power output compared to other technologies such as

single crystal silicon, amorphous silicon, cadmium telluride, or copper indium gallium selenide based PV [3, 16]. Many or all of the elements of the cell can be solution processed [17]. All of the layers can be made flexible to some extent, which greatly reduces transportation and installation costs. Flexible materials can be used in roll-to-roll processing, which has the capacity to cover large substrate areas in a single process step and reduce fabrication costs compared to other methods [3]. OPV devices can be made semitransparent [11, 18], which makes them available for building integrated PV applications in windows of buildings. They can also be made to perform very well in low light conditions, making them very attractive for indoor PV applications [19].

The main challenges faced by the OPV field are in their efficiency, their lifetime, and their materials costs. Although state of the art devices are currently 10% efficient [14, 20-22], some cost analysis models place the necessary efficiency for mainstream energy production at 15% to achieve $0.50 per watt{woodhouse}. Not all devices are air stable. Air stable OPV devices can be made, generally with inverted geometry (discussed later), but unencapsulated lifetimes under illumination are on the order of hundreds of hours [23]. The lifetime target for rooftop and utility PV is ~ 20 years (~100,000 hours). Encapsulation can increase lifetimes, but the field is still examining possibilities for flexible, impenetrable barriers [6, 24]. In addition to potential encapsulation, OPV devices all require a TC on at least one side of the device. TCs tend to be expensive, and can be chemically or mechanically fragile. The current standard TC is indium doped tin oxide. ITO works well in small area OPV applications, but

it is not abundant enough to be available for large scale energy production [3, 16]. It also needs to be heated to very high temperatures (~300 °C) in order to obtain the crystal structure necessary for good transport properties. These high temperatures are not compatible with flexible substrates. All of these challenges are being addressed by the OPV community, and a number of solutions is being studied for each [6, 25, 26].

### 1.2. Characterization of Photovoltaic Devices

The end goal of any photovoltaic device is to convert sunlight into useable energy. The figure of merit use is power conversion efficiency: the percentage of incident light energy that the cell is capable of converting into electrical energy. The tool for measuring power conversion efficiency for devices intended to be used outdoors is the solar simulator. A solar simulator consists of a lamp calibrated to resemble the solar spectrum at the surface of the earth. A varying electrical load is applied to the PV cell and current is measured. The area of the cell is considered and a current density is calculated. Current density vs. voltage curves that can quickly display the basic performance characteristics of the cell.

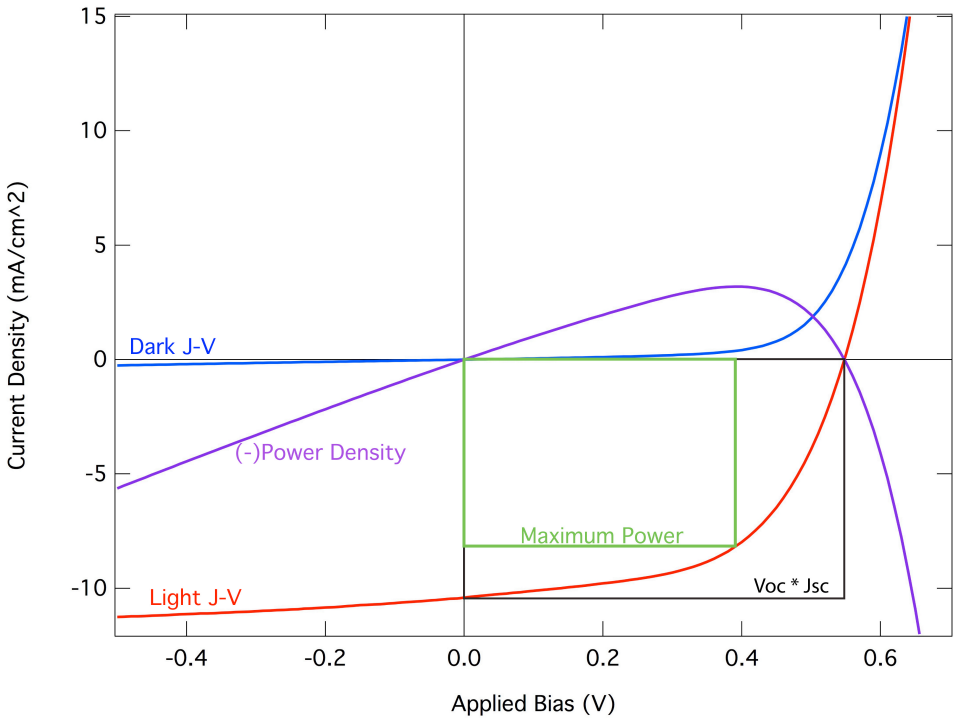


**Figure 1.2.1.** A typical *J-V* curve will include the current-voltage behavior of a device in the dark (blue) and under illumination (red). On this figure, the maximum power is found my maximizing the negative of the power density curve (purple), which is the product of the current and voltage at all points on the red curve. A negative sign is added to yield power produced. Maximum power is represented by the area of the green rectangle. Fill Factor is the area of the green rectangle divided by the area of the black rectangle.

In the dark the device behaves as a diode. Due to energy level alignment of the contacts with the respective HOMO and LUMO levels of the device, the contacts block charges from being injected into the device under reverse bias(see Fig. 1.3.3.1). There are no available states for charge injection in the reverse direction, so current under reverse bias is limited to leakage current with high series resistance. Under forward bias, after the turn on potential is reached, current flows with relatively low resistance. When the cell is illuminated, a current is produced in the reverse direction that can work against a certain forward bias until net current flows in the forward direction.

The following terms are defined under illumination: Open circuit voltage, measured in V or mV, is the bias potential where the forward (dark) and reverse (photoinduced) current are equal. As a result, it is the point where there is no net current. Graphically, $V_{oc}$ is the *x*-intercept of the graph. Short circuit current density, $J_{sc}$, measured in mA/cm$^2$, is the current that the device produces under no load. On the graph it is the *y*-intercept. Power, defined by the simple equation $P=IV$ can be calculated by multiplying the *x* and *y* axes, or finding the area under the curve at any point on the graph. Note that power will increase with active area with any system, so power per area is actually the key metric. Power is negative in quadrant IV, indicating that the cell is doing work (creating energy) when current is negative while voltage is positive. Fill factor is an ideality factor defined as the maximum power output density of the cell divided by the product of $V_{oc}$ and $J_{sc}$. Graphically, *FF* is the area of the rectange defined by the maximal power point and the axes divided by the area of the square defined by the two perpendicular bisectors of the axes at the intercepts of the light *J-V*. (See Fig. 1.2.1) One way to represent power is:

$$P_{\max} / Area = J_{\max} \bullet V_{\max} = J_{sc} \bullet V_{oc} \bullet FF \qquad \text{(Eq. 1.2.1.)}$$

Where $J_{max}$ and $V_{max}$ are the current density and voltage at the maximum power point, distinct from the $V_{oc}$ or $J_{sc}$. As a general indicator in linking measured quantities to physical properties, $V_{oc}$ is related to the energetics of the system and $J_{sc}$ is related to the charge collection and transport properties of the system. *FF* is a bit more convoluted, but it can be affected, among other things, by charge

recombination in the active layer or at the contacts, and series resistance within the device, or between the device and the measurement system. Power conversion efficiency ($\eta$) is the power output of the cell divided by the input. If solar irradiation is used, input power is the integral of the solar spectrum, which is ≈ 1000 W/m$^2$, or 100 mW/cm$^2$

$$\eta = P_{\max} / P_{in} \qquad \text{(Eq. 1.2.2.)}$$

$$P_{in} = \int_0^{\infty} F(\lambda) d\lambda \qquad \text{(Eq. 1.2.3.)}$$

Where $F(\lambda)$ is the energy per wavelength per area of the solar spectrum at the surface of the earth as determined by the AM1.5G spectrum.

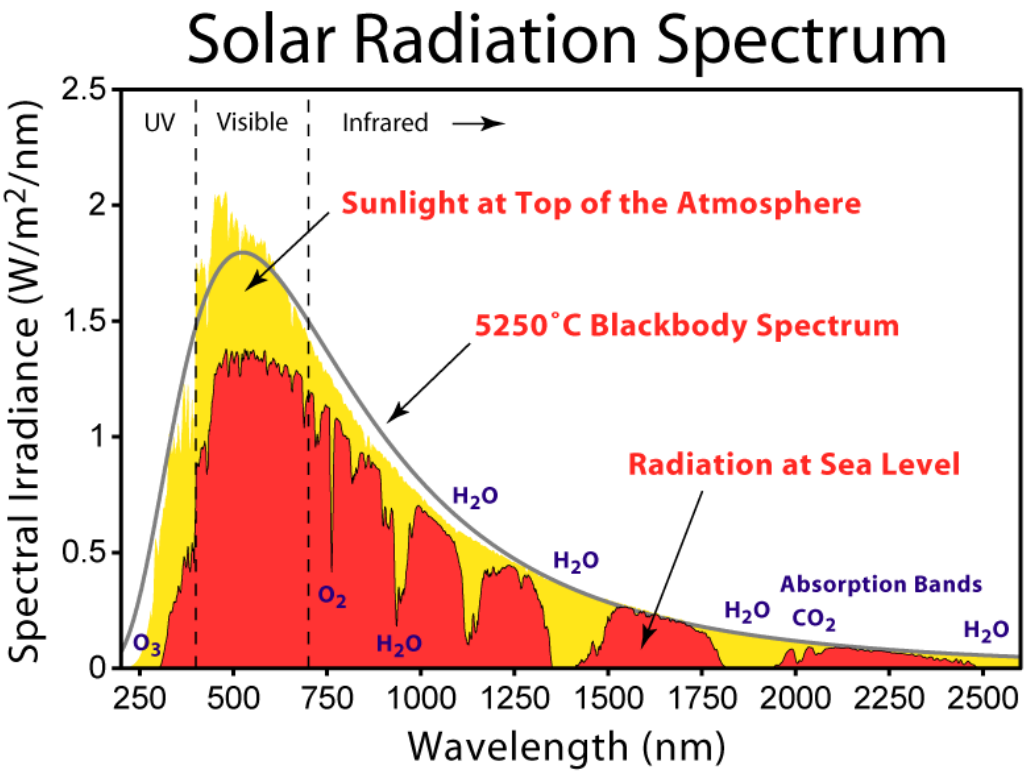


**Figure 1.2.2.** The solar spectrum at the surface of the earth compared to the upper atmosphere and the blackbody spectrum for the temperature of the sun [27].

## 1.3. Physics of Organic Photovoltaics

### 1.3.1. Excitonic Systems and Charge Generation

One of the primary functional differences between organic and inorganic PV is the presence of excitons and the need to dissociate them in OPV. Organic semiconductors have low dielectric constants ($\varepsilon_r \approx$ 3-4) [28, 29]. As a result, when a photon excites a charge from the highest occupied molecular orbital to the lowest unoccupied molecular orbital of an organic semiconductor, the electron and hole remain bound in an exciton because they are unable to overcome their fundamental electrostatic attraction to each other.

$$U = \frac{e^2}{4\pi\varepsilon_r\varepsilon_0 r}$$ Coulombic Attraction Potential (Eq. 1.3.1.1.)

Although qualitatively valid, the Coulomb potential cannot be used to calculate exciton binding energy. The electron and hole are attracted to each other very similarly to the proton and electron of a hydrogen atom, and are limited to discrete energy levels Energy levels of the exciton are given by a modified Rydberg equation.

$$E_n = \frac{-\mu e^4}{2\hbar^2\varepsilon_0^2\varepsilon_r^2 n^2}$$ Excitonic Energy Levels (Eq. 1.3.1.2.)

Where $\mu$ is the reduced mass of the electron and hole, using their effective masses, $\varepsilon_r$ is the dielectric constant of the semiconductor, and $n$ is the principal quantum number. The dissociation energy is the difference in energy from the ground state ($n = 1$) to a dissociated state analogous to ionozation ($E_\infty = 0$)

Due to the high dielectric constant of silicon ($\varepsilon_r \approx 12$) [30], excitons in silicon semiconductors are instantly separated into free charges by available thermal energy ($k_BT$). Photoinduced excitons in organic semiconductors have binding energies significantly greater than $k_BT$, on the order of 0.3-1 eV [29]. At room temperature, $k_BT$ is ~0.025 eV. In order to become separate and mobile charges, tightly bound Frenkel excitons must be dissociated into free electrons and holes. The most effective way to do this is to physically dissociate the electron and hole onto separate molecules. An exciton formed in a donor

molecule must diffuse to an interface between the donor and acceptor. At the interface, the electron jumps from the LUMO of the donor to the LUMO of the acceptor. The driving force for this separation is a decrease in energy between the LUMO of the donor molecule and that of the acceptor. The LUMO of the acceptor is farther from vacuum, making it energetically favorable for the exciton to dissociate and the electron to transfer to the acceptor. This is known as LUMO-LUMO band offset. As a result, the available energy of dissociated charges is lower than the electrical band gap of the donor, by at least the exciton dissociation energy.

Once the exciton has been dissociated into an electron on the acceptor's LUMO, and a hole on the donor HOMO, the charges are still not mobile. Because of poor screening, (again related to low $\varepsilon$) even once they are on different materials, the electron-hole pair still experiences Coulombic attraction (of the range 0.1-0.5 eV), resulting in the formation of Coulombically bound interfacial pairs [31]. These Coulombically bound electron-hole pair states are partially charge-separated states, where the hole is primarily localized on the donor HOMO orbital and the electron on the acceptor LUMO orbital but the Coulomb attraction remains greater than $k_BT$. Separated, but still Coulombically bound electron-hole pairs are known in literature variously as geminate pairs, bound polaron (or electron-hole or radical) pairs, charge-transfer excitons, exciplexes, and charge transfer (CT) states. The exact role of the CT state is not fully understood, and is still being investigated in the field [32-35]. One piece of evidence for its existence lies in the fact that it is possible to excite the CT state

directly. It is possible for an electron to be promoted directly across the effective gap of the donor-acceptor couple, in essence directly exciting the charge transfer state. Experiments [36] have shown that “pushing” the CT state with an infrared pulse increased the yield of free carrier generation.

Fullerenes are used almost exclusively as acceptor molecules in high efficiency OPV [3], but progress is being made with polymer acceptors as well [37, 38]. Non-fullerene acceptors in OPV devices have recently reached 5.2% PCE [39, 40]. Often functionalized for solubility and energy level changes [41], the most common acceptor fullerenes for OPV are C60 and C70 based PCBM. Also popular when paired with the most studied donor, P3HT, is a C60 fullerene with two indene groups added: ICBA. Due to the LUMO-LUMO offset of the P3HT:ICBA heterojunction, ICBA increases the voltage of a P3HT:ICBA heterojunction solar cell by about 250 meV over that of P3HT:PCBM [42].

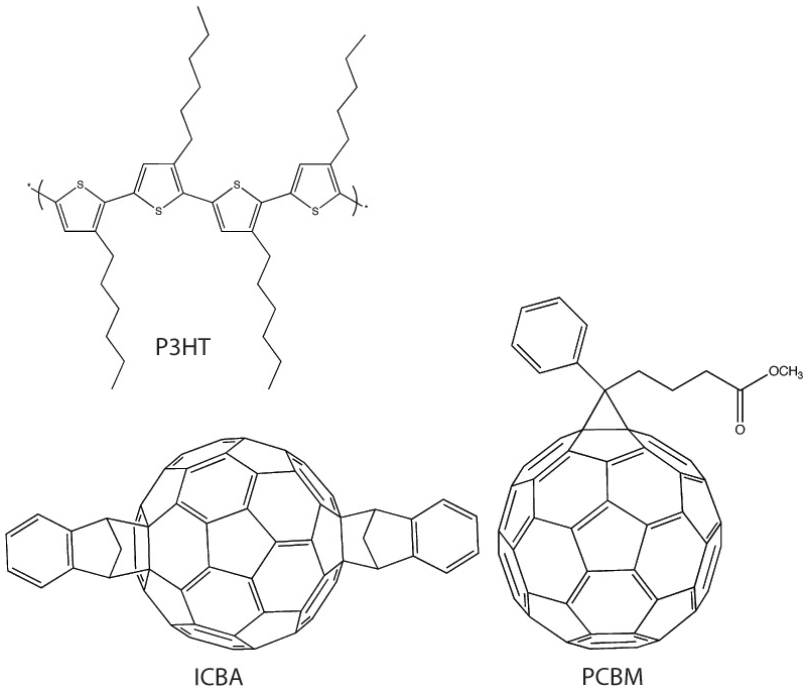


**Figure 1.3.1.1.** Chemical structures of a P3HT, a popular donor molecule, C60 ICBA and C60 PCBM, two popular fullerene acceptor molecules.

### 1.3.2. The Bulk Heterojunction

Organic absorbers have optical extinction coefficients α (~ $5 \times 10^4$ $cm^{-1}$) so that the characteristic absorption length 1/α ~100 nm [43].

$$I = I_0 e^{-\alpha t} \qquad \text{(Eq. 1.3.2.1.)}$$

In order to absorb a significant fraction of incident light, functional light absorbing (active) layers need to be on the order of 100 nm thick. In contrast, exciton diffusion lengths are on the order of 5 - 10 nm [44-47]. If an exciton is formed more than 10 nm away from an interface between the donor and acceptor, it will most likely recombine in the donor before it reaches the acceptor, and the absorbed energy will be lost to thermalization. Thus there are two competing

mechanisms: Optical absorption requires that the device have a thick ~100 nm absorbing layer, but exciton dissociation requires that the entire donor material be within ~10 nm of the acceptor. The bulk heterojunction [48] is one solution to this seeming paradox. To form a BHJ, the donor and acceptor molecule are mixed together in solution. Upon drying or annealing, the two chemicals partially or completely phase separate to form an interpenetrating network of donor and acceptor molecules.

Due to the very fine structure necessary for a functional heterojunction, techniques for analyzing the phase separation and microstructure of the 2 elements have only recently been introduced [49]. It was thought that ideally the structure would be interdigitated with features on order of the exciton diffusion length, but recent work has found the ideal picture to be less obvious combination of partially mixed amorphous phases, and crystalline ones [49, 50]. In this picture, charge transfer happens in intermixed phases, and free charges are energetically driven toward pure phases. The driving force for this is the reduced band gap in the crystalline vs. amorphous phase of each material. This band gap reduction is due to longer conjugation lengths in crystalline phases, and is readily observed in the absorption spectrum of crystalline vs. amorphous P3HT [51]. Bulk heterojunctions can also be formed by co-evaporating small molecules, and heating during deposition to promote phase separation [12], or even depositing a bilayer of the two phases from solution, then allowing them to mix upon heating [52].

### 1.3.3. Inverted vs. Traditional Geometry

Once free charges are created in the BHJ, they must still be transported through the BHJ to the contacts and collected in order to produce power. Since the BHJ is mostly isotropic, an asymmetry must be built into the system so that the charges have an energetically favorable direction to travel. The modification to this is that a thin P3HT rich skin layer forms on top if the film is dried in air [49]. Phase separation (if any) at the bottom of the film is dominated by the surface energy characteristics of the underlying substrate. The BHJ is sandwiched between two electrodes, at least one of which must be transparent. Most often, the other electrode will be metallic. Since light must enter through the transparent (most often ITO) contact, it earns the convention of being called the front of the device. To further complicate understanding, OPV fabrication typically starts with deposition onto the TC, so that side is often referred to as the bottom of the device, while the final metal deposition happens on top. Electrons can either travel toward the front ITO contact or the rear metal one, and vice versa for holes. If the front contact collects holes and the rear collects electrons, the device is said to have traditional geometry. If the front contact collects electrons and the rear collects holes, the device is inverted. (Fig. 1.3.3.1.)

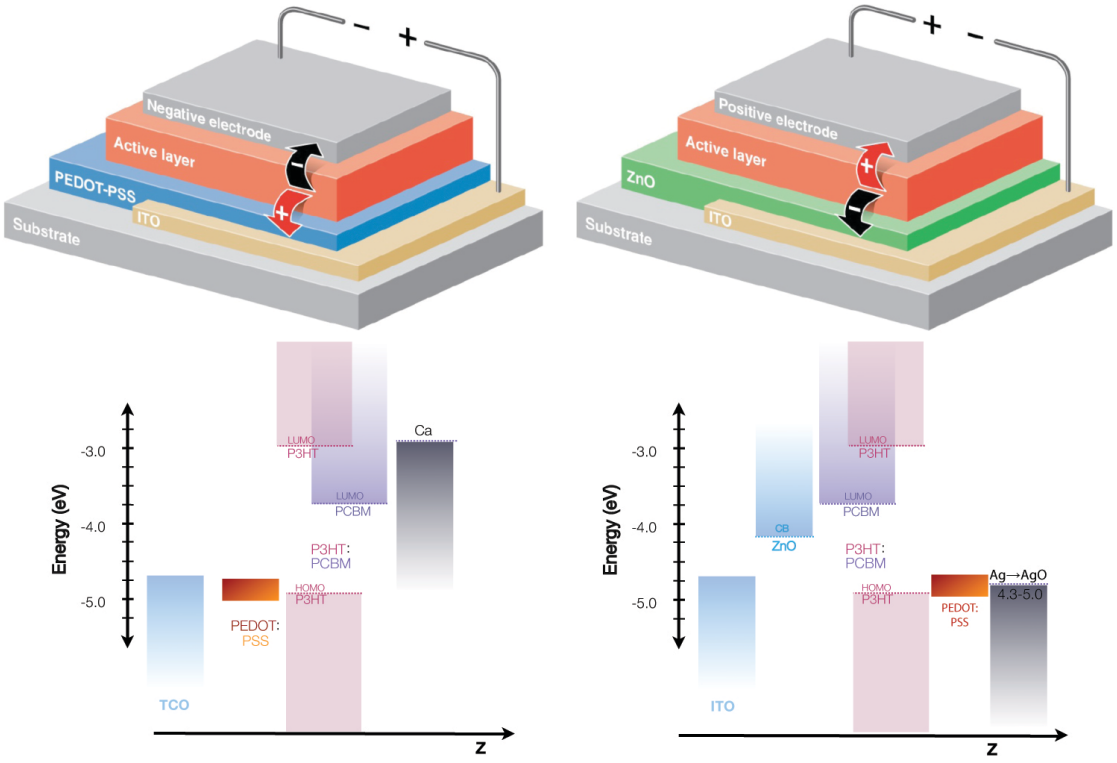


**Figure 1.3.3.1.** Graphics showing current flow and band structure of traditional (left) and inverted (right) geometry OPV cells.

Traditional geometry devices tend to have higher efficiency than inverted ones (Fig. 1.3.3.2). Due to the high energy level offset between the low work function electron collecting metal and the high work function hole collecting polymer layer (the details of which will be discussed in the next section), an electric field is induced in the active layer of the device, causing carriers to drift toward their intended contacts. Worth noting is that the active layer is a highly doped semiconductor with a relatively high carrier density [28], and a depletion width on the order of the thickness of the active layer film [53]. Thus the induced electric field is anisotropic within the layer. In either geometry, the open circuit voltage is dominated by the energy difference between the HOMO of the donor

and LUMO of the acceptor molecule, but is also affected to a lesser extent by the work functions of the charge transport layers and the contacts [54].

We hypothesize that electric field in an inverted device is much lower than one with traditional geometry. The contacts act as selective blocking layers so that each carrier has available states to enter at only one electrode. The electron contact does not have available states for holes, so it acts as an electron selective, or hole blocking layer, and vice versa for the hole contact. Current in inverted devices is driven largely by diffusion and the selective nature of the contacts that enforce chemical potential gradients for electrons and holes. This topic is under investigation by other group members.

The advantage of inverted devices is that the absence of a low work function metal allows them to be processed and measured in air. Due to their low work function top electrodes, traditional devices tend to degrade over a matter of days when exposed to ambient conditions. Inverted ones can be stored in air in the dark for months or more [55]. Unless otherwise stated, all devices discussed and fabricated in this work use inverted geometry and are measured in ambient air.

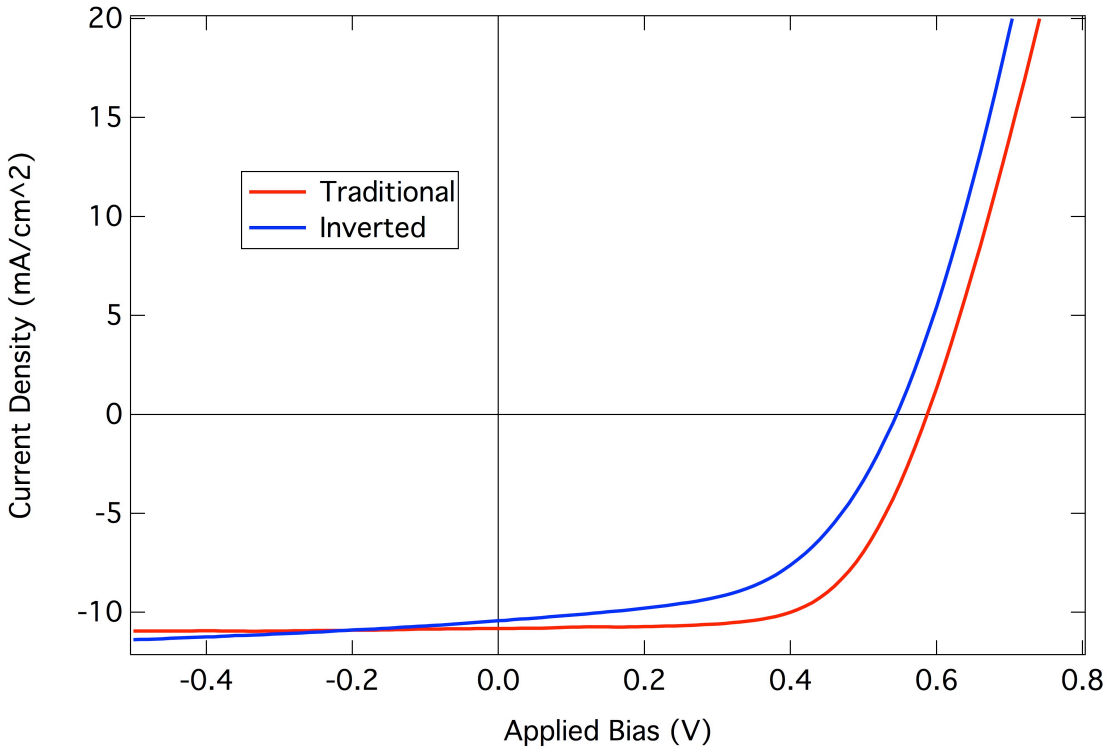


**Figure 1.3.3.2.** *J-V* curves of optimized traditional (red) and inverted (blue) geometry devices.

### 1.3.4. Contacts and Transport Layers

In OPV devices, the layers adjacent the active layer are responsible for determining the energetics of charge transport out of the device. Careful attention has been paid to the properties of the electrode materials in order to control these energetics [56-59]. One emerging trend is to use a semiconducting transport layer over the conductive contact [3, 60-68]. This transport layer can be optimized for device energetics, while the overlying contact simply becomes a way to shuttle current to an electrical connection.

The most popular hole contact to date for OPV is the semiconducting polymer PEDOT:PSS. PEDOT is a semiconducting polymer that is not soluble in water. PSS is added to soluablize the mixture and stabilize the doping of the

PEDOT. PSS dissociates to form sulfonic acid in water, and allows PEDOT:PSS to form an aqueous suspension that can be solution processed via spin coating or other solution deposition methods such as ultrasonic spray, or inkjet printing [69-73].

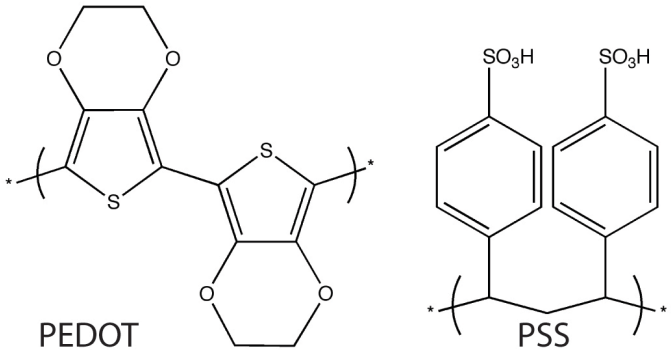


**Figure 1.3.4.1.** Chemical structures for PEDOT and PSS.

PEDOT:PSS makes a very good hole contact for P3HT devices because PEDOT's work function of ≈ 5.0 aligns very well with the HOMO energy of P3HT. It also acts as an electron blocker, providing a diffusion gradient for hole transport. For donors with higher HOMO levels (further from vacuum), transport layers with higher work functions have been shown to increase device voltage and efficiency [74]. In addition to suffering from intrinsic degradation in air, the hygroscopic and acidic nature of PEDOT:PSS also cause it to contribute significantly to device degradation by damaging other layers in the cell [75-78]. Another issue with PEDOT:PSS is its aqueous nature. Many active layers, including P3HT one, are hydrophobic. In order to effectively spin coat PEDOT:PSS onto a hydrophobic active layer, the active layer must be treated

with an oxygen plasma, or additives [71, 79] must be used in the PEDOT:PSS to promote wetting. Because it is a nanoparticle suspension and not a true solution, PEDOT:PSS even wets itself relatively poorly compared to plasma treated ITO, clean glass, or other hydrophilic materials. Recently, a variety metal oxides have been shown to work well as hole contacts [80]. These do not have the hydroscopic or acidic properties of PEDOT:PSS, but few are solution processable [81-83], and none yet have the processing versatility of PEDOT:PSS, which can be deposited onto almost any surface without heating above 100 °C, conversion, or organic solvents.

Traditional geometry devices often use a low work function metal as the top contact with no transport layer [56]. Due to the high work function of ITO, inverted devices must have an electron selective contact modifier over the ITO electrode, and a high work function (often metallic) back contact. Bare metal can be used as the hole collecting contact, albeit less efficiently than with a hole transport layer [84]. The most frequently used electron transport modifiers are ZnO [84], and TiOx [18], although new alternatives look very attractive [60]. In this dissertation, ZnO is used exclusively as an electron collection layer. Until Chapter 6 explores different methods, ZnO is grown from a Zinc Acetate precursor. It is highly n-doped, and acts as an electron selective contact because of it's good energy level alignment with electrons in the device, and unavailable states for hole transport. See Fig.5.3.2. for a band diagram of ZnO.

## 1.4. Motivation for Lamination

The main work of this thesis will focus on lamination. In this context, lamination means that part of the device is deposited onto one substrate, and the rest is deposited onto another. The two substrates are then laminated together to complete the device (Figure 1.4.1). As we will show, lamination enables the in-air fabrication of devices with power conversion efficiencies equivalent to evaporated contact devices fabricated in parallel.

Lamination as a method to fabricate OPV has several potential advantages over conventional bottom-up fabrication. First, the processing step of thermal evaporation of a metal onto a polymer layer is eliminated, as the metal electrode is now deposited onto a bare substrate. Thermal damage of the active layer has been proposed to occur during conventional metal evaporation, and high parasitic resistances have been measured in evaporated metal-organic interfaces, compared to laminated ones [85]. It has been shown that the rate of metal evaporation onto a polymer:fullerene active layer is an important determining factor for the efficiency of the device [84]. Therefore, unless one has access to a high quality (and potentially expensive) thermal evaporation system that allows precise control of the evaporation rate, the fabrication of consistently performing inverted OPV devices may be problematic. A lamination press is an order of magnitude cheaper than a vacuum based thermal evaporation system and will reduce capital investment costs, enabling research in small institutes that want to explore the field. Second, lamination produces a self-encapsulated device that is mechanically protected on two sides. Utilization of flexible

substrates with good oxygen and moisture barrier properties should also result in enhanced lifetimes of laminated devices. Lamination is a versatile tool compatible with many different materials, processes, and fabrication techniques. Chapter 3 will show the technique's applicability to electrodes that are incompatible with standard fabrication procedures. Chapter 4 will use the technique to explore the physics of device performance evolution, and Chapter 5 will use it to laminate one entire device to another to create a tandem structure. In addition to its scientific benefits, lamination is compatible with roll-to-roll processing on flexible substrates and with solution-processed metal electrodes [86].

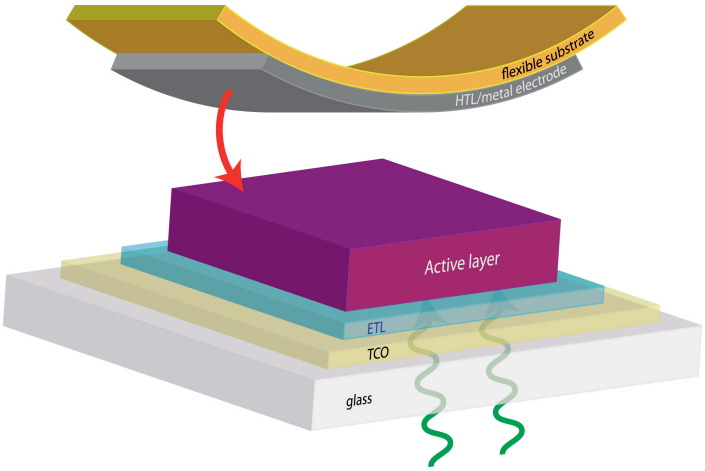


**Figure 1.4.1.** Basic structure of the lamination process

### 1.5. Tandem OPV

In a single junction cell, there will be a tradeoff between voltage and current which is dictated by the band gap of the absorber. A higher band gap allows for a higher voltage, but only high energy photons will get absorbed. Lower band gap materials absorb a larger portion of the spectrum, but electrons from high energy photons are thermalized to the band edge, with any extra energy mostly dissipated as heat. This, as well as a thermodynamic detailed balance of absorbed and radiated photons, presents an efficiency limit (known as the Shockley-Queisser limit) of 32% for a single junction solar cell [87]. The goal of multijunction PV is to use complimentary absorbers to absorb more of the solar spectrum while maximizing the energy collected from each photon. Although OPV is far from the 32% single junction limit, it can still benefit from a multijunction structure to reduce the overall cost per watt of the technology.

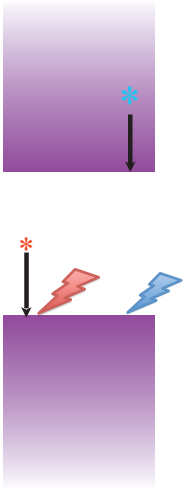

**Figure 1.5.1.** Energy Level Diagram depicting the motivation for tandem OPV. In a single junction cell, low energy photons do not get absorbed, and high energy photons lose any surplus above the band gap to thermalization. The black arrows represent energy from each photon that is unharnessed by the cell.

One solution to this problem is to construct tandem cells [88]. In tandem PV, two (or more) different absorbers are used. They are generally stacked in series, with light unabsorbed by the first layer passing through to the second layer. In order to connect the two series subcells, an interconnect layer (also referred to as a recombination layer) must be inserted between them. In an inverted geometry the ICL must act as an HTL for the front cell and an ETL for the back cell. The charges recombine within the layer and balance the current of the tandem. This layer must be as transparent as possible, since light must still be transmitted to the back cell of the device.

In a multijunction device the most common method to connect the subcells is in series. In a series circuit the voltage is the sum of the two subcells' voltages, but due to conservation of charge, both must have the same current.

$$J_{series} = J_1 = J_2$$
$$V_{series} = V_1 + V_2 \qquad \text{(Eq 1.5.1.)}$$

As a result, to first order, the current of the tandem is limited by the lower of the two subcells [88]. If the subcells have different fill factors, it is slightly advantageous for maximum PCE to have the subcell with the higher *FF* operate with a slightly higher current at $J_{sc}$ than the one with lower *FF* [89, 90]. Careful work must be done with layer thicknesses to match the current of the two subcells, thus maximizing the current of the device. Since the thickness of the active layers is on the same order of magnitude as the wavelengths of light,

optical effects can be a significant factor. Optical spacers have been proven effective in models and in functional tandem devices [91]. Computational modeling plays an important role in determining optimal layer thicknesses [88, 92, 93].

One challenge to tandem OPV fabrication is that of orthogonal solvents. Since organic active layers are often soluble in the same solvents, care must be taken to ensure that the solution coating of one layer does not dissolve any of the layers beneath it. One fix is to evaporate metal or metal oxide buffer layers to protect underlying organics [94-96]. Another option is to alter one or more of the organic layers to be more chemically robust[97]. The option explored in Chapter 6 is to deposit the active layer of each subcell onto different substrates, which are then laminated together.

### 1.5.1. Optical Modeling

When light hits an interface between two media, a portion is reflected, and a portion is transmitted through the interface. This fraction of reflected light is generally given by the Fresnel equations. Although complicated by polarization, angle of incidence, and magnetic permeability, for normal incidence and dielectric materials ($\mu = \mu_0$), the Fresnel equations reduce to:

$$\frac{E_{trans}}{E_0} = \frac{2n}{n'+n}$$

$$\frac{E_{refl}}{E_0} = \frac{n'-n}{n'+n}$$ (Eq.

1.5.1.1.)For the reflected wave, the sign convention is that for polarization parallel to the plane of incidence. This means that if n' > n there is a phase reversal for the reflected wave.

Due to the relatively thin layers in an OPV device, optical interference must be considered. Reflected light can interfere with transmitted light, changing the overall reflection, and transmission at each interface, and the and intensity at various points within the stack. The overall reflection of a layer structure is the sum of an infinite number of reflections, which is cumbersome to calculate. One way to calculate the optical field at various parts of the stack is to use the transfer matrix method[93, 98-100]. In this method, the field in each layer can be found by representing the layers by matrices of their admittances (related to indices of refraction), and phases. This allows one to know the field at any point in a multilayered stack, in order to maximize that field in the position occupied by the active layer of the cell.

## 1.6. Dissertation Outline

This dissertation will focus on the physics and device properties of OPV devices made with lamination.

Chapter 2 will introduce the lamination procedure. Materials and techniques will be discussed, analyzed and optimized for the P3HT:PCBM system.

Chapter 3 will use the previously established technique to create devices from previously difficult or impossible to integrate electrode materials. The lamination technique will first be modified to work without the hole selective PEDOT:PSS, and will then be applied to three different semitransparent contacts: PEDOT:PSS, single walled carbon nanotubes, and silver nanowires. Due to the nature of these contacts, lamination is the best, if not the only way to make inverted devices using them as the back electrode.

Chapter 4 will explore the contact evolution of inverted devices. When silver is evaporated onto an inverted OPV without a hole transport layer, it needs to age a few days before the device performs optimally. We hypothesize that this may be due to either silver oxide or silver sulfide forming at the silver/BHJ interface. Bare contacts made from silver oxide and silver sulfide are laminated to OPV devices to infer which compound is formed when pure silver is evaporated and allowed to age on its own.

In chapter 5, tandem devices are laminated together. One active layer is deposited onto each substrate, and they are laminated together to make the tandem. Although the method works well, we learn that the ZnO is to blame for

non-optimal device performance. There is also some work of optical interference modeling and data fitting regarding matching currents in the two subcells of the tandem.

Chapter 6 explores the physics behind the basis of lamination: adhesion. Different mechanisms of adhesion are proposed and calculated based on known materials properties. Calculations are quite broad, but within the range of measured values for adhesion force. A general picture of the physics involved with lamination and adhesion emerges.

Appendix A is a list of supplemental figures and unfinished experiments that the author thought important to record and share, but was unable to finish completed studies on.

## Chapter 2. Hot Press Lamination

### 2.1. Introduction

Recent progress on materials optimization for organic photovoltaics (OPV) has resulted in efficiencies exceeding 10% [20]. While these advances in efficiency bring the technology closer to commercialization, there is also strong motivation to improve the processing techniques for the fabrication of these devices. Of particular concern is compatibility with large-area manufacturing on flexible substrates and encapsulation for mechanical robustness and stability against degradation [101]. Due to the nature of the polymeric materials involved in OPV, unconventional methods of fabrication that encompass these traits become possible. One of these methods is the simple lamination ("gluing") of two parts of the device to finish the final OPV structure, as was shown over a decade ago for polymer-polymer bilayers [102] and has recently been demonstrated for polymer-fullerene bulk heterojunctions [103, 104]. In contrast to lamination of inorganic PV that is performed to encapsulate a finished device, the OPV lamination process brings two active elements of the device into contact with the goal of forming a functioning charge-collecting interface. Device structure is shown in Figure 2.3.1. The laminated OPV devices reach 3.19% power conversion efficiency at 1 sun. The superior efficiencies high fill factors (typically over 0.55) of laminated devices relative to evaporated devices indicate good electronic contact between the laminated layers. We present studies of the

effect of various parameters of the lamination on device performance as well as demonstrate the processing steps that are important and must be carefully controlled in order to obtain efficient devices.

## 2.2. Background & Motivation

In this paper we report on OPV devices fabricated in air with a hot press lamination process. Lamination as a method to fabricate OPV has several potential advantages over conventional bottom-up fabrication. First, the processing step of thermal evaporation of a metal onto a polymer layer is eliminated, as the metal electrode is now deposited onto a bare substrate. Thermal damage of the active layer has been proposed to occur during conventional metal evaporation, and high parasitic resistances have been measured in evaporated metal-organic interfaces, compared to laminated ones [85]. It has been shown that the rate of metal evaporation onto a polymer:fullerene active layer is an important determining factor for the efficiency of the device [84]. Therefore, unless one has access to a high quality (and potentially expensive) thermal evaporation system that allows precise control of the evaporation rate, the fabrication of consistently performing inverted OPV devices may be problematic. As we will show, lamination enables the in-air fabrication of devices with power conversion efficiencies equivalent to evaporated contact devices fabricated in parallel. Second, lamination produces a self-encapsulated device that is mechanically protected on two sides. Utilization of flexible substrates with good oxygen and moisture barrier properties should

also result in enhanced lifetimes of laminated devices. Finally, lamination is compatible with roll-to-roll processing on flexible substrates and with solution-processed metal electrodes [86]. To demonstrate hot press lamination we use the prototypical P3HT:PCBM bulk heterojunction in an inverted geometry, [64, 83, 84, 105] using a solution-cast ZnO underlayer as the electron collecting contact and a laminated PEDOT:PSS / Ag layer as the hole collecting top electrode.

## 2.3. Experimental

The two parts of the device, one on glass and the second on a flexible plastic PET substrate, are fabricated in air as follows. A glass slide with patterned ITO is sonicated in acetone and isopropyl alcohol, then treated with an oxygen plasma for 5 minutes. Zinc oxide is deposited from zinc acetate solution followed by thermal conversion at 300 ºC in air [84]. An active layer of 320 nm is spun from a 1:1 weight ratio of P3HT:PCBM dissolved in chlorobenzene with 2% dibromooctane added to promote phase separation without the need for solvent or thermal annealing [106, 107]. On the PET film, 100 nm of silver is thermally deposited, followed by a 40 nm spin-coated film of PEDOT:PSS. For the best devices the PEDOT:PSS was doped with 10% by weight d-sorbitol [108], unless otherwise stated. The PET substrate is then annealed at 115 ºC for varying annealing times as discussed below. The two parts of the device are then placed in contact as shown in the figure 2.3.1, and placed in a hydraulic hot press for lamination . Both top and bottom plates of the press are preheated to 130 ºC (verified within 2%) and the sample is pressed with 1.9 MPa (275 psi) of pressure

for 5 minutes. Control devices were fabricated in parallel with evaporated top Ag contacts by spin coating PEDOT:PSS on top of the P3HT:PCBM active layer and annealing at 130 ºC, followed by thermal evaporation of 100 nm Ag. To facilitate adhesion of the PEDOT:PSS layer, the active layer was exposed to a light oxygen plasma.

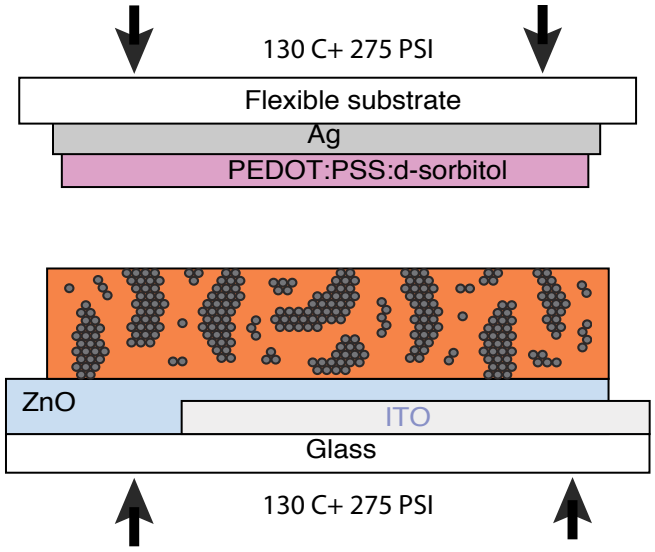


**Figure 2.3.1.** Laminated device structure.

Current-voltage (*J-V*) curves are measured on an AM 1.5G solar simulator with a Xenon lamp calibrated to one sun intensity. The device area of 0.11 $cm^2$ defined by the electrode geometry is inaccurate because of the high conductivity of the doped PEDOT:PSS layer, so an aperture was used to define a device area of 0.0514 $cm^2$ [109, 110]. It was verified that the EQE of devices integrated with the AM1.5G spectrum reproduces the short circuit current density with a 10% accuracy (Figure 2.4.2). Although an aperture is unnecessary for evaporated

contact devices, the evaporated contact control devices were apertured to .0401 $cm^2$ for a more accurate comparison to the laminated contact devices. Aperturing evaporated contact devices to 0.0401 $cm^2$ from 0.11 $cm^2$ decreases their open circuit voltages and increases fill factors while keeping the short circuit current constant. The efficiency is consistent within error of the measurements.

## 2.4. Results and Discussion

Typical *J-V* curves of laminated devices and comparison to devices with a thermally evaporated top contact with a PEDOT:PSS hole transport layer are shown in Fig. 2.4.1. The device performance parameters are summarized in Table 2.4.1, where the average and standard deviation of performance parameters taken from six laminated devices is also shown. As we will discuss below, optimizing the annealing step of the PEDOT:PSS layer impacts both the efficiency and the reproducibility of the devices. The best laminated device has an efficiency of 3.19% and was achieved when the zinc acetate precursor solution was prepared fresh, stirred overnight at room temperature, then spun just before device fabrication. As documented in previous work, inverted devices benefit from aging in air, with efficiencies gradually improving due to change on the work function of the top Ag electrode [55]. This phenomenon is also observed in the laminated inverted devices presented here, but to a lesser extent. The best efficiencies are reached 5-7 days after the fabrication of the device, but the overall improvement is around 20% over the day zero

performance. During that period the devices were stored in the dark in ambient conditions.

Compared to the best inverted device presented by White et al [84], laminated devices have good $V_{oc}$ of 549 mV and much higher FF of 56%. The $J_{sc}$ of the laminated device is lower at 10.3 mA/cm$^2$, but efficiency is still improved compared to evaporated contact devices (table 2.4.1). The higher *FF* of the laminated devices may be related to the presence of PEDOT:PSS without a potentially damaging oxygen plasma treatment of the active layer to improve wetting on the active layer. The device results obtained by White et al. did not use PEDOT:PSS/Ag top contact.

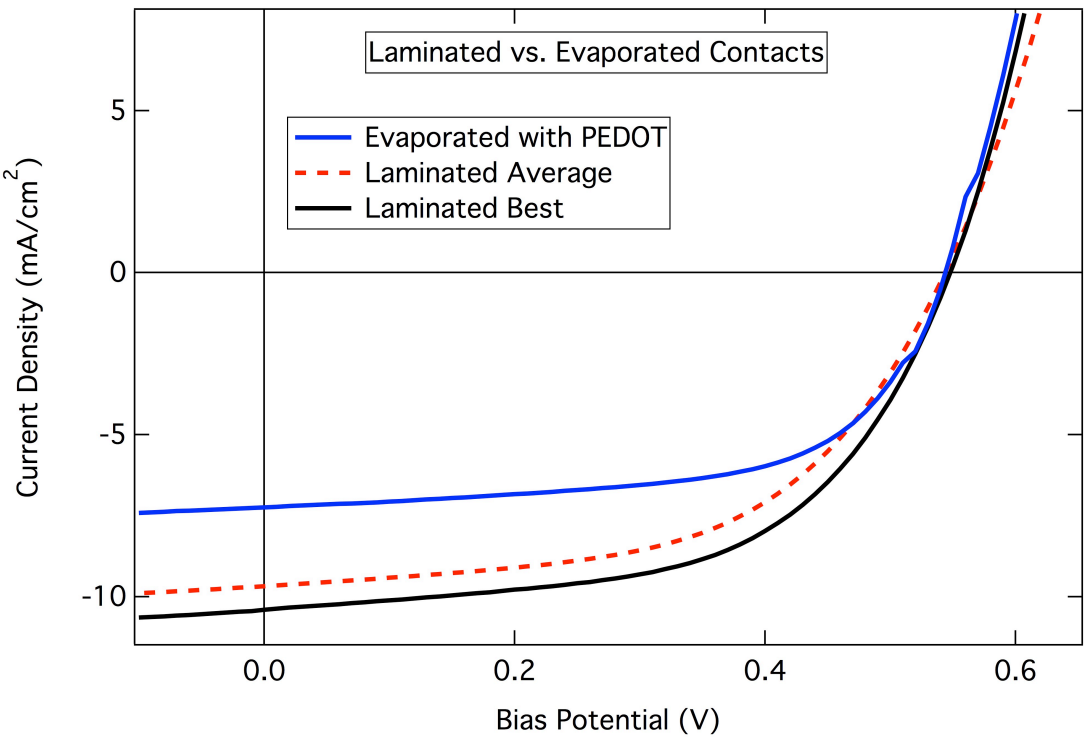


**Figure 2.4.1.** Typical *J-V* curves of inverted OPV devices made by hot press lamination (dotted red) compared to ones with thermally evaporated top contact (solid blue). The best performing laminated device is also shown (solid black).

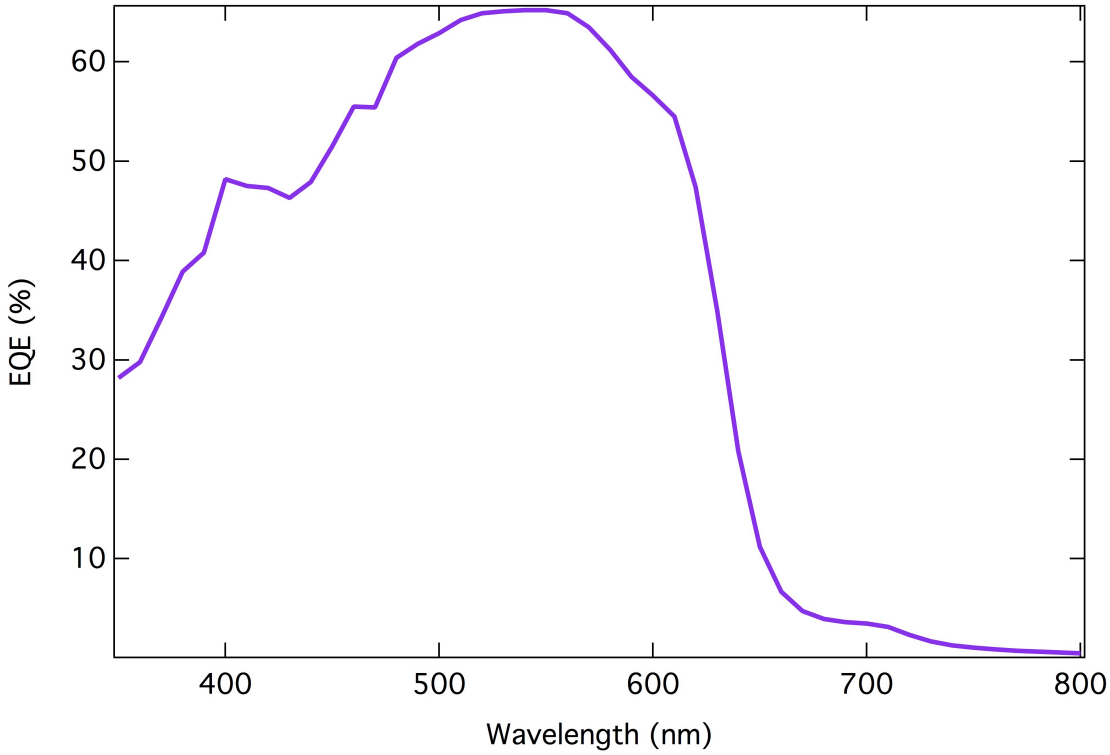


**Figure 2.4.2.** External Quantum Efficiency of laminated OPV, verifying short circuit current.

| Top Contact | $V_{oc}$ (mV) | $J_{sc}$ (mA/cm$^2$) | $FF$ (%) | $R_s$ (Ω) | $\eta$ (%) |
|---|---|---|---|---|---|
| Avg Evap control w/ PEDOT | 545±2.5 | 7.23±.47 | 60.8±.23 | 41±1.5 | 2.40 |
| Avg Laminated | 545±4.8 | 9.78±.73 | 54.5±1.8 | 77±20 | 2.92±.27 |
| Best Evap {White, 2006 #3} | 556 | 11.22 | 47.5 | | 2.97 |
| Best Laminated | 549 | 10.39 | 56 | 37 | 3.19 |

**Table 2.4.1.** Performance characteristics of laminated contact devices compared to evaporated contact ones. The control and laminated devices were made during this study, while the best evaporated device data was taken from previous work [84].

The performance of OPV devices fabricated with hot press lamination is critically affected by the composition and thermal treatment of the PEDOT:PSS layer. Figure 2.4.3. demonstrates the significance of the PEDOT:PSS layer and the d-sorbitol additive on the performance of laminated devices. These samples were fabricated at the same time under conditions that allowed us to compare different compositions of the laminated contact. The best laminated device of the series contained d-sorbitol additive (10% by liquid weight) and had an efficiency of 2.67%. This differs from the 3.19% laminated device since the other parameters mentioned in the study had not yet been optimized.

With no PEDOT:PSS interlayer, the devices have poor efficiency with very low $V_{oc}$ of 173 mV, and $J_{sc}$ of 3.9 mA/cm$^2$. This indicates the presence of a barrier for charge collection at the laminated (hole collecting) side of the device in the absence of PEDOT:PSS. The low *FF* of 29%, and high series resistance, measured from the inverse slope of the curve at + 1 V, of ca. 200 Ω, indeed suggests poor electrical contact at the laminated interface. The presence of a PEDOT:PSS interlayer drastically improves the device performance: $V_{oc}$ is 506 mV, $J_{sc}$ is 8.1 mA/cm$^2$, series resistance drops to 50 Ω, and *FF* increases to 52%. These observations verify that the PEDOT:PSS is providing an ohmic contact for hole extraction[104, 108]. The addition of d-sorbitol to the PEDOT:PSS interlayer further increases the $J_{sc}$ to 8.7 mA/cm$^2$ and the *FF* to 58%. In some cells, the fill factor is over 60%, and the series resistance is reduced to 35 Ω. The decreased series resistance and increased *FF* are consistent with increased conductivity of the PEDOT:PSS:d-sorbitol. The d-

sorbitol doped films exhibit much enhanced adhesion, and devices from these films are made more physically robust during the lamination process. About 25% of the undoped PEDOT:PSS devices delaminated when the plates of the press were pulled apart, while none of the doped PEDOT:PSS devices failed in this manner. Further work on adhesion will be discussed in Chapter 6.

Sublimation of d-sorbitol occurs at 120 ºC at atmospheric pressure and is responsible for the increase in the conductivity of the film[111]. The d-sorbitol treatment also alters the work function from 5.1 to 4.8 eV in films deposited on glass[111]. However, in the devices shown in this work, the $V_{oc}$ is relatively unchanged between PEDOT:PSS with and without d-sorbitol. This is in contrast to what is seen in non-inverted devices, in which formulating the PEDOT:PSS with sorbitol results in a decrease in $V_{oc}$ [68]. We also note that the $V_{oc}$ of inverted devices using a thermally evaporated Ag top contact has been seen to correlate with the work function of the Ag [55]. That the behavior of this laminated electrode is different suggests that either the chemical potential at the laminated interface is decoupled from the work-function of the electrode, presumably due to a lack of Fermi level pinning, or that it is the Ag in the PEDOT:PSS:d-sorbitol/Ag that is dominating the chemical potential.

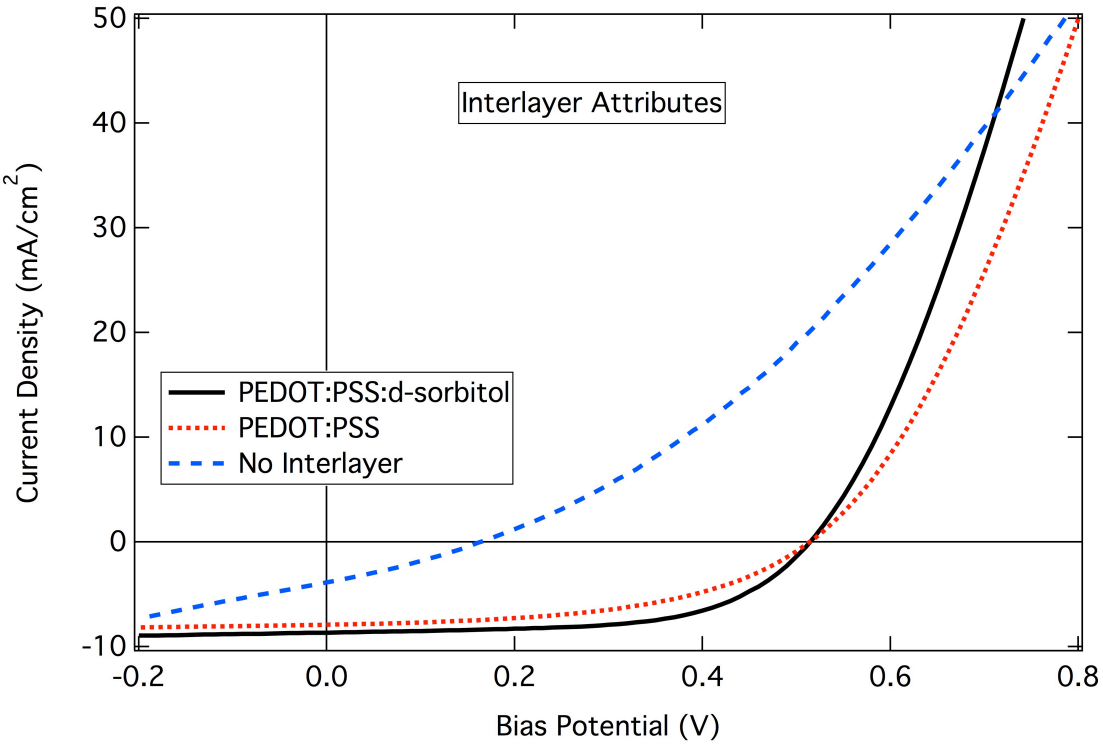


**Figure 2.4.3.** *J-V* curves of devices with various layers at the lamination interface. The blue dashed line shows performance from a device laminated without an interlayer between the bulk heterojunction and the Ag on PET. The red dashed line has a PEDOT:PSS interlayer, and the solid black line has a PEDOT:PSS:d-sorbitol interlayer.

During annealing of the PEDOT:PSS:d-sorbitol layer a balance needs to be achieved between removing water from the film, while maintaining levels of d-sorbitol at the lamination interface until an electrical connection is made. Careful control of the annealing conditions of the PEDOT:PSS:d-sorbitol layer is one of the most important parameters for efficient and reproducible laminated devices. Figure 2.4.4. shows the effect of different pre-lamination treatments of the PEDOT:PSS:d-sorbitol interlayer on device performance. The error bars correspond to the standard deviation between six devices on the same substrate. The following types of treatment were used: i) drying in ambient conditions, ii) a

10 minute vacuum step without heat and iii) an annealing step on a hot plate in air set to 115 ºC. In treatment iii) the time on the hot plate was varied between 2 and 10 minutes. Annealing above 115 ºC leads to delamination during fabrication and poor reproducibility. Figure 2.4.3 shows that both the $J_{sc}$ and the *FF* of devices increase and become more consistent when the samples are heated, while the $V_{oc}$ is relatively unchanged. We conclude that annealing the PEDOT:PSS:d-sorbitol layer at 115 ºC for 10 minutes increases both the performance and reproducibility of laminated devices. Note that the efficiency of the optimized devices in Figure 2.4.4. is ca. 2.4%, lower than the 3+ % reported above. The results shown in Figure 2.4.4. are taken from devices measured shortly after the lamination process without allowing them to age, which improves their efficiency.

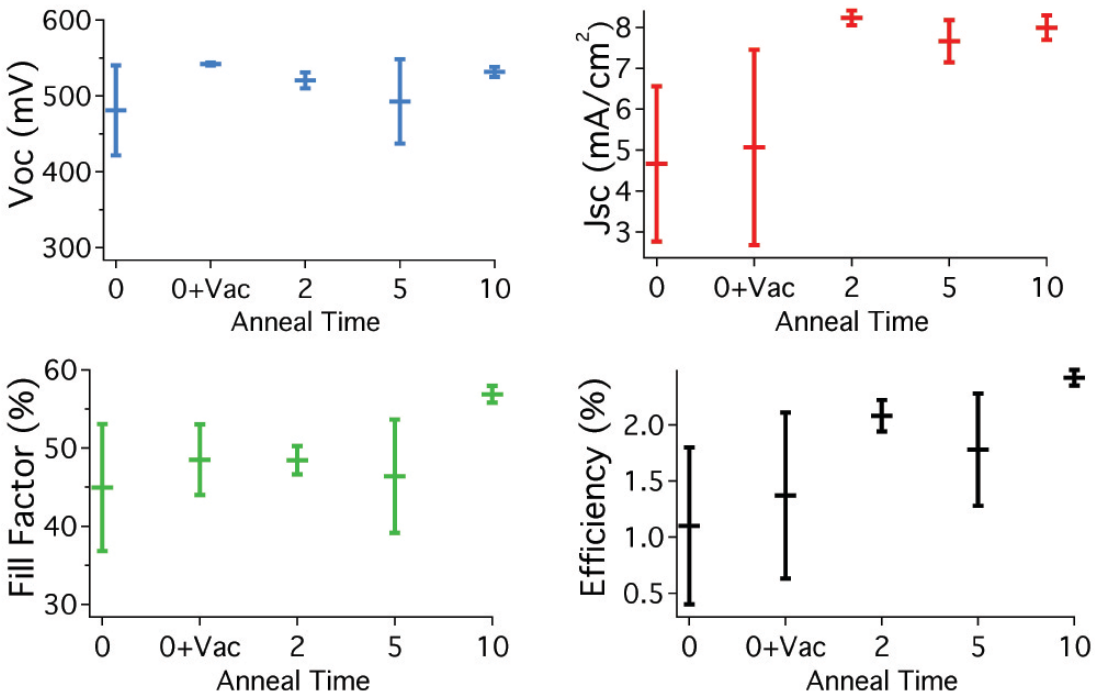


**Figure 2.4.4.** Device performance parameters for different pre-lamination treatments of the PEDOT:PSS:d-sorbitol interlayer. "0" represents drying the layer in ambient conditions, and "0+Vac" represents drying the layer in vacuum of $10^{-1}$ torr at room temperature for 10 minutes. The other points correspond to annealing the layer at 115 ºC in air for 2, 5 and 10 minutes.

Additional parameters were explored and were found to have less effect on device performance. Lamination pressure was varied from 0.7 to 2.4 MPa (100 to 350 psi) with a broad performance peak between 1.31 and 2.07 MPa but with small variations outside that range. Lamination time was varied from 0.5 to 30 minutes with devices laminated 2 minutes or less showing poor reproducibility, and devices annealed longer than 5 minutes showing no significant improvement. Thickness of the active layer was varied from 230 to 560 nm, with thicker layers showing higher $J_{sc}$ and lower *FF* values. The optimum thickness was near 320 nm, the same as reported for evaporated contact devices [84].

## 2.5. Conclusions

In summary, we demonstrate that lamination of the Ag contact can produce inverted OPV devices with efficiencies higher than devices made in parallel with thermal evaporation of the top contact. The processing parameters that are important in the fabrication process are the presence of a PEDOT:PSS:d-sorbitol interlayer at the lamination interface, the pre-lamination treatment of that layer. If these parameters are adequately controlled, devices with efficiencies over 3% are routinely achieved. As will be shown in future chapters, lamination is generally applicable to a wide range of contacts and active layers. In addition to the electrodes shown in chapter 3, we were able to change the P3HT:PCBM active layer to P3HT:ICBA (shown in chapter 5), and to PCDTBT:PC70BM (shown in appendix A). The flexibility of the technique will allow research groups to investigate other OPV materials without some of the limitations of sequential deposition.

In addition to the scientific benefits of the technique, lamination provides a way to produce efficient OPV devices with reduced capital investment costs. A lamination press is an order of magnitude less expensive than an evaporation chamber. Electrodes can be purchased from an offsite evaporator, or metal foils can be used. Lamination also opens pathways for low cost deposition of electrode materials, such as solution cast electrodes.

## Chapter 3. Transparent Back Electrodes and Alternative Adhesives

### 3.1 Introduction

While PCE advances are led by the development of new active layer materials, an aspect of OPV that is increasingly attracting attention is the electrical contacts. From the device physics standpoint, new active layer materials with tunable energetics require tunability in the contact work functions for efficient charge extraction [59, 112]. For the transparent conducting side of the device, limited worldwide indium supplies make ITO a controversial choice for the transparent contact in large scale PV applications [113]. Flexible ITO on plastic is inherently lower quality in its optical transmission and sheet resistance than rigid ITO on glass, due to constraints of substrate temperature, limiting its electrical properties when used in large scale roll to roll applications. On the potentially opaque side of the device, evaporating metal directly onto a solution processed active layer is not easily scalable to large area production, and it requires an on-site vacuum deposition chamber, which can be costly. Evaporating metals quickly onto organics involves a fair amount of heat transfer, which can potentially damage the organic layer.

One of the most disruptive developments regarding contacts in OPV has been the adoption of the so-called inverted device geometry [18, 22, 84, 105, 114, 115]. Its main advantage is that it does not require a low work function contact for electron collection resulting in increased shelf life and functional

lifetime of the OPV device [23, 55]. The bottom contact is modified with ZnO, and the top contact is Ag, either bare or modified with PEDOT:PSS. All fabrication steps except for metal evaporations can be performed in ambient air.

This work demonstrates a versatile toolbox of methods for scalable fabrication of laminated OPV devices. D-sorbitol alone is first explored as an adhesive for the silver back contact in inverted OPV devices, as opposed to the previously used PEDOT:PSS:d-sorbitol adhesive. This allows for the lamination of a metal electrode without an interlayer, which will later facilitate lamination from either the electron or hole side contact. Next, alternative back electrode materials are studied using the lamination procedure. PEDOT:PSS films, single walled carbon nanotubes, and silver nanowires are studied in OPV devices and compared to solid silver films. PEDOT:PSS is a widely used conductive polymer with many applications. We use it here as an electrode without the problems of wetting when spin-coating over a BHJ, or the droplet formation issues of spray deposition. Single walled carbon nanotubes have been shown to make good transparent contacts for OPV devices already, but have not yet been used as a back contact due to processing conditions that would destroy the underlying layers. This work circumvents the processing issues and utilizes SWCNTs as a semitransparent back contact in inverted OPV. Silver nanowires are one of the best prospects for low cost transparent conductors for PV applications. We are able to laminate AgNW contacts without having to submit the underlying organics to drying conditions or solvents.

Devices in this work are fabricated by hot-press lamination, as demonstrated in earlier work [116]. In lamination, the top metal electrode is deposited onto a flexible substrate. This metal electrode is then coated with additional organic layers, and subsequently pressed onto the bulk heterojunction of an otherwise complete device on a glass substrate (Fig. 3.1.1.A). This is contrasted with evaporated contact devices, in which all layers except the top metal contact are spin coated sequentially on top of the ITO electrode. An evaporated device is completed when the metal electrode is evaporated over the organic layers.

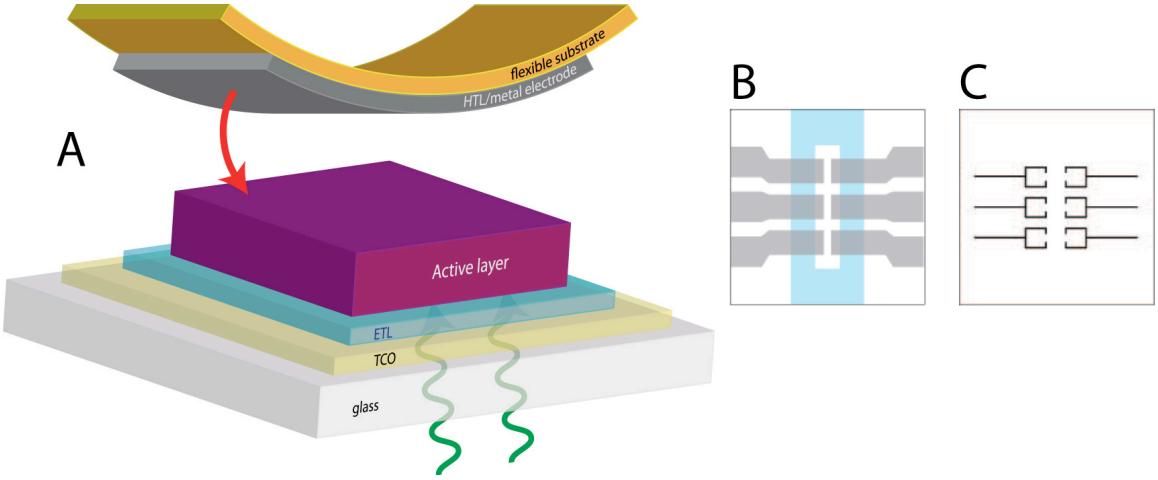


**Figure 3.1.1.** (A) A schematic showing the lamination process. The device is completed when the flexible electrode is laminated to the active layer. In this work different adhesive interlayers as well as different top electrodes are used. (B) The device geometry used in this work. The active layers are sandwiched between the underlying blue ITO and the grey electrodes laminated on top. (C) The bus bar pattern used for PEDOT:PSS:d-sorbitol only electrodes

Laminated devices have similar or better PV properties than identical devices made with metal evaporation [116]. Lamination enables isolation of electrode processing from the active layer. This allows for electrode materials and treatments to be used that would otherwise damage or destroy the device. Other advantages shown in this work include: More fabrication steps can be done in air. Lamination is compatible with metal free and semitransparent contacts, as well as roll to roll processing. Laminated devices are encapsulated on both sides. The step of using barrier layers can be trivially integrated into the fabrication of the device. Our previously published standard demonstrates that lamination is a viable technique for OPV device fabrication. In this work, our standard technique (summarized in the following section) is modified to work with new adhesives electrode materials that are both transparent, and difficult or impossible to implement into inverted devices without lamination.

The materials and methods are examined using a P3HT:PCBM bulk heterojunction active layer. All devices have the same bottom half of the OPV device, while the top, flexible contact and adhesive layer are varied. Results demonstrate the use and processing of these readily-available materials for semitransparent, metal-free devices with no vacuum step in their fabrication procedure. Although optimization of each approach is not the goal of this work, a route to further optimization is suggested for each electrode studied.

### 3.1.1. Lamination Without PEDOT:PSS

In our previous lamination work, it was shown that lamination with no interlayer between the electrode and active layer made poor devices [116]. PEDOT:PSS:d-sorbitol acted as both the adhesive and as a hole contact modifier for the silver electrode. In an attempt to isolate these two roles, lamination using the d-sorbitol adhesive without PEDOT:PSS is performed here. This will allow for different materials to be laminated in the future, including electron selective contacts instead of the hole collecting PEDOT:PSS contact modifier.

### 3.1.2. PEDOT:PSS as a Transparent Electrode

PEDOT:PSS is then used as a transparent electrode. D-sorbitol, used earlier for its adhesion properties, also increases the conductivity of the polymer film by three orders of magnitude [111]. The mechanism of this conductivity increase involves the sublimation of d-sorbitol, and the reorganization of the PEDOT:PSS into the voids left behind [111]. D-sorbitol also changes the work function of the final film, decreasing it from 5.1 eV to 4.9 eV[111]. In our previous work, the decreased work function of the PEDOT:PSS:d-sorbitol did not affect the device voltage when compared to pristine PEDOT:PSS [116]. PEDOT:PSS is relatively transparent to optical wavelengths when it is used as a thin film. When used solely as a hole transport layer, PEDOT:PSS films are generally ~30 nm thick. When 10% d-sorbitol is added to the suspension and spin coated in identical conditions, the film is ~275 nm thick after annealing. This much thicker, mostly d-sorbitol, film is more transparent than the PEDOT:PSS only film (Fig.

3.3.2.1.B), and is much more conductive [111]. Pure d-sorbitol films are insulating, but PEDOT:PSS:d-sorbitol films prepared here have conductivities ~3 orders of magnitude higher than pure PEDOT:PSS ones.

Because of its transparency and conductivity properties, PEDOT has been used as a semitransparent contact for OPV devices by others in the past [69, 70, 117-119]. It is also the most widely used hole contact in OPV. In inverted devices, PEDOT:PSS is used between the active layer and the metal electrode. If the electrode is silver, PEDOT:PSS allows the device to perform optimally upon fabrication, as opposed to having to wait for the silver to age over a few days [55]. PEDOT:PSS is aqueous, and poor wetting prevents its easy deposition onto hydrophobic active layers. Solutions include additives such as surfactants [79], spray coating [69, 70] or potentially damaging plasma or UV ozone treatment of the active layer. Spray coated films tend to be less conductive due to barriers at droplet boundaries. Lamination is a useful procedure to ensure physical and electrical contact between the active layer and the PEDOT:PSS electrode with the addition of d-sorbitol, but no other additives or surfactants, and no problems with droplet formation or active layer damage due to oxygen plasma or UV ozone. Due to its low conductivity, a bus bar pattern (Fig 3.1.1.C) is used beneath the electrodes to laterally conduct current from the electrode to the electrical contact for wire connection. The device area is entirely PEDOT:PSS:d-sorbitol, the metal simply aids the current from the device to the electrical connect across the substrate.

### 3.1.3. Single Walled Carbon Nanotubes

Single walled carbon nanotube films may present several advantages over alternatives either as a transparent conductor, or as a thicker, non-transparent electrode [25, 120-123]. SWCNT's have been demonstrated as the bottom contact of an OPV device [120], but have not successfully been used in an inverted structure. The nanotubes themselves have very low resistances, but in a film of them, resistance arises from the junctions between tubes. The transparency of the tubes is due to the separation between the light-absorbing tubes in the network that makes the film [123, 124]. SWCNT's can be sprayed in a variety of thicknesses in order to balance light transmission and conductivity [120]. Because we are using them as the back contact, films are sprayed to optimize conductivity at the expense of lower transparency. As prepared, SWCNTs are ~2/3 semiconducting, and ~1/3 metallic. Redox dopants are found to increase the delocalized carrier density and transmission probability through intertube junctions more effectively for semiconductor-enriched films than for metal-enriched films. As a result, redox-doped semiconductor-enriched films are more conductive than either intrinsic or redox-doped metal-enriched films [121].

Carbon nanotube films are prepared as in previous work [122]. In brief, the SWCNTs are ultrasonically sprayed from a SWCNT ink with a CMC surfactant. Soaking the film in nitric acid simultaneously dissolves the surfactant and p-type dopes the semiconducting nanotubes in a redox reaction. The work function of the doped SWCNTs is approximately 5.8 eV, which makes them suitable as a hole collecting contact in a P3HT:PCBM device. The nitric acid

soak makes it impossible to spray the tubes directly onto the active layer of an OPV device. The subsequent necessary acid soak will destroy the underlying layers. In this work, lamination is used to isolate the acid soak step from the other parts of the device, and fabricate inverted OPV devices with a SWCNT top electrode.

### 3.1.4. Silver Nanowires

Silver nanowires provide an opportunity for metallic contacts without the need for a vacuum deposition step. Due to the separation between the wires, AgNW films are semitransparent. This makes them a potential replacement for ITO as a transparent conducting contact. Their macroscopic transparency and conductivity properties make them ostensibly better candidates for ITO replacement than SWCNT films [25]. On the microscale, the gaps between wires are too large for free holes to travel laterally across the bulk heterojunction to be collected. This suggests a hybrid between the relatively wide-open AgNWs and a lower conductivity but fully coating PEDOT:PSS:d-sorbitol film [125]. Since the AgNWs are sprayed from an IPA suspension, lamination is not inherently necessary, but it does isolate the organic layers from the spraying, drying, and annealing conditions required by the AgNWs. There is evidence in literature that even a poor solvent can cause the P3HT to swell, and promote changes in microstructure within the blend [52]. Lamination also provides a clean, smooth PET substrate for AgNW deposition, rather than multiple layered organics.

### 3.2. Experimental

All devices in this work start with patterned ITO on a glass substrate. A ZnO electron transport layer is made by spin-coating then annealing a sol-gel precursor [126] over the substrate. The P3HT:PCBM active layer is spin-coated over this ETL.

All control devices are made as follows: On a flexible substrate, 100 nm of Ag is thermally deposited onto PET. This film is then coated with Baytron 4083 PEDOT:PSS mixed with d-sorbitol in a 10% by weight mixture. The PEDOT:PSS:d-sorbitol is spin-coated twice onto the Ag electrode at 2000 RPM to produce a film roughly 350 nm thick. This tenfold increase in thickness is consistent with a tenfold increase in solids in the film, and means that the film is mostly d-sorbitol with in interpenetrating network of highly conductive PEDOT:PSS. This flexible substrate is pre-annealed for 10 minutes at 115 ºC to remove water from the PEDOT:PSS before lamination. The two substrates are then laminated together to complete the device. During the lamination step the layers are pressed for 5 minutes between heated plates at 130 ºC and 275 psi. All steps after the thermal evaporation of metal onto the PET are done in ambient atmosphere. Devices with alternative adhesives or electrode materials use this standard procedure with the following changes:

When d-Sorbitol as an adhesive layer for Ag Film Electrodes, d-sorbitol is first dissolved in water in a 5% by weight solution. This solution wets the silver/ PET substrate poorly, so it is then diluted with IPA in (H20:Sorbitol):IPA ratios of 1:1, 1:3, or 1:7. This mixture is spin-coated onto the patterned silver electrode on

a PET substrate at 2000 RPM. D-sorbitol is an electrical insulator, so the layer must be thin enough to allow tunneling of current. These substrates are then laminated to the active layer to complete the device.

Devices with transparent PEDOT:PSS contacts are made as follows: A silver bus bar pattern is evaporated through a shadow mask onto a flexible PET substrate (Fig 3.1.1.C). This substrate is then coated with the PEDOT:PSS:d-sorbitol recipe used above. In this case the PEDOT:PSS acts as the entire contact, rather than a hole modifier for the silver contact. The PET/Ag busbar/ PEDOT:PSS:d-sorbitol substrate is laminated onto the bulk heterojunction to complete a device in place of a metal electrode.

SWCNT films were prepared as in Tenent et al. [122]. Since they are being used for the non-transparent back electrode in this work, thick films (~80 nm) with little transparency (~40%) are used. Devices are laminated with SWCNT electrodes in 2 different treatments: As cast (freshly doped) SWCNTs, and SWCNTs coated with PEDOT:PSS:d-sorbitol.

Silver nanowire films are prepared by ultrasonic spray deposition of silver nanowire solutions in IPA onto PET substrates. Silver nanowires with an average diameter of 115 nm were purchased from Seashell Technologies (La Jolla, CA) and used without additional modification. Film transparency and thickness are controlled by the number of passes of the spray head. The films used here have a sheet resistance of 15 Ω/□ and a transparency of 55% across the useable portion of the spectrum (Fig 3.3.4.1.C). Devices are laminated with 3 treatments: bare NW films, NWs coated with a solution of d-sorbitol in water (5% by weight),

and NW's coated with PEDOT:PSS:d-sorbitol (used in controls). These films are laminated onto a bulk heterojunction to complete the OPV device.

Devices are characterized with current-voltage measurement under simulated solar light from a xenon arc lamp calibrated to solar intensity using a silicon diode with a spectral mismatch of 1.1. Due to the high conductivity of the PEDOT:PSS:d-sorbitol layer used in some devices, all devices are apertured using a .0514 $cm^2$ shadow mask. Nominal dark device area is 1.1 $cm^2$. Device series resistance ($R_s$) is measured as the inverse slope of the *J-V* curve at +1V.

### 3.3. Results and Discussion

#### 3.3.1. D-Sorbitol as an Adhesive Layer for solid Ag Film Electrodes

Device yield of the 1:7 ratio adhesive layer is 50% due to the sensitivity of the devices to the thickness of the adhesive layer. The 50% that work have the best performance of all PEDOT free devices. This suggests that there is a narrow range of correct d-sorbitol thicknesses when it is spin-coated over Ag as a contact adhesive. The layer must be thick enough to promote adhesion while being thin enough to allow for tunneling of charges into the Ag. Series resistance of the functioning 1:7 devices is similar to that of the PEDOT:PSS control (Table 3.3.1.1.). The slightly higher short circuit current and reduced fill factor of the 1:7 devices is consistent with bare Ag contacts, as opposed to PEDOT:PSS coated contacts. We conclude that the (d-sorbitol:H20):IPA mixture needs to be quite dilute. Charges either tunnel through the thin sorbitol layer or make ohmic contact in the gaps between sorbitol patches in the adhesive film.

Lamination of bare contacts using only d-sorbitol as an adhesive produces working OPV devices, but the failure rate due to delamination during fabrication of these devices is high, and the performance characteristics are not as good as those with the PEDOT:PSS:d-sorbitol hole modifying adhesive. PEDOT:PSS free lamination is a useful test procedure for devices with alternative electrode materials or treatments, as well as alternative HTLs. Further optimization of the (d-sorbitol:$H_2O$):IPA mixture may provide better wetting on the substrate, and more consistent device performance. This procedure may work differently when the (d-sorbitol:$H_2O$):IPA mixture is spun onto a surface with different wetting properties than a smooth Ag film (See Chapters 4&5).

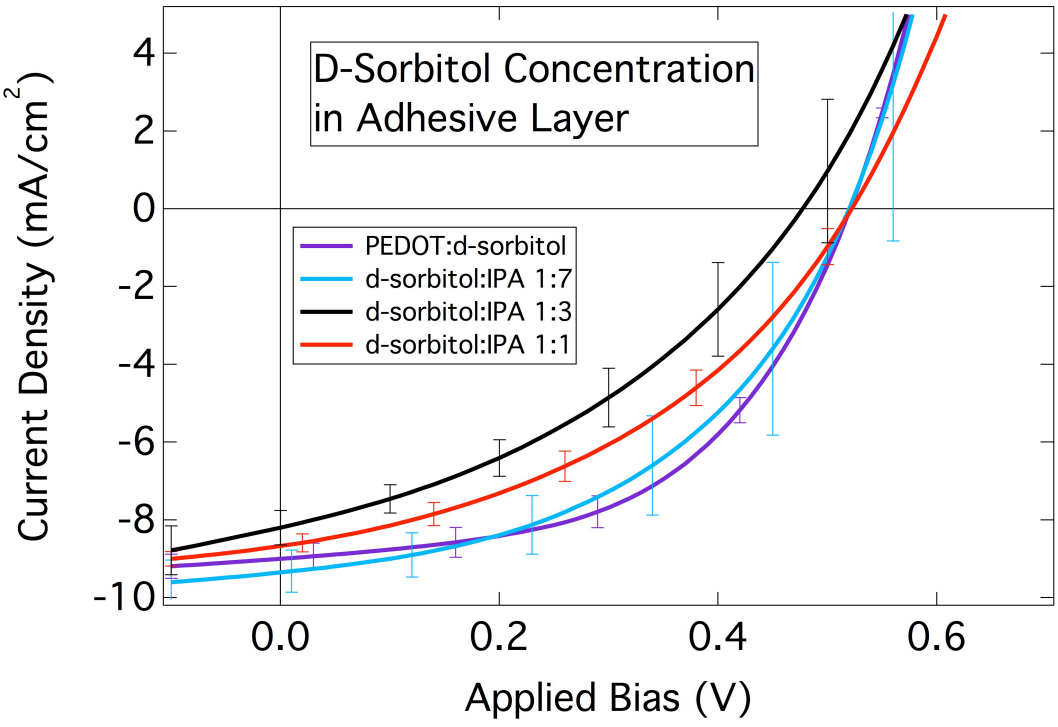


**Figure 3.3.1.1.** Performance characteristics of adhesive layers made from water, d-sorbitol, and IPA in various concentrations. Error bars are standard deviation of the functional devices.

| **Adhesive Treatment** with 100 nm Ag electrode | **Device $R_s$ (Ω)** | **$\eta$ (%) Best / Avg** | ***FF* (%) Best / Avg** | **% Functional (≥6 devices)** |
|---|---|---|---|---|
| Ag/PEDOT:PSS:d-Sorbitol | 40-50 | 2.74 / 2.60 | 56.2 / 55.4 | 85 |
| Ag/Sorbitol:IPA 1:1 | 120-170 | 1.91 / 1.83 | 41.4 / 40.6 | 66 |
| Ag/Sorbitol:IPA 1:3 | 120-250 | 2.09 / 1.52 | 42.5 / 38.2 | 66 |
| Ag/Sorbitol:IPA 1:7 | 40-55 | 2.44 / 2.12 | 47.3 / 47.1 | 50 |

**Table 3.3.1.1.** Properties of devices made with d-sorbitol as a contact adhesive

### 3.3.2. PEDOT:PSS:d-Sorbitol Electrodes

Devices with PEDOT:PSS contacts exhibit good open circuit voltages, but suffer from reduced current and fill factor, and large variation. PEDOT:PSS electrodes are the most transparent of those examined in this work, but are also the most resistive.(Fig 3.3.1.1 and Table 3.3.1.1.). Since PEDOT:PSS:d-sorbitol is already the most effective conducting adhesive for lamination purposes, it is easily incorporated as a semitransparent electrode. PEDOT:PSS electrodes allow for fabrication of metal-free devices. Metal bus bars are used in this geometry to help with the relatively long lateral distance charges must travel to get from the active area of the device to the electrical connect (Fig. 3.1.1.C). There is no vacuum step necessary in the fabrication process. For further optimization, thicker films would have better conductivity properties with minimal absorption increase but may not be effective enough to lead to increases in device fill factors and efficiencies. Given that sheet resistance is inversely related to thickness, it would likely be better to increase conductivity by orders of magnitude than thickness. Higher conductivity PEDOT:PSS variants are available [70, 119], but generally have smaller work functions. The higher

conductivity and lower work function should both theoretically decrease photovoltage, but in our experience with P3HT:PCBM and the d-sorbitol additive in 4083 PEDOT, this has not been the case [116]. Careful formulation, or layering [118] of PEDOT:PSS variants could advance the usefulness of the material as an electrode.

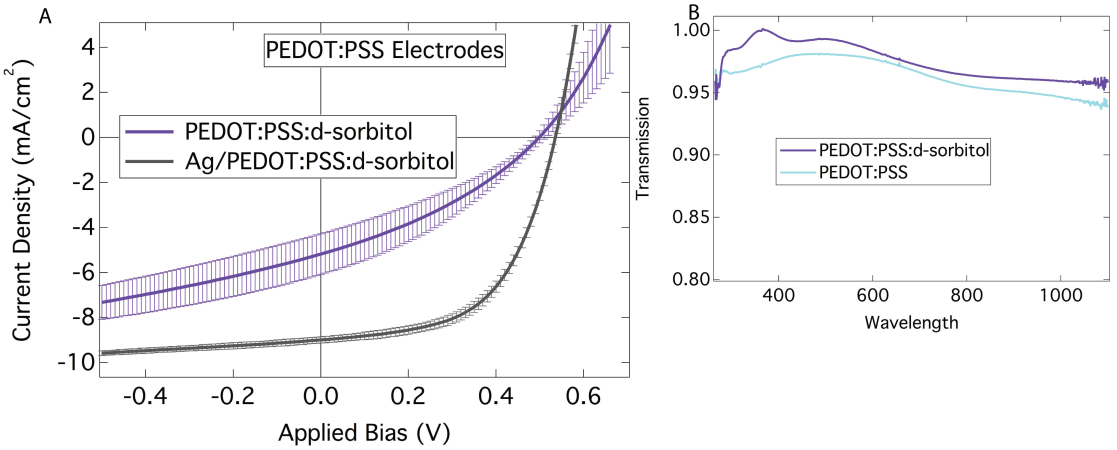


**Figure 3.3.2.1.** (A) PEDOT:PSS as a transparent contact exhibits similar voltage, but poor current and fill factor compared to laminated Ag contacts. (B) Optical transmission of PEDOT:PSS with and without d-sorbtiol, before and after annealing.

### 3.3.3. Single Walled Carbon Nanotube Electrodes

SWCNT devices are laminated with as bare (freshly doped) SWCNTs, and SWCNTs coated with PEDOT:PSS:d-sorbitol. Devices made from bare SWCNTs have poor photovoltaic properties, but have series resistances similar to those made from SWCNTs treated with PEDOT:PSS:d-sorbitol. SWCNT electrodes treated with PEDOT:PSS:d-Sorbitol exhibit much better photovoltaic properties. AFM data shows that the roughness of bare SWCNTs is similar to that of ones with PEDOT:PSS spin-coated over them. Measured RMS roughness is 8.0 nm for coated SWCNTs vs. 4.6 nm for bare ones. (Fig 3.3.3.1.b). Identical $V_{oc}$ of the

SWCNT/PEDOT:PSS devices and the Ag/PEDOT:PSS ones suggest good energy level alignment of the SWCNT/PEDOT contact with P3HT. The series resistance SWCNT devices is 330-600 Ω compared to 40 Ω in devices with Ag contacts.

The SWCNT films used start at at 25 Ω/□. It is found that either annealing at 130 C, spin-coating PEDOT:PSS over the films, or both, will increase the sheet resistance to ~45 Ω/□ (Table 3.3.4.1.). This change in sheet resistivity is attributed to de-doping of the tubes either by heating or washing away of the dopants. For comparison the ITO used as the transparent contact has a sheet resistance of 15 Ω/□ (Table 3.3.4.1.). Figure 3.3.3.1.C shows that the devices are quite attenuating, but still semitransparent. The flat absorption at wavelengths greater than 650 nm is due to the broad absorption of the SWCNT film.

Further optimization should include a variety of PEDOT:PSS:d-sorbitol thicknesses, and bus bars or better geometry to limit *FF* reduction from parasitic series resistance. As shown elsewhere [127] and in this work (Table 3.3.4.1), SWCNT films tend to become more resistive as dopants desorb when exposed to heat or liquids. Newer, more stable dopants [128] may resist desorption and lead to lower resistance SWCNT networks, thus better devices. Isolating the semiconducting SWCNTs would improve the performance of the final electrode compared to the 2/3 semiconducting, 1/3 metallic mixture used in this work.

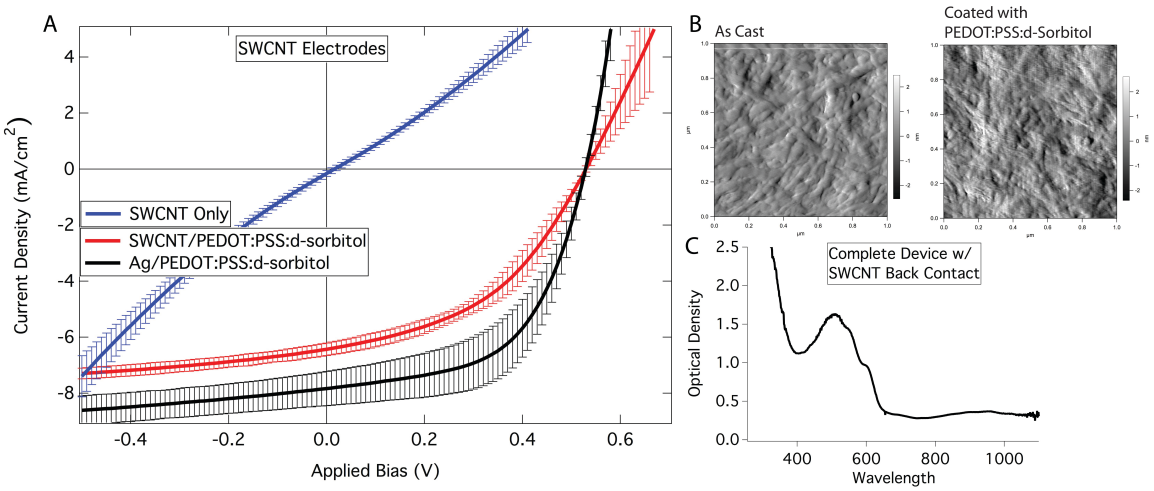


**Figure 3.3.3.1.** (A) PV performance of devices with SWCNT contacts compared to Ag ones. The PEDOT:PSS:d-sorbitol is necessary for good performance of SWCNT electrodes. (B) AFM deflection images of SWCNT films with and without PEDOT:PSS covering layers. Spinning PEDOT:PSS over the SWCNT film does not noticeably affect surface roughness. (C) Optical density of a semitransparent OPV device with SWCNT back contact.

### 3.3.4. Silver Nanowire PEDOT:PSS Hybrid Electrodes

AgNWs with no adhesive could not make measurable devices due to delamination. Wires coated with the d-sorbitol in water solution had poor electronic properties (Fig 3.3.4.1.A). Open circuit voltage of d-sorbitol coated electrode devices is similar to that seen from bare silver contacts, but current and fill factor are both very low. This is due to a space charge buildup of carriers unable to leave the device due to the large gaps between the wires. Nanowire films coated with PEDOT:PSS:d-sorbitol had performance comparable to the Ag:PEDOT:PSS:d-sorbitol controls. Similar currents and open circuit voltages are offset by the reduced fill factor, likely due to increased series resistance of the NW devices compared to the solid Ag film devices. Device resistance of NW electrode devices is 280-340 Ω compared to 40 Ω in control devices (Table

3.3.4.1.). Although PEDOT:PSS does not affect the RMS surface roughness (~50 nm), AFM images show that PEDOT:PSS is filling in gaps between wires (Fig 3.3.4.1.B). This increases the current collecting area and evens out the spatial conductivity of the contact.

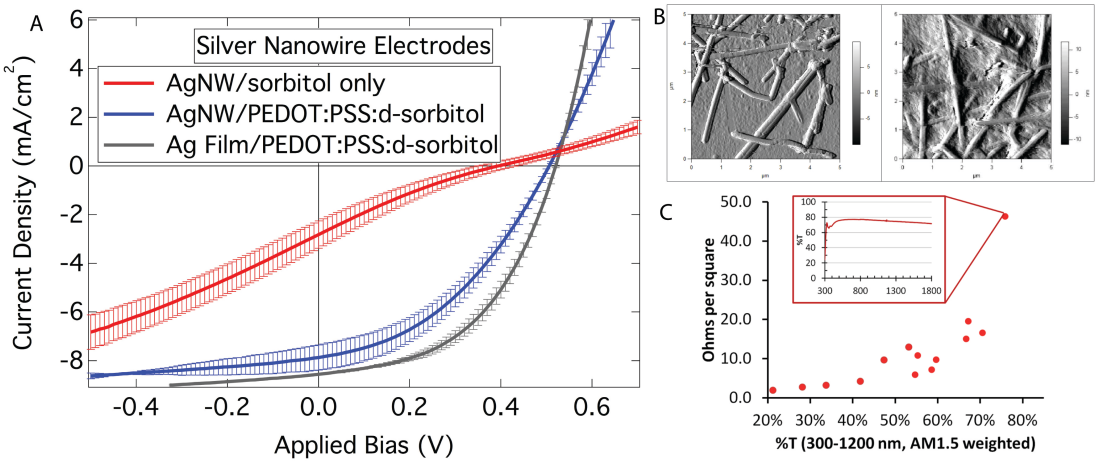


**Figure 3.3.4.1.** (A) PV performance of devices made with Ag NW contacts. (B) AFM deflection images of a bare NW film and one coated with PEDOT:PSS. The PEDOT evens out the spatial conductivity of the film (C) Resistivity vs. transparency and a typical transmission spectrum for Ag NW films. This work used the data point at 55%T and 15 Ω/□ Ultrasonic spray deposition allows the transparency and conductivity of AgNW films to be varied by simply varying the number of passes of the spray head over the substrate.

Given the relatively high performance of AgNW/PEDOT:PSS:d-sorbitol electrodes compared to solid silver films, not much further optimization should be required for this electrode. Solid silver bus bars outside the active area of the device should further decrease series resistance, and increase fill factor off the device. AgNW electrodes are quite comparable in OPV device performance to solid Ag film electrodes and have the advantages of being both semitransparent, and vacuum process free. Although others have demonstrated AgNW devices

without an adhesive or conducting polymer added [129], we were unable to reproduce this result. It is possible that altering the lamination technique with a release film may discourage delamination upon pulling the press apart. It also possible that surface morphology of the nanowire network or bulk heterojunction can be altered to make better mechanical contact between the two. Thicker films or bus bars may decrease resistivity and increase fill factor, but at the cost of transparency and simplicity, respectively.

### 3.4. Comparisons, and Conclusions General to All Contacts

Of the transparent contacts explored, AgNWs coated with PEDOT:PSS:d-sorbitol offer the best PV performance. This is consistent with our AgNW electrodes having the lowest sheet resistance (Table 3.3.4.1.) and with literature showing that AgNWs have a better transparency/conductivity figure of merit than SWCNTs [25]. Although SWCNTs are much cheaper in terms of raw material (carbon vs. silver), AgNWs are currently cheaper to produce and process into useable electrode films than the complicated process necessary to create SWCNT electrodes [122].

Nonreflective contacts result in minimal current loss when used with relatively thick P3HT:PCBM active layers. Many of the new high efficiency polymers are made much thinner due to charge transport properties [91, 130]. For example, optimal active layer thickness for both 6.7% efficient PCDTBT and 4.5% efficient PCPDTBT devices is 100 nm [74, 130]. Devices made from thinner active layers, such as PCDTBT, will suffer more from the absence of back

reflection with transparent contacts. Current loss from lack of back-reflection is an intrinsic issue with a device that is semitransparent by design. This can be mitigated by the use of a diffusive reflector behind the device or by stacking semitransparent cells for increased absorption. The light scattering properties of AgNWs may help this effect, light not absorbed by the active layer is either passed through the device, or scattered diffusely back into it. Back scattering will increase the path length of the reflected light. Although the AgNWs used here are randomly oriented, periodic AgNW networks have been shown to excite surface plasmons on individual wires which increase optical field intensity in the vicinity of the contact, and can be coupled diffractively to maximize transmission through the film or diffractive scattering [131].

In our geometry, much of the electrode material is in the non-active area of the device. The 'finger' of the electrode carries current of the device across an unnecessarily long lateral distance. Bus bars (used with PEDOT:PSS contacts) reduce this series resistance at the cost of additional processing. A different geometry with a shorter distance (or lower resistance) between the device area and the electrical measurement area would increase PCE in any semitransparent devices in which the fill factor is limited by the series resistance. All of the alternative electrode devices explored here have high $R_s$ values when compared to metal electrodes. Silver nanowire electrodes have resistance comparable to current transparent ITO, but are still more resistive than solid silver films. High device series resistance causes decreased fill factor and efficiency.

Comparatively good open circuit voltages of the alternative electrode devices suggest that the energy level alignment is appropriate and is dominated by the PEDOT:PSS:d-sorbitol interlayer. The energetic properties of the materials are adequate, but the lateral conductivity properties need remediation or improvement, especially in the case of PEDOT:PSS and SWCNTs.

| Electrode | Sheet *R* (Ω/□) | Device *Rs* (Ω) | *η* (%) Best / Avg | *FF* (%) | % Functional |
|---|---|---|---|---|---|
| Newly Doped SWCNT | 26 | n/a | n/a | n/a | n/a |
| SWCNT 130 ºC 5 min anneal | 45 | 440-600 | ~ 0 | 25 | 83 |
| SWCNT/PEDOT:PSS | 44 | n/a | n/a | n/a | n/a |
| SWCNT/PEDOT:PSS Annealed | 45 | 330-600 | 1.57 / 1.44 | 45.6 | 83 |
| Ag Nanowires/d-Sorbitol | 15 | ~2500 | 0.35 / 0.24 | 21.7 | 83 |
| Ag NW/PEDOT:PSS:d-Sorbitol | <15 | 280-340 | 1.65 / 1.48 | 40.5 | 83 |
| PEDOT:PSS:d-Sorbitol | ~1000 | 130-200 | 1.01 / 0.87 | 34.7 | 85 |
| Ag/PEDOT:PSS:d-Sorbitol | ~0 | 40-50 | 2.74 / 2.60 | 56.2 | 85 |

**Table 3.3.4.1.** Characteristics and device properties for semitransparent electrodes with different treatments. SWCNT's, AgNWs, and PEDOT:PSS:d-sorbitol films are compared to the standard Ag/PEDOT:PSS:d-sorbitol.

Solid silver films are comparatively robust both chemically and physically when compared to the alternative electrodes presented in this work. All of the alternative electrodes discussed in this work are easily wiped off during patterning for fabrication. This problem is not inherent to the electrode, but the particular geometry used. Care must be taken not to damage the electrodes during patterning and fabrication. Wiping can be eliminated if the PEDOT:PSS

interlayer is masked before deposition, or the interlayer can be deposited onto the other half of the lamination interface. Each solution poses its own set of challenges, masking the electrode must be done in a way that is harmless to the electrode, and depositing PEDOT:PSS onto an organic stack may necessitate wetting additives or treatments.

A note on the AFM images: The images shown are deflection scans. The deflection of the AFM tip is shown. When the substrate is scanned, the height of the measurement is the sum of the tip deflection and change in stage height. Showing deflection only compresses the image, so that details of both large and small features can be seen. Height traces for the 4 relevant electrodes (AgNWs and SWCNTs with and without PEDOT:PSS:d-sorbitol) are in appendix A.

## Chapter 4. Contact Evolution

### 4.1. Introduction

As device efficiencies continue to improve, time evolution, degradation, and shelf-life all become important processes to understand. Devices made in the 'traditional' geometry (electrons collected at the metal electrode) have low work function top electrodes, often Ca, LiF/Al, or Be [56]. Although initially high performing, devices made with low work function contacts tend to degrade quickly in air [23], and must be encapsulated in order to be candidates for large scale solar power generation. Another solution to this degradation problem is to make devices in inverted geometry with higher work function metal contacts that are inherently stable. Inverted OPV devices are often made with silver contacts with or without a hole collecting electrode modifier. Hole collecting layers include the high work function semiconducting polymer PEDOT:PSS, or transition metal oxides such as $MoO_3$[81, 132],$WO_3$[133]or $V_2O_5$ [132, 134]. It is documented (and shown in this work) that inverted devices with P3HT:PCBM active layers and silver contacts perform poorly initially, but improve after a few days in the dark in ambient conditions [55]. This has been attributed to the shift in work function as silver oxidizes . This is not the only available explanation however. White et al have suggested that the performance increase is due to oxygen doping in the active layer of the device [135]. It is also possible that silver sulfide plays a role. This postulation is based on the facts that tarnished silver is predominantly silver

sulfide, and that the sulfur containing thiophene in P3HT may contribute to this process while bonding the hole-collecting Ag electrode to the P3HT in the active layer.

This work uses a previously developed lamination technique [116] to examine the possibility that silver sulfide, not silver oxide, is responsible for the improvement of PV characteristics over time in inverted OPV devices. A series of devices is laminated with silver contacts that are pre-treated to form $Ag_xO$ and $Ag_xS$. PV characteristics of the electrodes and resultant devices are then measured to determine the nature of the performance increase.

## 4.2. Background

The work function of Ag has been documented at 4.3 eV [55](Fig 4.2.1.). This aligns poorly with the HOMO of P3HT at 4.7 eV [136]and induces a poor electric field when paired with a ZnO electron transport layer with a work function near its conduction band at 4.1 eV [137]. Inverted devices perform quite poorly upon fabrication, with $V_{oc}$'s near 120 mV. After storage in dark ambient conditions, $V_{oc}$, $J_{sc}$, *FF*, and efficiency all improve (Fig 4.2.2.). As silver oxidizes, its work function moves 250 mV further from vacuum, nominally from ~ 4.275 to ~ 4.525 eV so the performance improvement has been attributed to the oxidation of the silver electrode [55].

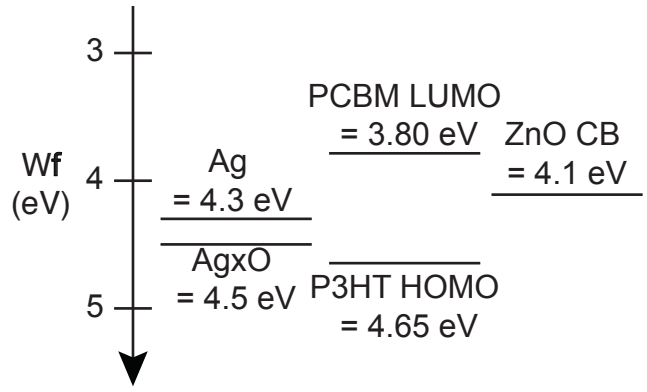


**Figure 4.2.1.** Energy Levels of Silver and Silver Oxide compared to other parts of the inverted OPV system.

The performance change of inverted OPV devices with an Ag electrode without an interlayer is quite drastic. Devices work very poorly upon initial fabrication, but improve over the first few days. See Figure 4.2.2. This time-delayed performance effect is greatly diminished when a PEDOT:PSS interlayer is used. PEDOT:PSS is available with a variety of conductivities, work functions, and wetting treatments. The Baytron 4083 formulation is most often used as a hole collecting interlayer in traditional geometry devices. Without additives to the PEDOT:PSS or treatments to the active layer, wetting between the two is poor, so PEDOT:PSS cannot be spin coated directly onto a P3HT:PCBM active layer. One solution to this problem is to spin coat it over a silver electrode on a flexible substrate, and then laminate the substrate to the active layer of a device [116]. Adding d-sorbitol to the 4083 PEDOT:PSS changes its work function from 5.10 eV to 4.85 eV and increases its conductivity by 2-3 orders of magnitude [111]. Incorporating PEDOT:PSS as an interlayer in an OPV device greatly diminishes the previously documented time evolution gains on the 0-2 day time scale (Fig.

4.2.2.). Devices work almost optimally upon fabrication, and improve only slightly over the first few days of ambient storage. The presence of PEDOT:PSS decreases the $J_{sc}$, increases the *FF*, and does not alter the $V_{oc}$ to make a cell with a higher efficiency than Ag contacts alone.

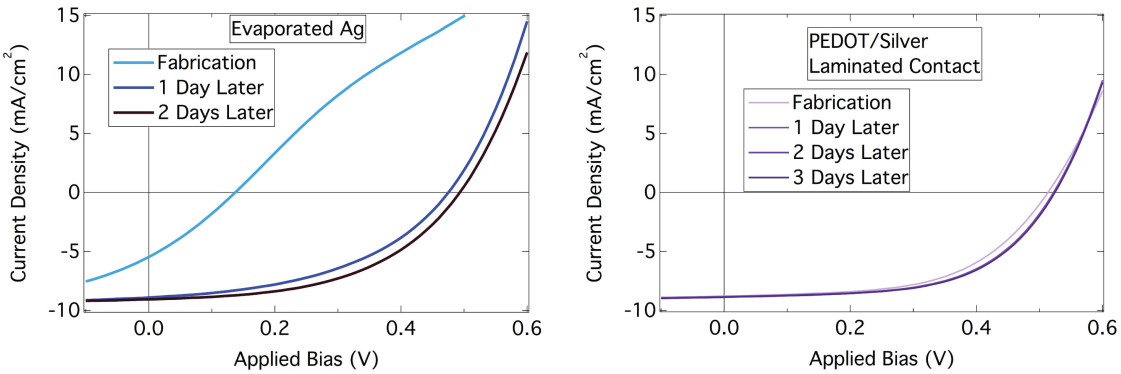


**Figure 4.2.2.** Time evolution of inverted devices with Ag contacts on the left compared to inverted devices with PEDOT:PSS treated contacts on the right

## 4.3. Experimental

Inverted OPV devices were fabricated using five different contacts. All devices start with a sol-gel processed ZnO electron collecting layer and a P3HT:PCBM active layer on ITO coated glass. 100 nm silver films were evaporated onto flexible PET substrates. Silver films were either treated with an aqueous ammonium sulfide solution to produce silver sulfide, or a light oxygen plasma to produce silver oxide. These substrates along with untreated silver ones were then coated with an adhesive made from d-sorbitol:$H_20$:Isopropanol solution in a .05:1:0.8 weight ratio. The adhesive was wiped from the active area of the device. The 1-inch square substrates were then laminated in a hot press with 275 pounds of force at 130 °C for 5 minutes. Other controls were made by laminating PEDOT:PSS:d-sorbitol coated silver electrodes, or evaporating silver

directly onto the active layer without any interlayer. Work functions of the electrodes were measured with a vibrating kelvin probe. *J-V* measurements are taken under simulated solar conditions. Because of the high lateral conductivity of the PEDOT:PSS:d-sorbitol, all devices are apertured to 0.0514 $cm^2$.

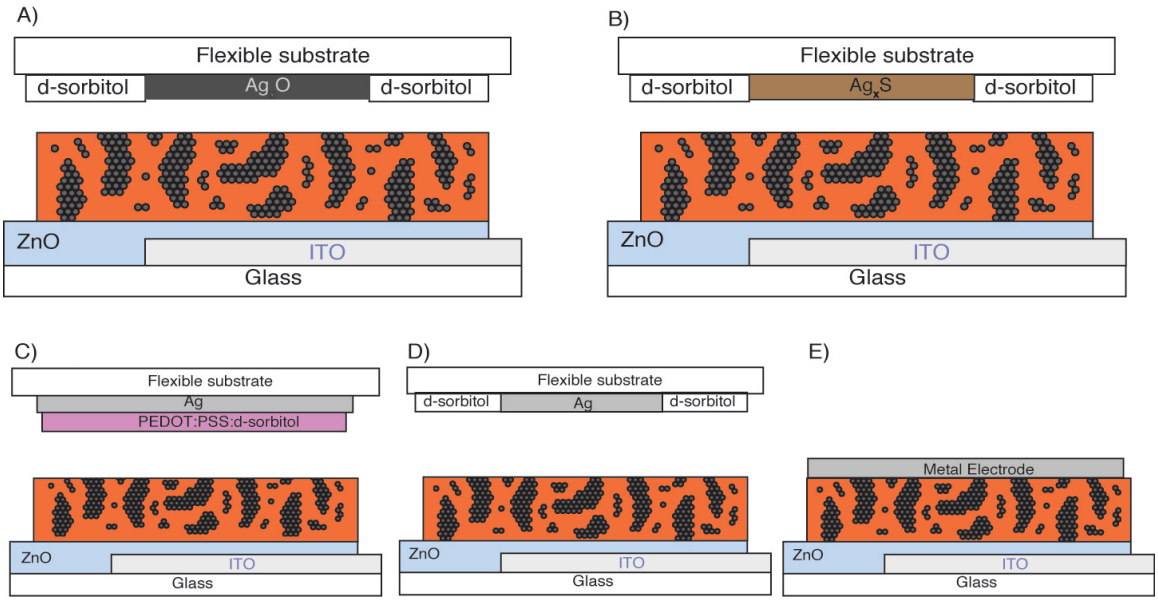


**Figure 4.3.1.** Various device structures used in the experiment. (A-D) have laminated contacts while (E) has evaporated silver.

## 4.4. Results

PV characteristics of different top contacts are shown in Fig. 4.4.1. Devices made from $Ag_xO$ contacts have higher $V_{oc}$ and fill factor than those from $Ag_xS$. The relatively poor *FF* of the silver sulfide contact device compared to the silver oxide one suggests that silver oxide is indeed responsible for OPV device performance improvement over time. Reduced current in both devices is likely due to the thin, insulating d-sorbitol layer at the lamination interface reducing the active area. This explanation is reinforced by higher series resistance from

devices with the d-sorbitol interlayer (Table 4.4.1.) The lateral sheet resistance of the treated silver electrodes was identical to the untreated ones. Another potential loss mechanism is the reduced back-reflection from the tarnished contacts. Treated $Ag_xO$ and $Ag_xS$ contacts were slightly discolored and hazy in appearance compared to the other electrodes used.

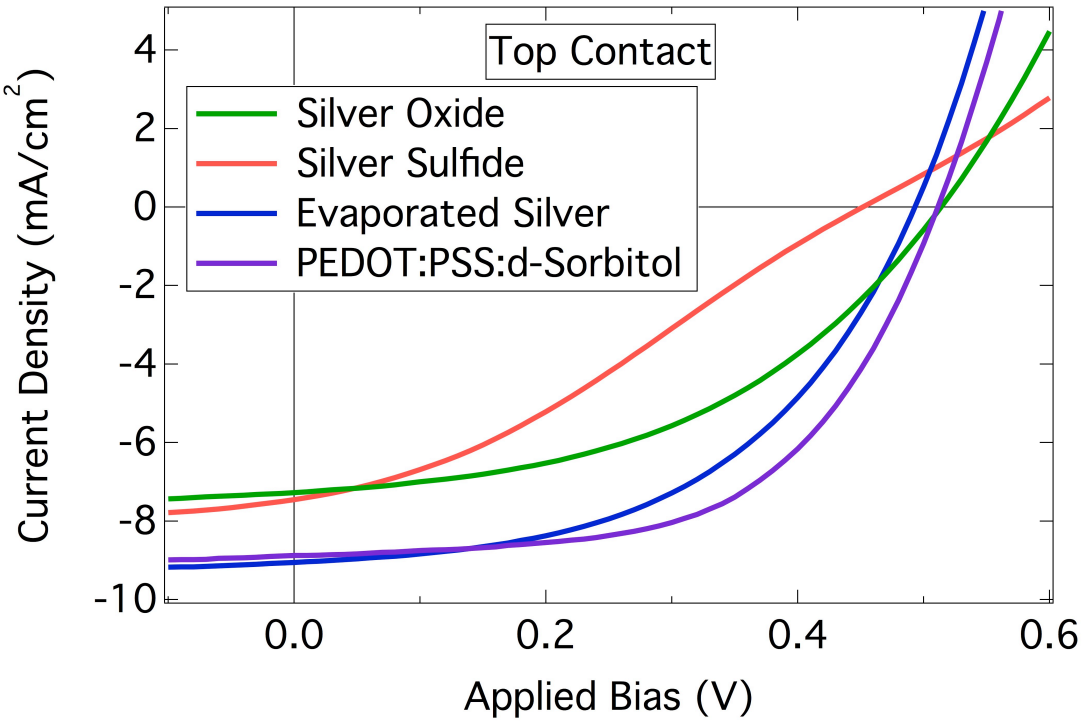


**Figure 4.4.1.** Comparison of different electrodes used. All contacts are laminated except for evaporated silver. Each device is aged 3 days before measurement.

| Back Electrode | $V_{oc}$ (mV) | $J_{sc}$ (mA/cm$^2$) | *FF* (%) | $\eta$ (%) | $R_s$ (Ω) |
|---|---|---|---|---|---|
| Evaporated Ag | 494 | 9.06 | 49.7 | 2.22 | 50 |
| $Ag_xO$ | 514 | 7.28 | 45.2 | 1.69 | 138 |
| $Ag_xS$ | 451 | 7.46 | 31.6 | 1.06 | 920 |
| PEDOT:PSS:d-sorbitol | 511 | 8.89 | 56.9 | 2.59 | 67 |

**Table 4.4.1.** Peak performance characteristics of device contacts

One interesting result was unexpected. Laminated devices were made from 3 different contacts: $Ag_xO$, and nominally pure Ag contacts that were either aged or fresh. Nominally pure silver contacts were either made immediately before fabrication, or 1 week before fabrication and stored in ambient air. Devices from these 3 were indistinguishable from each other (Fig. 4.4.2.). In addition, the laminated Ag contact devices did not age the way that evaporated silver ones do. While evaporated Ag devices take a few days to reach their full potential, laminated ones are as good as they will ever be upon fabrication. The lamination process happens in ambient air, so all contacts are exposed to air immediately before and during lamination. This suggests that the aging effect is happening quickly on the surface of the Ag contact that will be laminated onto the device.

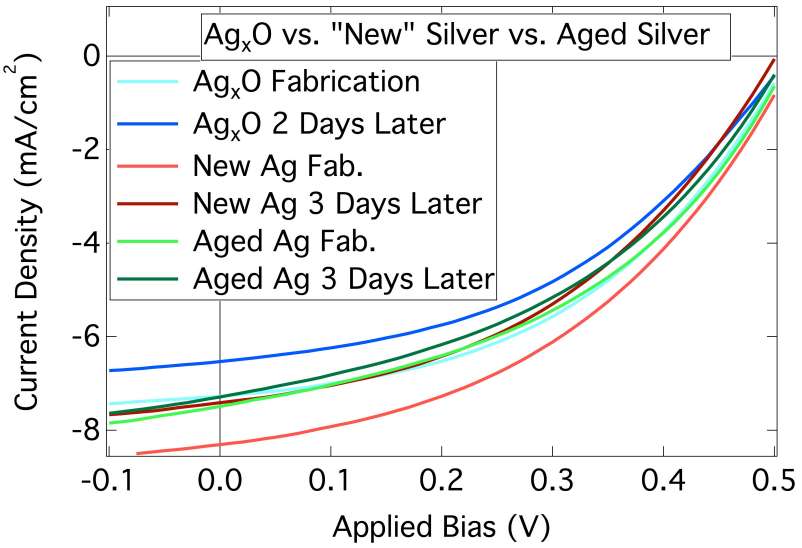


**Figure 4.4.2.** Old Ag, New Ag, and $Ag_xO$ contacts are indistinguishable from each other in laminated devices.

Work functions of the various electrodes are shown in Fig 4.4.3. The $Ag_xO$ electrode is 270 meV deeper than the PEDOT:d-sorbitol on Ag (which is reported at 4.85 eV on glass [111]). The $Ag_xS$ electrode is 170 meV shallower than PEDOT:d-sorbitol. Pure Ag has a reported Wf of 4.5 eV. This is consistent with the data observed here, but we found that Ag's Wf changed quickly in air. Kelvin probe measurements were carried out in air, showed that the work function decreased by over 400 meV in 20 minutes. This is the opposite direction measured by Lloyd et al. over the course of many days [55]. In order to find agreement between the two, a longer term measurement was taken. Silver was moved as quickly as possible from the evacuated evaporation chamber to the measurement probe in air (5 min).

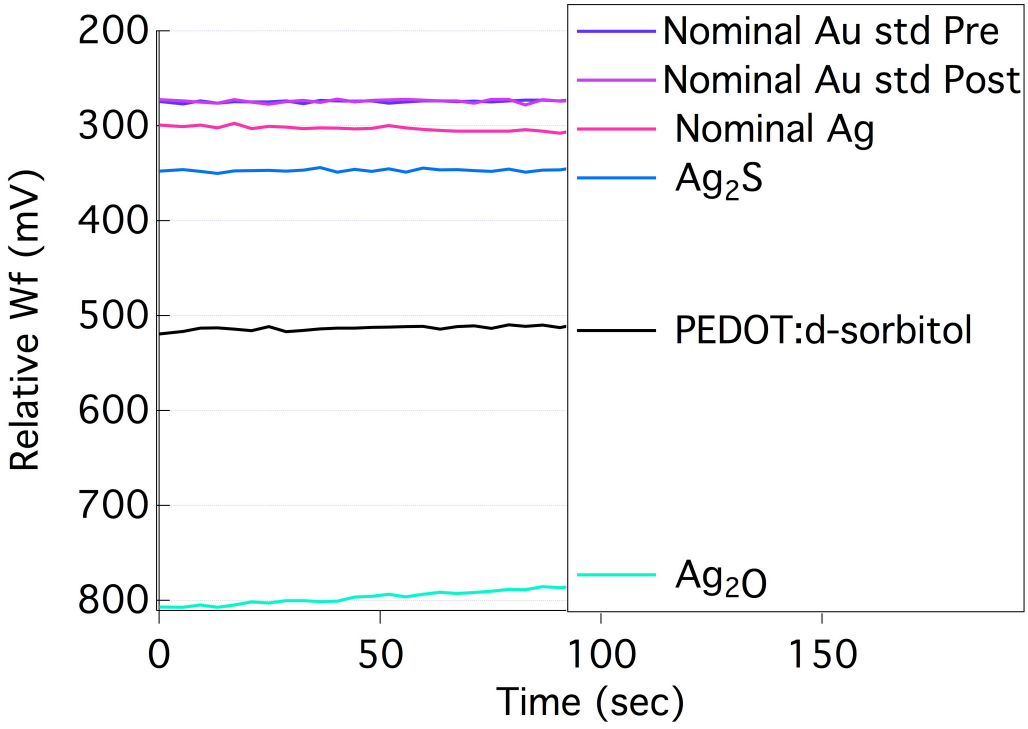


**Figure 4.4.3.** Work functions of the electrodes used in this experiment relative to the vibrating probe tip. Aluminum pre/post work functions are off the axis scale at -701/-713 mV respectively.

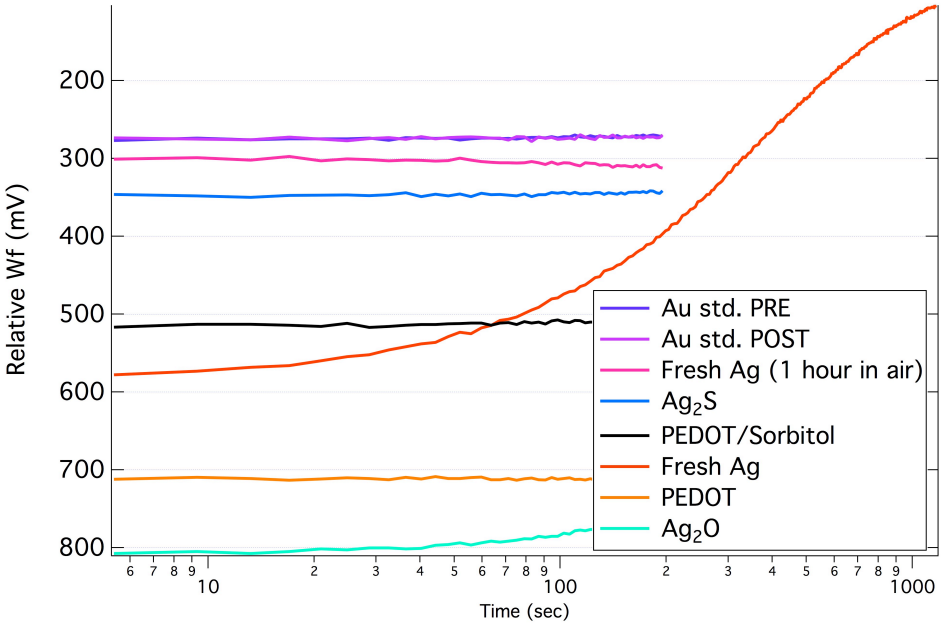


**Figure 4.4.4.** The measured work function of Ag changes quickly upon exposure to atmospheric air.

## 4.5. Conclusions

Although the original intention of this work was to support the claim that silver sulfide is responsible for device improvement in inverted OPV devices, evidence found suggests the contrary. It is more likely that silver oxide is the optimal silver compound for device performance when P3HT is the hole producing polymer. It is possible that $Ag_xS$ may still play a role, but only if the presence of P3HT somehow alters the interface during the $Ag_xS$ formation.

During the course of the experiment, it was discovered that Ag, specifically its measured work function, changes very quickly in air. This measured work function resets and repeats the same path if the sample is removed and re-measured. It is unlikely that the actual work function is behaving as the measurement suggests, but the fact that this effect is only seen with fresh Ag tells us that something about the system is changing in a way unique to fresh Ag. Because of this rapid change, lamination with pure Ag is not practical in ambient air, because it changes instantly and constantly for at least the first few hours. Given the work function of pure silver, and behavior of evaporated devices pure Ag lamination would not likely be preferable for high performance OPV in the first place.

Laminated devices do not age to the same degree as evaporated ones. This indicates that a small amount of surface oxidation on the silver electrode is sufficient for the work function change necessary for optimal performance. The hours long change mechanism noted above is likely accelerated to its conclusion by the heating step during lamination. This suggests that the time scale for

previously noted improvement in evaporated devices is limited by the diffusion rate of oxygen reaching the Ag/BHJ interface. Although some improvement is possible in laminated devices over the first few days (See chapter 2), this improvement does not share the characteristics of that from evaporated Ag electrodes, and is likely a different, less influential mechanism.

The specific mechanism of device improvement with the presence of PEDOT:PSS is also questionable. PEDOT:PSS increases device voltage and fill factor without the need for further aging, but it could be because it alters the Ag contact in a way that makes it favorable for hole collection, or that the properties of PEDOT:PSS itself dominate the interface. The latter is more likely given that recent ellipsometry data shows that the mixed PEDOT:PSS:d-sorbitol films are ~ 275 nm thick. Any electrical properties of the Ag electrode would be masked by the large relative distance between the electrode and the active layer. It can be concluded that in an inverted OPV with a PEDOT:PSS hole collection layer, the purpose of the metal electrode is simply to shuttle current out of the device. The work function and hole collection properties of the device are dominated by the transport layer, and not the metal electrode.

## Chapter 5. Laminated Tandems

### 5.1. Introduction

One fundamental energy loss mechanism in all photovoltaics is the thermalization of charges originating from absorption of photons with energies higher than the band gap of the cell, while photons under the bandgap energy are not absorbed. Another problem specific to organic photovoltaics is the relatively low charge mobility in active layer materials. In some otherwise useful light absorbing polymers, this low carrier mobility necessitates a thinner layer than would be ideal for optimized optical absorption [74, 130]. Both of these issues can be addressed in a tandem structure, in which two bulk heterojunction (BHJ) active layers are stacked in series. The active layers can have complimentary spectral absorption to maximize absorbed sunlight, and they can be thinner than they would in a single junction cell, ameliorating recombination related to thickness issues. An interconnect layer must be used between the two active layers to allow charges to recombine and voltages to add between the two subcells. In our inverted architecture, the ICL acts as a hole collector for the front cell, and an electron collector for the back cell.

One challenge to tandem OPV fabrication is that of orthogonal solvents. Since organic active layers are often soluble in the same solvents, care must be taken to ensure that the solution coating of one layer does not dissolve any of the layers beneath it. One remedy is to evaporate metal or metal oxide buffer layers

to protect underlying organics [94-96]. Another option is to alter one or more of the organic layers to be more chemically robust [97]. In this work, we deposit the active layer of each subcell onto different substrates, which are then laminated together. We use the same P3HT:ICBA bulk heterojunction for both junctions, and choose to focus on the fabrication technique and ICL rather than use complimentary absorbing donors.

The ICL used in this work is a bilayer of PEDOT:PSS and Zinc Oxide. Zinc acetate (ZnAc) is used as a precursor to ZnO on the bottom glass/ITO substrate in single junction cells [137]. ZnAc cannot be used as a precursor to ZnO in the ICL or on flexible substrates because of the high temperature anneal necessary. Diethylzinc in toluene, diluted with THF can be used [23, 138], but not over the BHJ, as both P3HT and ICBA are soluble in toluene. The use of DEZ as the electron collecting part of the interconnect layer requires using structure B from Fig 5.2.1.. Zinc Oxide nanoparticles can also be used with relatively few solvent limitations, and they seem to be popular in literature [82, 139-141]. We were unsuccessful in depositing ZnO NPs onto a BHJ in either a single junction or tandem configuration, so we were limited to DEZ and structure B for fabrication of laminated tandems.

Subcells of the tandem are connected in series. In a series circuit the voltage is the sum of the two subcells' voltages, but due to conservation of charge, both must have the same current. Computational modeling plays an important role in determining optimal layer thicknesses in the device [88][92]. In this work, we model the optical field in the device and study the current's

dependance on active layer thickness in single junction devices in order to match modeled current values with measured ones. We apply the same method developed with single junction devices to tandems in order to maximize current in the tandem device.

An earlier developed lamination technique [116] is used to fabricate tandem devices. Due to the complicated nature of spin-coating the multiple materials in a tandem stack, this work uses lamination as a method to simplify the process. One subcell is constructed on each substrate, and the ICL is deposited onto the glass substrate before the cells are laminated together. (See Fig 5.2.1.B) This “outside in” construction will allow more flexibility with solvents and processing conditions than the traditional “bottom-up” approach.

## 5.2. Experimental

All devices use inverted geometry. Devices were fabricated similarly as in previous work[116]. The flexible substrate has switched from polyethylene terephthalate (PET) to polyethylene naphthalate (PEN), due to the availability of superficially smooth PEN. The active layer is now PV2000. PV2000 is a pre-mixed P3HT:ICBA ink in dichlorobenzene available from Plextronics [142]. Using ICBA as the acceptor increases the open circuit voltage of the cell significantly with a relatively small drop in current [42]. In our laminated inverted single junction cells efficiency increases from 3.19% to 3.56% when switching from optimized P3HT:PCBM to P3HT:ICBA (Table 5.2.1.).

| BHJ | $V_{oc}$(mV) | $J_{sc}$ (mA/cm$^2$) | *FF (%)* | $\eta$ (%) | $R_s$ (Ω) |
|---|---|---|---|---|---|
| P3HT:PCBM | 549 | 10.39 | 56 | 3.19 | 37 |
| P3HT:ICBA | 777 | 7.56 | 60.6 | 3.56 | 74 |

**Table 5.2.1.** Performance characteristics of P3HT:PCBM and P3HT:ICBA single junction cells.

All devices start with ZnO deposition onto patterned ITO. The ZnO is deposited form a Zinc Acetate sol-gel solution as in [137]. For single junction devices, the active layer is spun at 650 RPM for 120 seconds to yield a layer that is 180 nm thick and annealed at 170 °C for 30 minutes. A flexible PEN substrate with evaporated Ag electrodes is coated with a PEDOT:PSS:d-sorbitol adhesion and hole transport layer. The two substrates are laminated at 130 °C for 5 minutes. (Fig. 5.2.1.A)

Because ZnO crystalizes out of solution in the DEZ precursor method, the substrate upon which the DEZ is deposited becomes important. Identical single junction devices are made (ICL C and ICL D) that functionally differ only in the substrate for ZnO formation. The location of the d-sorbitol adhesive also changes, but this is inconsequential to device performance. With ICL C, the ZnO is grown from DEZ over an organic PEDOT:PSS layer. In ICL D, the ZnO is grown over an evaporated silver film (Fig 5.2.1.C, D)

Tandem cells start with a bottom substrate identical to previously mentioned single junction cells. On top of this, an ICL is deposited. The bottom substrate is: glass/ITO/ZnO from ZnAc/120-160nm BHJ/pH7 PEDOT:PSS/ZnO/d-

sorbitol. The top flexible substrate is PEN/Ag/ 4083 PEDOT:PSS/180 nm BHJ. (Fig 5.2.1.B) Due to heating limitations of the flexible substrate, the top BHJ is annealed at 130 °C for 30 minutes instead of the 170 °C of the BHJ on the glass substrate. This minimally alters the performance of the layer (Fig. 5.3.1.). Neutral pH PEDOT:PSS purchased from sigma aldrich and used for the ICL because other forms of PEDOT:PSS are acidic (pH = 1.2 - 2.8 [143]). Acidic PEDOT:PSS will etch or destroy ZnO (See Fig. A in Appendix A). Since PEDOT:PSS in the ICL must be deposited onto the active layer, so the surfactant dynol-604 is added (0.2%) to promote wetting [79].

The ZnO used in the ICL is either formed with the DEZ precursor or with ZnO nanoparticles synthesized as in [144] and dissolved in chloroform. The DEZ precursor is made by mixing .33 M DEZ in toluene with THF in a 1:2 ratio to get . 11M DEZ in toluene:THF. This is done in an inert glovebox and then taken into ambient air for deposition at 2000 RPM for 1 minute and annealing at 115 °C for 10 minutes. The PEDOT:PSS layer is effective in protecting the active layer from the toluene in the DEZ solution and the chloroform of the ZnO nanoparticle suspension.

The d-sorbitol adhesive layer is made from a 10% solution of d-sorbitol in water, which is then diluted 1:10 with isopropanol. This is spun once at 2000 RPM to yield a layer that is ~50 nm thick. Devices are laminated using the same procedure as for single junction devices.

Current-voltage (*J-V*) curves are measured on an AM 1.5G solar simulator with a Xenon lamp calibrated to one sun intensity. The device area of 0.11 $cm^2$ defined by the electrode geometry is inaccurate because of the high conductivity of the pH neutral PEDOT:PSS layer, so an aperture was used to define a device area of 0.0517 $cm^2$ [109, 110]. Active layer thicknesses are determined using a stylus profilometer and compared using UV-Vis spectroscopy.

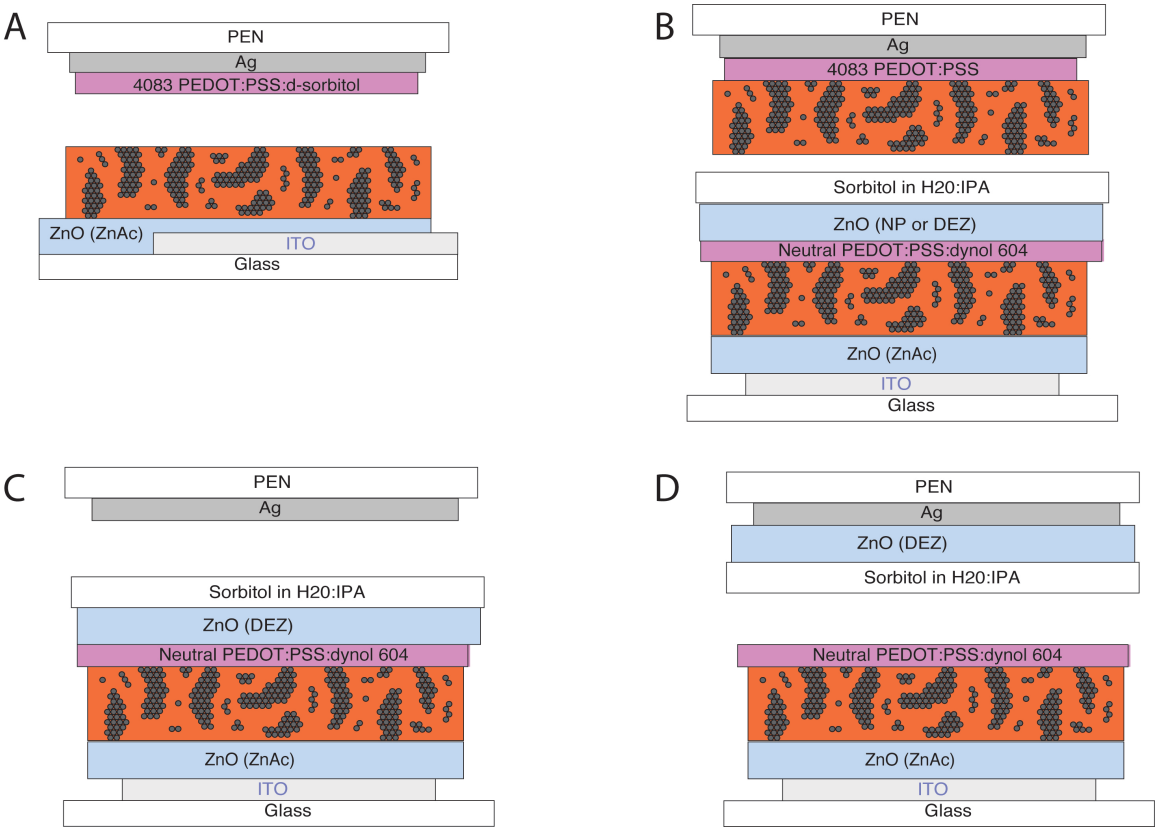


**Figure 5.2.1.** Structure and ordering of layers in devices made in this work. (A) Standard inverted single junction. (B) Tandem Structure. (C) Single junction cell with an ICL with DEZ grown on PEDOT. (D) Single junction cell with an ICL with DEZ grown on top of Ag. Note that structures C and D are identical except for the layer that ZnO is grown on top of, and the location of the d-sorbitol adhesive layer. The blank spaces indicate where the devices were laminated.

## 5.3. Results and Discussion

Single junction cells annealed at 130 °C show only mildly degraded performance compared to those annealed at 170 °C (Fig 5.3.1.). We conclude that reduced annealing temperature does not significantly affect performance of the rear subcell in the tandem device.

Growing the ZnO layer over PEDOT:PSS causes a significant decrease in all PV properties ($V_{oc}$, $J_{sc}$, and Fill Factor). The proposed reason behind this difference is that when the ZnO is grown over PEDOT:PSS, it crystalizes irregularly. Voids form between the PEDOT:PSS and ZnO layers. These voids inhibit current collection by decreasing the active area of the device, and decrease voltage by increasing space charge at the ZnO/PEDOT interface. Growing the ZnO on Ag produces better performing devices. Although not possible in a tandem structure, this demonstrates one reason for nonoptimal performance of ZnO from the DEZ precursor in the ICL of the tandem.

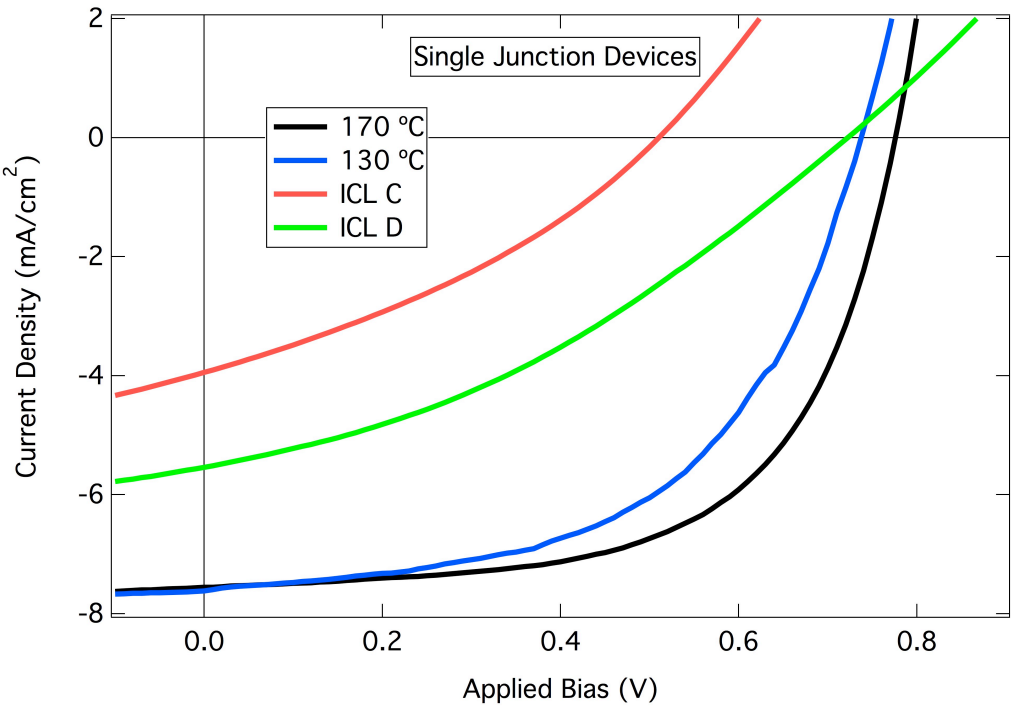


**Figure 5.3.1.** JV curves for single junction cells. ICL structures C and D both use active layers annealed at 170 °C. ICL performance is dependent on whether ZnO is formed on top of a Ag, or PEDOT:PSS. See table 5.3.1. for numerical values.

Zinc oxide nanoparticles are examined using photoluminescence (PL) measurements. A broad emission peak centered at 580 nm emerges when ZnO NPs are excited at energies higher than the band gap (Fig 5.3.2.A). 580 nm light corresponds to an emitted photon energy of 2.13 eV. Since we know the ZnO is highly n-doped, we assume that the photoluminescence comes from a defect state near the conduction band of ZnO that is ~2.1 eV above the valence band [145] . This mid-gap defect state ~0.8 eV below the conduction band in the ZnO NPs acts as a trap for electrons and degrades the voltage of the cell (Fig 5.3.2.B).

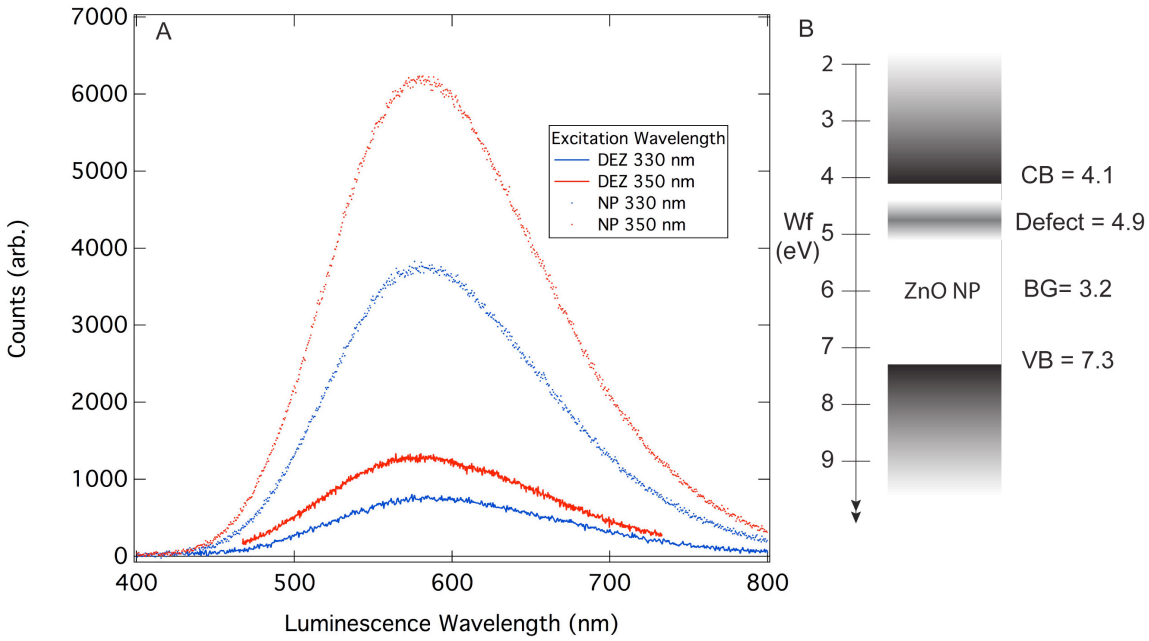


**Figure 5.3.2.** (A) Photoluminescence of ZnO NPs and ZnO formed from DEZ. Films are pumped at 330 and 350 nm. A broad emission peak at 570 nm is indicative of defect states prominent in nanoparticle ZnO and less so in than that formed from DEZ. (B) Band structure of ZnO NPs showing the location and approximate width of the defect state.

In order to determine optimal thickness and predict values for the matched current in the subcells of the tandem, the following procedure is utilized: Using a program based on the optical transfer matrix method [98], current is calculated as a function of thickness for single junction inverted cells. The program is purely optical. It assumes 100% EQE; meaning that every photon absorbed in the active layer produces an electron that is collected and used. In order to scale the calculation to account for non-unity EQE, a series of single junction cells with varying thickness are constructed. The short circuit currents of these cells are plotted on the same axes as the calculated currents, and a scalar is multiplied by the calculated current curve to align it with the data points. In this work, the scalar is 0.46. The new adjusted current curve can now be used to estimate $J_{sc}$

in an actual device as a function of thickness. Results are shown in Fig 5.3.3. Note that above ~200 nm, the model is no longer applicable because currents become limited by recombination rather than absorption near this thickness. The same scalar obtained from the single junction calculation is then used in a double junction one where making an array of device thickness is impractical. The results are shown in Fig 5.3.4 Keeping in mind the ~200nm upper limit for BHJ thickness, the optimal current is ~4 mA/cm$^2$. This optimal current is calculated for a tandem in which the front cell is 120 nm thick and the back cell is 180 nm thick.

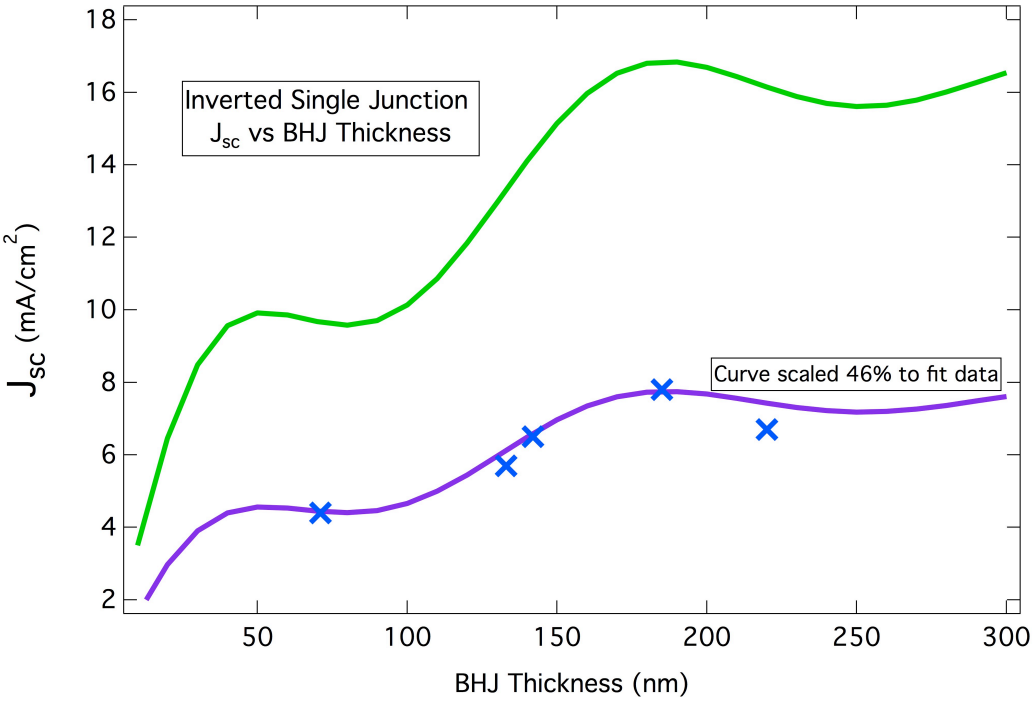


**Figure 5.3.3.** Green: Calculated $J_{sc}$ vs. Active layer thickness via optical absorption modeling with 100% external quantum efficiency. Blue crosses: Actual $J_{sc}$ data from various active layer thicknesses. The point at 220 nm shows the breakdown of the model with thicker layers due to mobility / charge recombination effects. Purple: The green curve is multiplied by a scalar to fit actual data.

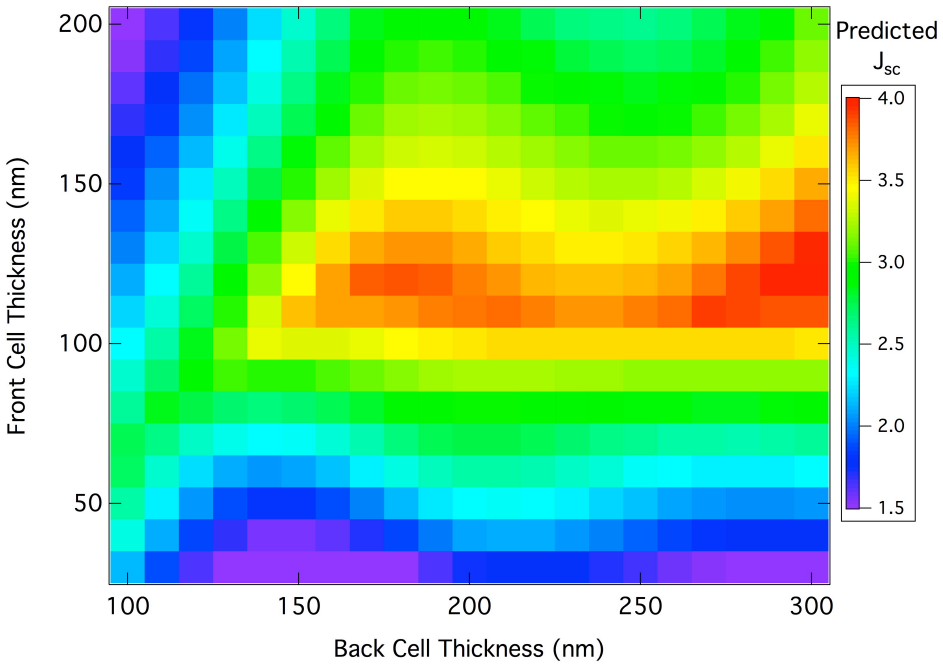


**Figure 5.3.4.** Predicted short circuit currents from various front and back cell active layer thicknesses in a tandem junction device.

Since the current of the back cell is limited by recombination rather than absorption, the maximum single junction thickness of 180 nm is used while the front cell thickness is varied. *J-V* of tandem devices with different ICL ZnO and front cell thicknesses are shown and compared to single junction subcells in Figure 5.3.5. Single junction cells have higher currents due to the benefit of back reflection and lack of absorption from other BHJ layers. Tandems with DEZ based ZnO in the ICL have a $V_{oc}$ of 1.2 V if a thicker front cell is used. Tandems with ~ 50 nm ZnO NPs in the ICL have increased *FF*, $J_{sc}$, and $\eta$, but $V_{oc}$ decreases toward that of single junction cells. A thinner (~ 25 nm, possibly discontinuous) ZnO NP layer in the ICL results in devices with increased $V_{oc}$, but at the cost of decreased *FF*. The $J_{sc}$ of cells with ZnO NPs in the ICL is the maximum we expect from the optical modeling procedure mentioned earlier.

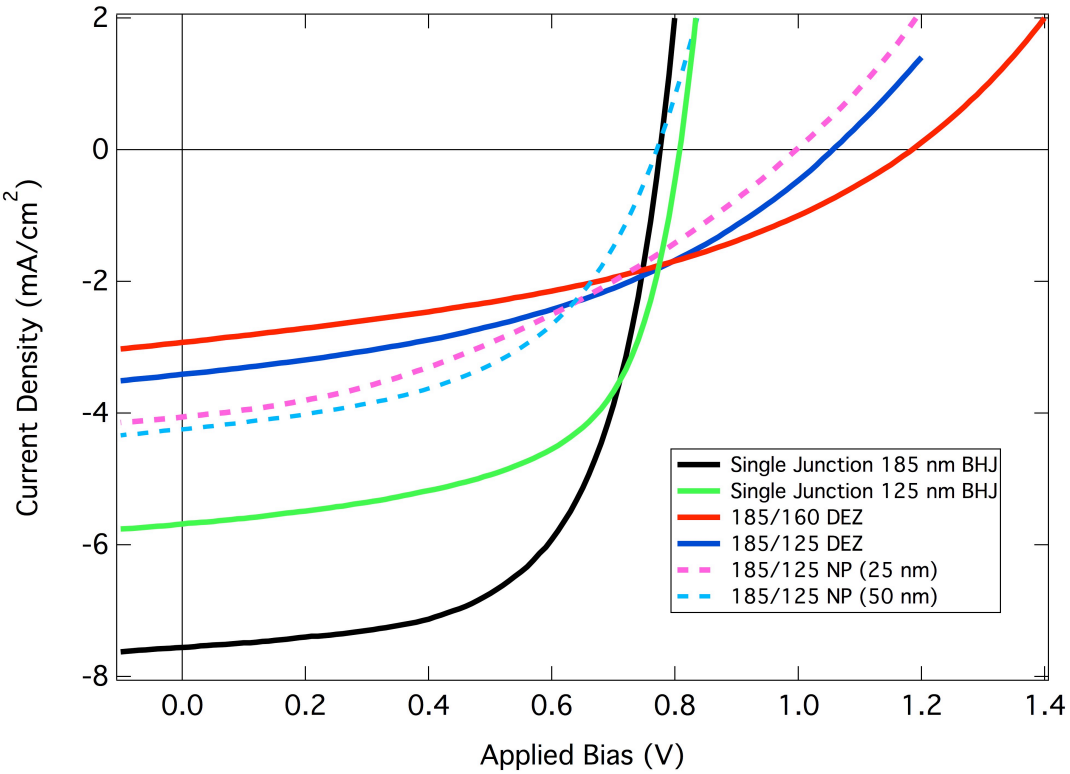


**Figure 5.3.5.** *J-V* curves of tandem devices with different BHJ thicknesses and ZnO composed ICL layers compared to single junction devices

| Device | $V_{oc}$ (mV) | $J_{sc}$ (mA/cm$^2$) | *FF* (%) | $\eta$ (%) | $R_s/R_p$ (Ω) |
|---|---|---|---|---|---|
| Single Junction 180 nm BHJ | 777 | 7.56 | 60.6 | 3.56 | 75/20k |
| Single Junction 125 nm BHJ | 809 | 5.69 | 59.8 | 2.75 | 80/50k |
| Active Layer anneal 130 °C | 739 | 7.60 | 54.1 | 3.04 | 140/2k |
| ICL C | 533 | 4.00 | 33.9 | 0.72 | 1k/6k |
| ICL D | 741 | 5.75 | 36.6 | 1.56 | 1.7k/30k |
| Tandem DEZ 180/160 nm | 1187 | 2.93 | 39.3 | 1.37 | 1.2k/25k |
| Tandem DEZ 180/125 | 1057 | 3.41 | 41 | 1.48 | 1.8k/16k |
| Tandem ZnONPs 180/125 | 771 | 4.25 | 50.5 | 1.65 | 310/14k |
| Tandem ZnONPs (thin) 180/125 | 998 | 460 | 37.1 | 1.50 | 1k/31k |

**Table 5.3.1.** Performance characteristics of devices explored in this work

## 5.4. Conclusions

The goal of tandem OPV is to optimize the current of the cell while obtaining the sum of the voltage of the two subcells with maximal fill factor. In tandems with complementary absorbers, current is maximized by designing each subcell to absorb a different portion of the solar spectrum. Ideally, each subcell operates with the same current in the tandem as it would in a single junction cell. In single junction P3HT based OPV over 90% of incident light within the spectral range of the cell is absorbed. As a result, in a tandem structure with P3HT in front and back cells, absorption will be split between the two subcells, given that they both absorb the same portion of the spectrum. Conservation of energy states that unless charge extraction improves, the efficiency of the optimized tandem (with identical absorbers) should be equal to the optimized efficiency of the single junction device. One modification to this statement is that thinner active layers tend to produce devices with slightly higher fill factor and $V_{oc}$. Another benefit to tandem structures is reduced resistive losses in a cell with higher voltage and lower current, which will favor devices structures with higher voltages and lower currents. In this study, the optimal thickness of the back subcell is equal to that of the optimized single junction cell.

Since the same active layer is used for both junctions, the goal of this work is to double the voltage of the tandem and half the current compared to a single junction cell, while retaining the fill factor of the single junction one. The authors are able to achieve almost double the voltage (1.2 V as opposed to 1.5 V), and we were able to achieve maximum possible currents with 50% *FF*. Unfortunately,

this did not occur in the same device. The zinc oxide used in the interconnect is the limiting layer in each of the tandem cells made. When ZnO NPs are used in the ICL, the voltage is limited by unfavorable energetics from the trap state mentioned in earlier and shown in Fig 5.3.2.. If DEZ is used as a precursor to ZnO, current and *FF* are limited when it is grown over PEDOT:PSS as mentioned earlier and shown in Figs 5.2.1.C/D and 5.3.1. We propose that this is the result of void formation at the ZnO/PEDOT:PSS interface. It could also be due to improper or incomplete precursor conversion, or buildup of organic 'leftovers' after conversion at the organic interface.

Given the relatively large variety of single junction cells that can be made with the lamination process, we propose that the lamination process does not limit the performance of the tandem. Poor tandem performance is a result of either poor ZnO formation or unfavorable energetics, depending on the system used. If this issue were resolved, it is quite likely that lamination can be shown as a valid pathway for fabrication of tandem OPV. One benefit of the lamination procedure is that it provides access to the lamination interface for modifying layers. Because of this flexibility afforded by the process, self assembled monolayers [146, 147] or dopants [60] could be inserted into either side of the lamination interface to tune the properties of the ICL, and to affect its interaction with adjacent absorbing layers.

## Chapter 6. Adhesion at the Laminated Interface

### 6.1. Introduction

This work investigates the mechanism of adhesion between the laminated surfaces of an OPV device. Laminated substrates are mechanically separated while the force is measured. Order of magnitude calculations and estimates of the different possible force mechanisms are calculated and compared to experimental values. The goal is to determine which forces are responsible for adhesion in laminated OPV devices, and to which extent the calculated values of these forces match real world values, thus validating the physical mechanism for the adhesion force. We focus on the interface between the P3HT:ICBA bulk heterojunction and the PEDOT:PSS:d-sorbitol adhesion layer.

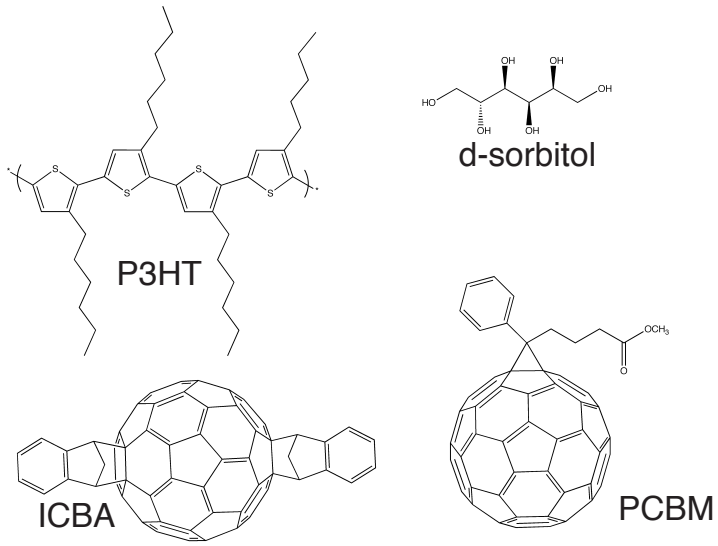


**Figure 6.1.1.** Chemical structures of P3HT, ICBA, PCBM, and d-sorbtiol

## 6.2. Background Information

### 6.2.1. Lamination Interface Background

Although many different lamination structures have been attempted in previous work, the ones that work most consistently are shown below in figure 6.2.1.1. All of the devices shown have d-sorbitol present at the lamination interface. Devices without d-sorbitol were also constructed in previous work, but these devices either performed poorly, or had very low yields due to frequent delamination during fabrication. This is consistent with the initial use of d-sorbitol as an adhesive. Although d-sorbitol is mixed with PEDOT:PSS in a 10% by mass ratio, this is while the PEDOT:PSS is still aqueous. Aqueous PEDOT:PSS is 1%-1.7% solid content (pH neutral is 1.1% solids, 4083 is 1.3-1.7%). A dried PEDOT:PSS:d-sorbitol film is between 87% and 95% d-sorbitol by weight. This is intriguing given that once annealed, PEDOT:PSS:d-sorbitol films are much thicker and much more conductive than the same films without d-sorbitol [111].

The best performing laminated devices are made by laminating a predominantly d-sorbitol layer to an organic bulk heterojunction. Although complete devices can delaminate at the metal/PEN and metal/PEDOT:PSS interfaces, they most frequently come apart at the PEDOT:PSS:d-sorbitol/BHJ interface. This is in comparison to evaporated contact devices, which always delaminate in the bulk heterojunction [148]. This work will focus on adhesion at the lamination interface between (predominantly) d-sorbitol and the BHJ. In addition to being the most frequent delamination point, it is the only interface that is unique to the lamination procedure compared to spin coated and evaporated

devices. The bulk heterojunction (BHJ) used in previous work is either P3HT:PCBM or P3HT:ICBA, in ratios optimized for PV performance (generally close to 1:1).

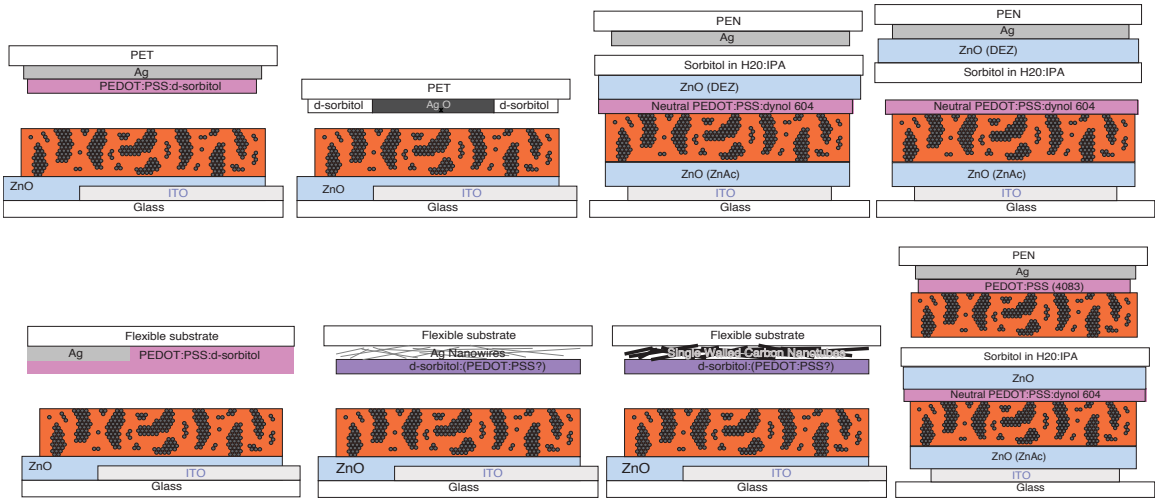


**Figure 6.2.1.1.** Lamination structures used in this dissertation which produce efficient PV devices

### 6.2.2. Dipole - Dipole Bonding

Permanent dipole - permanent dipole bonding is an electrostatic interaction between two dipoles. The dipole moment of a molecule is caused by a partial charge on one side. In a polar covalent bond, one atom is more electronegative than the other, and the wave function of shared electron between the two shifts toward the more electronegative atom. This induces a dipole moment for each bond that points toward the electron deficient atom. Dipoles are attracted via standard electrostatic interaction, in which the energy is given by:

$$W = \frac{1}{4\pi\varepsilon r^3}[\vec{p}_1 \bullet \vec{p}_2 - 3(\vec{p}_1 \bullet \hat{r})(\vec{p}_2 \bullet \hat{r})] \qquad \text{(Eq. 6.2.2.1)}$$

where $p_1$ and $p_2$ are the dipole moments, and r is the separation between them. If the two interacting dipole moments are and parallel, this reduces to:

$$W = \frac{-p_1 p_2}{2\pi\varepsilon r^3} \qquad \text{(Eq. 6.2.2.2)}$$

Differentiating with respect to distance ($F = -dU/dr$) gives:

$$F(r) = \frac{-3p_1 p_2}{2\pi\varepsilon r^4} \qquad \text{(Eq. 6.2.2.3)}$$

This is an attractive force with a $1/r^4$ dependance. Note that this is for two point dipoles, and that the geometry used later will be for two infinite planes.

Hydrogen bonding is a special case of dipole - diplole attraction. Since hydrogen only has one electron, the shift allows a particularly close distance between the hydrogen and the neighboring electronegative atom in the adjacent molecule. Because of the small size of hydrogen relative to other atoms and molecules, the resulting charge, though only partial, represents a large charge density. A hydrogen bond results when this strong positive charge density attracts a lone pair of electrons on another atom, which becomes the hydrogen-bond acceptor. See Fig. 6.2.2.1 for a graphical representation of hydrogen bonding between water molecules.

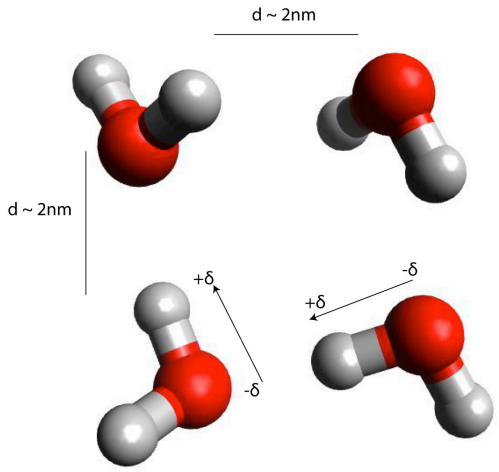


**Figure 6.2.2.1.** Hydrogen bonding between water molecules is a result of the dipole induced by the more electronegative oxygen atom shifting the electron cloud away from the hydrogen atoms

### 6.2.3. Van der Waals interactions

Van der Waals interactions are generally attractive interactions due to induced or permanent dipoles. The 3 main categories in decreasing order of magnitude are permanent dipole - permanent dipole (Keesom force), permanent dipole - induced dipole (Debye force), and induced dipole - induced dipole (London dispersion force). Keesom force (discussed in 6.2.1.) requires that both sides of he interface have permanent dipoles. Debye force is caused by the permanent dipole inducing a shift in the electron cloud of an adjacent molecule, thus creating a dipole in an otherwise nonpolar molecule. London disperson forces are caused by While PEDOT:PSS:d-sorbitol side likely has dipoles from adsorbed water, it is unlikely that there are strong permanent dipoles on the P3HT chain, which will be discussed later. This means that most of the adhesion force will come from Debye and London dispersion forces between the two interfaces.

## 6.3. Macroscopic Delamination Force Measurement

In order to isolate the studied interface, only the bulk heterojunction and PEDOT:PSS layers are spin coated on opposing substrates. The BHJ used in this work is PV2000: a pre-mixed P3HT:ICBA solution. The substrates are laminated using same procedure as with previously demonstrated devices. Force values are obtained by gluing a 1 $cm^2$ force probe to the back PEN side of a laminated substrate. The two sides are pulled apart with increasing force until effectively instant delamination occurs. The time resolution on the force probe is such that delamination appears to happen instantaneously. Forces were recorded 5 times each for lamination of PEDOT:PSS with and without d-sorbitol onto a P3HT:ICBA BHJ.

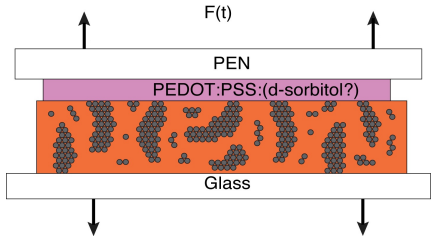


**Figure 6.3.1.** Cartoon of delamination apparatus.

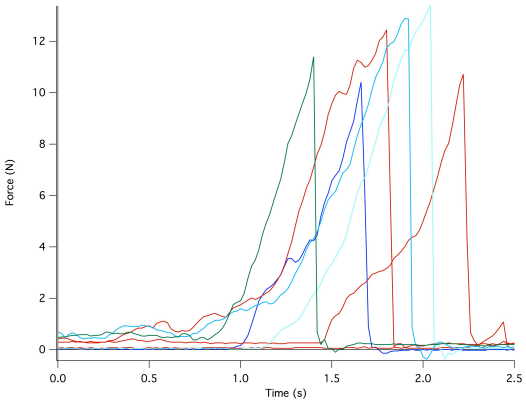


**Figure 6.3.2.** Representative Force vs. Time curves for delamination tests. Force was increased until instantaneous delamination occurred.

| Stack | Delamination Force |
|---|---|
| PEN/PEDOT:PSS/ /BHJ/Glass | 16.7 ± 5.7 N |
| PEN/PEDOT:PSS:d-sorbitol/ /BHJ/Glass | 18.9 ± 6.8 N |

**Table 6.3.1.** Delamination force statistics for 10 devices of area 1 $cm^2$. The double slash marks (/ /) indicate the lamination interface

A note on relating adhesion force to delamination force: In order for delamination to occur, the entire interface does not need to fail at the same time. Delamination can begin at an isolated point on the interface with a very small area (thus high Force per area), and then propagate across the entire substrate. For a comparison, one can look to defect propagation in crystals. The physical system here is obviously different than a limited number of defects in an otherwise perfect, covalently bonded crystal, but there are similarities. In order for forced delamination to occur, separation can begin at a weak point on the interface. The interface is not likely to be homogeneous on the microscopic level, and small inconsistencies in either bonding interface may allow greatly reduced area, and thus increased negative pressures leading to with delamination. When compared to defect propagation in crystals, this may change the delamination force compared to the adhesion force from 1-3 orders of magnitude [149].

## 6.4. Bonding Mechanisms between Lamination Interfaces

Performing lamination in air brings together the solid(s) at the lower interface, the solid(s) at the upper interface, and any contaminants or adsorbed surface species. Given the chemical structures of the materials involved, it is unlikely that any charges are being transferred or covalently shared between the two interfaces upon initial lamination. In decreasing order of bond strength, it is most likely that the interfaces are held together by dipole-dipole hydrogen bonding, dipole-induced dipole van der Waals interaction (Debye force), and induced dipole induced dipole van der Waals force (London dispersion force). Within the solid, semiconducting polymers are predominantly held together by van der Waals interactions [150, 151]. When evaporated devices are pulled apart, failure always occurs within the P3HT:Fullerene layer, although Indene based fullerenes increase cohesion strength by an order of magnitude [148].

Keesom force is the strongest of the van der Waals forces, however in this work, its strength is limited by the relatively small differences in electronegativity between carbon and sulfur, and between carbon and hydrogen (Table 6.4.3.1). Lamination is performed in ambient air, so water is readily available for adsorption onto either surface, specifically the polar hydroxyl groups of the d-sorbitol, and whichever face of the P3HT molecule is shown at the interface.

The Debye force is between the adsorbed water on the PEDOT:PSS:d-sorbitol surface and the nonpolar portions of the P3HT surface, while London dispersion force can act on the remaining nonpolar groups of each interface.

D-sorbitol has both hydroxyl groups to participate in hydrogen bonding with ambient water, and a hydrocarbon backbone to participate in Van der Waals interactions. Its ability to form both types of bonds, as well as its relatively high density of bonding sites (compared to PEDOT:PSS or P3HT) suggests why it is useful as an adhesive in this system. Because of d-sorbitol's high relative bonding density and ability to form both hydrogen and Debye bonds, the BHJ layer is assumed as the limiting material in forming bonds between the two interfaces.

### 6.4.1. P3HT Packing and Surface Density

P3HT has been shown to form lamellar structures [43, 152, 153] (Figure 6.3.1). Using the chain structure, along with separation distance between lamellae in both the *y* and *z* directions allows for estimation of the number density of available bond sites for either permanent or induced dipole bonding.

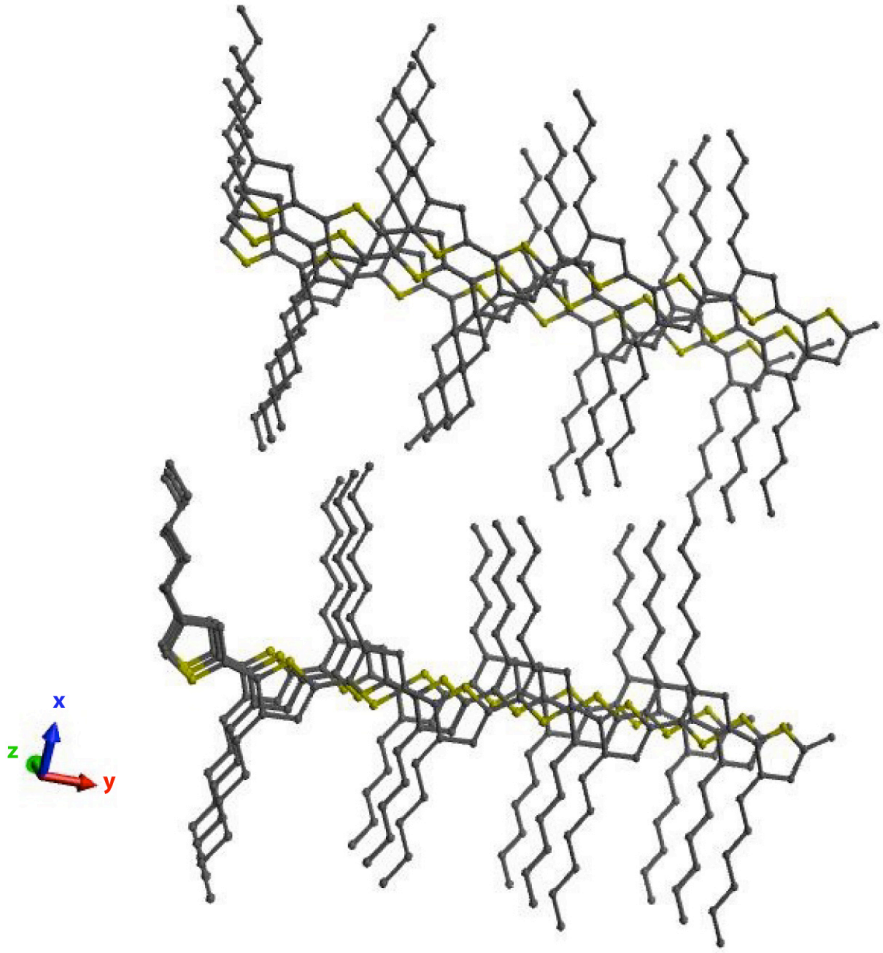


**Figure 6.4.1.1.** Lamellar stacking structure of P3HT. The structure shown here is illustrative, and is not the computed ground state structure.

To begin the 2-D density calculation, we define the unit cell as a simple orthorhombic with one monomer at each corner. As in Fig. 6.4.1., the *x*-direction is parallel to the hexyl side groups, the y-direction is along the conjugated chain, and the *z*-direction is the closest stacking direction between lamellae. In the *x*-vector of the unit cell has length 1.7 nm, the *y*-vector is 0.39 nm, and the *z*-vector is 0.37 nm [43, 152, 153]. From these lengths, one can calculate the surface

area of each face of the orthorhombic crystal, and the surface density of atoms at the lamination interface.

| Face | Exposed Atoms | Area ($nm^2$) | $\sigma$ (Faces/$cm^2$) |
|---|---|---|---|
| *x-y* (flat lamella) | 1 Thiophene Ring, 1 Hexyl tail | 0.64 | $1.6x10^{14}$ |
| x-z (chain end) | 1 Thiophene side (Carbon), 1/2 Hexyl tail | 0.63 | $1.6x10^{14}$ |
| y-z (hexyl tail end) | 1/2 Hydrocarbon group | 0.14 | $7.1x10^{14}$ |

**Table 6.4.1.1.** Properties of the simple orthorhombic unit cell of a P3HT crystal. There is one monomer per unit cell, but due to the regioregularity of the P3HT chain, only every other hexyl tail end exposes atoms for bonding to the interface.

### 6.4.2. Minimum Separation Distance

The adhesion forces explored in this work are highly dependent on the minimum separation distance between the two sides of the lamination interface. While explicit measurement is difficult to perform here, we will form a range of estimates from other known quantities. Hydrogen bonded liquid water molecules are about 2 Å apart [154], so 2 Å will be used as a lower limit for separation. The pi-stacking distance of crystalline phase P3HT is 4 Å, and the diameter of a C60 fullerene is ~7 Å [155], so 5 Å will be used as a distance for a likely intermediate separation. Note that the pi-stacking direction is the “good” direction for conductivity in P3HT films. The hexyl tail length, or “bad” conductivity direction of stacked P3HT is 17 Å, so we will use 20 Å as an upper limit for separation that will still allow the possibility of charge transfer between the two surfaces.

### 6.4.3. Keesom Force Calculation

At the laminated interface, the first dipole moment in the adhesion equations (Eqs. 6.2.2.2. & 6.2.2.3.) is that of the water molecule, but the second is dictated by the polarization of the other covalent bond participating in the hydrogen bond. In this work, that is either between the sulfur and carbon atoms of the thiophene ring. The polarity of a covalent bond is directly related to the difference in electronegativity of the two elements, the Pauling electronegativity scale [156] is used here to compare the relative polarity of the bonds in question with that of water.

| | **Hydrogen (2.20 eV)** | **Carbon (2.55 eV)** | **Sulfur (2.58 eV)** | **Oxygen (3.44 eV)** |
|---|---|---|---|---|
| **Hydrogen** | | 0.35 | 0.38 | 1.24 |
| **Carbon** | | | 0.03 | 0.89 |
| **Sulfur** | | | | 0.86 |

**Table 6.4.3.1.** The Pauling electronegativity of relevant elements showing the polar component of each bond studied here. Electronegativity of each element is shown in the column headings. Dipole strength is related to the difference in electronegativity between two covalently bonded atoms.

From table 6.4.3.1., we infer that a carbon-hydrogen bond in the hexyl tail of a P3HT monomer will have a permanent dipole. This dipole will be cancelled by one pointing in the opposite direction of the other side of the carbon chain. Sulfur is slightly more electronegative than carbon, but the difference is over an order of magnitude smaller than that between hydrogen and oxygen in water.

Hydrogen bonds in liquid water have a strength on the order of 1 kCal (4200 J)/Mol [157]. The hydrogen bond strength between water adsorbed onto a

solid and sulfur is likely weaker, but that will be discussed later. An upper limit on bond force can be estimated by the following calculation:

$$F_{\max} / Area = \frac{1}{2}\frac{W\sigma N_{Bond}}{DN_A} \qquad \text{(Eq. 6.4.3.1.)}$$

Equation 6.4.2.1 arises from altering the definition of work over sufficiently short distances ($W = F \cdot d$) to this system. $W$ is the energy of the bond (in J/Mol), and $\sigma$ is the surface density of bonding cites (in this case, the number of unit cells per area from Table 6.4.1.1). $N_{Bond}$ is the number of bonding sites per cell (1 for the *x*-*y* face). $D$ is the characteristic distance over which the bond acts. As a first order approximation, we assume that the distance over which the bond acts is equal to the initial separation of the atoms in the bond. $N_A$ is Avogadro's number.

The 1/2 factor in equation 6.4.3.1 comes from the 1:1 ratio of P3HT:Fullerene in the bulk heterojunction; ICBA is nonpolar. This is a simplistic approximation, as a P3HT:PCBM is known to have a thin skin layer of P3HT rich composition near the top of an air dried film. Upon annealing while in contact with PEDOT:PSS, it is likely that fullerene is attracted to the interface [49].

Using the minimum reasonable value of 2 Å for $D$, and upper limit on hydrogen bonding of $F_{max}$ (2 Å) = 1680 N/cm$^2$.

This upper limit assumes the following:

1. Delamination force is parallel to the displacement.
2. Force as a function of separation can be approximated as linear over a sufficiently short distance.
3. The strength and characteristic distance of the hydrogen bonds are the same in this system as they are for water.

Assumptions 1-2 should be either valid or good approximations. Assumption 3 is untrue due to the nature of the polar bonds available to participate in Keesom force bonding. First we consider number surface density of the bonds: If the *x*-*y* face is at the interface, one polar bond between the carbon and sulfur in the thiophene ring (0.03 eV difference) is available for hydrogen bonding. THe polarity of this bond is small compared to the 1.24 eV difference in electronegativity between the hydrogen and oxygen in water molecules. We will assume that the permanent dipole bonds at the lamination interface have 1/10 of the energy as hydrogen bonds between water molecules, due to the lower polarity of the bonds in P3HT. X-ray diffraction data suggests that in the bulk, face *y*-*z*, not face *x*-*z,* is predominantly facing the surface of the substrate [49, 152, 153], so it is not likely that the maximum number of bond sites is available at the interface. If crystal orientation were completely random, 1/3 of the faces (*x*-*y*) would have $N_{bond} = 1$, while the other two faces only show hydrocarbons or chain ends on their surface, so there are no polar bonds to participate in permanent dipole interactions. We average these values and

estimate an effective $N_{bond}$ = 1/3. $F_{max}$ also assumes that every available site on the P3HT interface will form a Keesom bond. This is not likely the case. Actual bond density will lower $F_{max}$, but by an unknown extent.

Since the adhesion surfaces are both solid, it is unlikely that the bonding surfaces will be as intimate as water molecules in liquid water. This increased separation would decrease both the surface energy of the bond, and increase the characteristic distance over which the bond strength is significant.

If we make the following corrections:

•Estimate Keesom bond energies as 1/10 of hydrogen bond energy in water

•Estimate $N_{bond}$ = 1/3

Then maximum force becomes a more likely estimated force ($F_{est}$).

This $F_{est}$ (2 Å)= 56 N/cm$^2$

If we increase the initial separation from 2 Å to 5 Å, and approximate that surface energy is inversely proportional to initial separation ($W \propto 1/D$), and increase $D$ from 2 Å to 5 Å: $F_{est}$ (5 Å)= 9 N/cm$^2$

Further increasing $D$ to 20 Å and decreasing, and decreasing $W$ by a factor of 5/20 gives a minimum force $F_{min}$ (20 Å) = 0.6 N/cm$^2$.

Surface energy can be calculated by combining the bond energy (4200 J/Mol for water, est. 420 J/Mol for water - thiophene sulfur) with the number density of atoms on the surface, approximated as 5X10$^{14}$/cm$^2$. For increased separation distance, we assume again that W is proportional to 1/$D$. Calculated surface energy for hydrogen bonds to water and Keesom bonds to thiophene sulfur are shown in table 6.4.3.2..

| *D* (Å) | *W(D)* if $H_20$ - $H_20$ ($mJ/m^2$) | *W(D) if* $H_20$ - S ($mJ/m^2$) |
|---|---|---|
| 2 | 35 | 3.5 |
| 5 | 12 | 1.2 |
| 20 | 3.5 | 0.35 |

**Table 6.4.3.2.** Estimated surface energy of hydrogen bonds between water molecules and permanent dipole bonds between water molecules and sulfur on the thiophene ring for different separation distances

A note on units: In this work, energies are given as $mJ/m^2$, while pressure is stated as force per area in $N/cm^2$. This is to ease the correlation of calculated values of force with measured values of delamination force on a 1 $cm^2$ substrate.

### 6.4.4. Debye and London Dispersion Force Calculation

While Keesom bonding is the strongest available force for adhesion, it is not the only one. Induced dipole-induced dipole and dipole-induced dipole Van der Waals forces are also available to hold the interface together. The equation governing the surface energy per area due to the remaining van der Waals interaction for 2 planes is given by [158]:

$W = -A/12\pi D^2$ Per unit area (Eq. 6.4.4.1.)

Where *D* is the separation between the planes, and *A* is the Hamaker constant in units of Joules:

$A = \pi^2 C \rho_1 \rho_2$ (Eq. 6.4.4.2.)

Where $\rho$ is the number density of each material per volume, and $C$ is the dispersion constant for the pair (in $J/m^6$). The Hamaker constant for hydrocarbons is $5x10^{-20}$ J and for water is $1.5x10^{-19}$ J [158]. Typical values for the Hamaker constants of condensed phases, whether solid or liquid, are about $10^{-19}$ J. This arises because the coefficient $C$ in the interatomic pair potential is roughly proportional to the square of the polarizabilty , which is in turn roughly proportional to the volume of an atom. Larger atoms are more polarizable, but less densely packed. This does not apply strictly to the P3HT system because the packing of the hexyl tails is limited in part by the conjugated backbone of the molecule. Similarly, the availability of carbon atoms at the surface of a fullerene crystal is limited by the packing of the fullerene molecules. This should decrease the value of $A$ by an order of magnitude or less. If we choose $A = 5x10^{-21}$J, we get the following range of values for $W$ and $F = dW/dD$ :

| D (Å) | W/A ($mJ/m^2$) | F/A ($N/cm^2$) |
|---|---|---|
| 2 | 3.29 | 3320 |
| 5 | 0.53 | 212 |
| 10 | 0.13 | 26.5 |
| 20 | 0.033 | 3.31 |

**Table 6.4.4.1.** Representative surface energies and forces of induced van der Waals interactions at various separation distances.

Changing the separation by a factor of 10 changes the calculated Van der Waals force by 3 orders of magnitude. Although it is not plausible to know the average separation between the atoms in the laminated film, a safe estimate

would be between 2 Å and 10 Å. The 10 Å data point is included because it compares well to measured values.

### 6.5. Adhesion Force from Surface Tension and Contact Angles

One way to estimate surface (bond) energy between a solid and a liquid is to use contact angle measurement. This does not give any information to the molecular origin of the force, but it is on additional way to estimate the force between the 2 interfaces.

In contact angle measurement, a liquid is dropped onto a solid substrate, and the angle where the droplet contacts the surface is measured. The Young-Dupré equation relates the surface tension of the liquid ($\gamma$), the contact angle ($\theta$), and the adhesion energy per area ($\Delta W$).

$$\Delta W_{sl} = \gamma_l(1 + \cos\theta_{sl}) \qquad \text{(Eq. 6.5.1)}$$

For this study, DI water, and a 10% sorbitol solution were dropped onto a P3HT:ICBA (1:1) substrate and contact angles were measured. The surface tension of water at 25 ˚C is 72 mJ/Mol [159]. Adding sucrose or glucose to water increases its surface tension by less than 5% [160]. We assume that d-sorbitol increases the surface tension of water to the same extent as sucrose or glucose.

DI water on the BHJ gives an angle of 106˚. The contact angle of 10 % d-sorbitol in water on BHJ is 102˚. Given the increase in surface tension with the

addition of the d-sorbitol, the contact angle should increase with the addition of the d-sorbitol if the surface energy were unchanged. The decrease in contact angle along with the increased surface tension shows an increase in surface energy from 52.2 to 57.4 mJ/m$^2$. This is very large compared to previously calculated values and measured values. The number of bonding sites for d-sorbitol with adsorbed water will be greatly reduced compared to that of pure liquid water, but a surface density calculation for d-sorbitol films is beyond the scope of this work.

### 6.6. Conclusions

Delamination force is not significantly dependent on the presence of d-sorbitol. This contrasts with our experience that devices without d-sorbitol at the adhesion interface are much more likely to delaminate during fabrication. Delamination in this case occurs when the plates of the hot press are pulled apart. This delamination can be avoided with the use of a PFTE release film. Without d-sorbitol, another problem arises in that there is no initial adhesion or “tackiness” of the two substrates. The top flexible substrate is free to slide around over the bottom one, and improper alignment makes the device inoperable. For this work, complete devices were not necessary, so alignment was not important. The point remains that devices with d-sorbitol at the lamination interface are more physically robust at the time of fabrication than those without, while after fabrication, there is no apparent difference between the two. We conclude that the mechanism of initial “thumb pressure” adhesion is not

the same as the final cooled pressed device. The difference between the two may involve the heat during the 130 ˚C lamination changing the properties of the PEDOT or BHJ films, or moisture in the PEDOT:PSS film that is driven off during this step. There may also be something about the d-sorbitol that helps initial adhesion because it acts weakly, but over a larger distance than the final device, which may have closer separation distances after the 250 pounds (1100 N) of force are applied during the lamination.

Three different types of van der Waals adhesion mechanisms are proposed, permanent dipole - permanent dipole Keesom force bonding, and the remaining combined van der Waals (Debye and London dispersion) forces. Order of magnitude estimates have been found that depend heavily on the separation distance of the 2 laminated surfaces, and orientation of P3HT in the BHJ. Explanations of dipole bonding tend to be thermodynamic in nature, so relating individual molecular bonds to macroscopic forces has proven difficult. Debye and London dispersion van der Waals force calculations were estimated, and are less dependent on the molecular structure at the interface. Although Debye and London dispersion forces tend to be inherently weaker than polar bonding Keesom forces, they apply to a greater number of constituents in the system, so they end up being significant, and likely dominant when compared to Keesom force bonding. Possible mechanisms not explored are those that involve time evolution at the laminated interface. It is known that PEDOT:PSS and d-sorbitol both absorb ambient water, which affects device performance. This may also drive chemistry that affects adhesion at the interface.

Permanent dipole bonding estimates range from 1680 - 0.6 N/cm$^2$ for the system of planar PEDOT:PSS:d-sorbitol bonding to a P3HT:fullerene BHJ. Van der Waals force estimates range from 3300 - 3 N/cm$^2$. The delamination force is measured as ~20 N, which is well within the range of values for either bonding mechanism, especially when defect propagation is considered.

Water contact angle measurements give a surface energy of ~55 mJ/m$^2$, which is higher than even the upper limit estimates for either hydrogen or van der Waal interaction energies. We expect this number to be high, since interaction distances will likely be at a minimum with a liquid over the BHJ, but given that it is higher than either estimate, we also infer that both hydrogen and van der Waals forces contribute to the sum of adhesion forces measured with contact angles.

Overall, we were able to get a consistent value of the force required for delamination between PEDOT:PSS and BHJ. This value is within the range of order of magnitude estimates for both hydrogen bonding and van der Waals bonding mechanisms. Contact angle measurements confirm that the actual surface energy between the two materials is likely a result of the combination of both mechanisms. Because of the liquid nature of the contact angle measurement, we are able to assume a separation distance of about 2 Å for liquid water over the BHJ. When the two solid surfaces are laminated, we estimate a separation between 2 Å and 10 Å based on the features of the molecules at the lamination interface, and comparison of calculated adhesion force vales to measured delamination forces.

**Bibliography**


1. Kearns, D. and M. Calvin, *Photovoltaic Effect and Photoconductivity in Laminated Organic Systems.* J. Chem. Phys. , 1958. **29**: p. 950-951.
2. Tang, C.W., *Two-layer organic photovoltaic cell.* Applied Physics Letterrs, 1986. **48**(2): p. 183-185.
3. Brabec, C., V. Dyakonov, and U. Scherf, *Organic Photovoltaics*. 2008: Wiley-VCH.
4. Brabec, C.J., et al., *Polymer-Fullerene Bulk-Heterojunction Solar Cells.* Adv. Mater., 2010. **22**(34): p. 3839-3856.
5. Shaheen, S.E., D.S. Ginley, and a.E. Jabbour, *Organic-Based Photovoltaics: Toward Low-Cost Power Generation.* MRS BULLETIN, 2005. **30**: p. 10-19.
6. Dennler, G., et al., *Flexible, conjugated polymer-fullerene-based bulk-heterojunction solar cells: Basics, encapsulation, and integration.* J. Mater. Res., 2005. **20**(12): p. 3224-3233.
7. Li, G., R. Zhu, and Y. Yang, *Polymer solar cells.* Nature Photon, 2012. **6**(3): p. 153-161.
8. Peumans, P. and S.U.S.R. Forrest, *Efficient bulk heterojunction photovoltaic cells using small- molecular-weight organic thin films.* NATURE, 2003. **425**: p. 158-162.
9. Peumans, P. and S.R. Forrest, *Very-high-efficiency double-heterostructure copper phthalocyanine/C60 photovoltaic cells.* Appl. Phys. Lett. , 2001. **79**(1): p. 126-128.
10. Peumans, P., V. Bulovic, and S.R. Forrest, *Efficient photon harvesting at high optical intensities in ultrathin organic double-heterostructure photovoltaic diodes.* Appl. Phys. Lett. , 2000. **76**(19): p. 2650-2652.
11. Meiss, J., et al., *Highly efficient semitransparent tandem organic solar cells with complementary absorber materials.* Appl. Phys. Lett., 2011. **99**(4): p. 043301.
12. Pfuetzner, S., et al., *Improved bulk heterojunction organic solar cells employing C[sub 70] fullerenes.* Appl. Phys. Lett., 2009. **94**(22): p. 223307.
13. Kopidakis, N., et al., *Bulk heterojunction organic photovoltaic devices based on phenyl-cored thiophene dendrimers.* Appl. Phys. Lett., 2006. **89**: p. 103524.
14. Matsuo, Y., et al., *Columnar structure in bulk heterojunction in solution-processable three-layered pin organic photovoltaic devices using tetrabenzoporphyrin precursor and silylmethyl [ ….* J. AM. CHEM. SOC., 2009. **131**: p. 16048-16050.
15. Sun, Y., *Solution-processed small-molecule solar cells with 6.7% efficiency.* Nature Materials, 2011. **11**(1): p. 44-48.
16. Wolden, C., et al., *Photovoltaic Manufacturing: Present status, future prospects, and research needs.* Journal of Vacuum Science and Technology A, 2011. **29**: p. 1-17.

17. Krebs, F.C., *All solution roll-to-roll processed polymer solar cells free from indium-tin-oxide and vacuum coating steps.* Organic Electronics, 2009. **10**(5): p. 761-768.
18. Chen, C.-C., et al., *Visibly Transparent Polymer Solar Cells Produced by Solution Processing.* ACSNano, 2012.
19. Steim, R., et al., *Organic photovoltaics for low light applications.* Solar Energy Materials and Solar Cells, 2011. **95**(12): p. 3256-3261.
20. Heliatek. *10%*. Available from: http://www.heliatek.com/newscenter/latest_news/heliatek-erzielt-mit-107-effizienz-neuen-weltrekord-fur-seine-organische-tandemzelle/?lang=en.
21. Dou, L., et al., *Tandem polymer solar cells featuring a spectrally matched low-bandgap polymer.* Nature Photon, 2012. **6**(3): p. 180-185.
22. Polyera. *9.1% Record*. Available from: http://www.polyera.com/newsflash/polyera-achieves-world-record-organic-solar-cell-performance.
23. Lloyd, M.T. and D.C. Olson, *Influence of the hole-transport layer on the initial behavior and lifetime of inverted organic photovoltaics.* 2011: p. 1-8.
24. Lin, S.-H., et al., *Synthesis of ultraviolet curable encapsulating adhesives and their package applications for organic optoelectronic devices.* Solid State Sciences, 2011. **13**(10): p. 1889-1895.
25. Barnes, T.M., et al., *Comparing the Fundamental Physics and Device Performance of Transparent, Conductive Nanostructured Networks with Conventional Transparent Conducting Oxides.* Adv. Energy Mater., 2012. **2**(3): p. 353-360.
26. Granqvist, C.G., *Transparent conductors as solar energy materials: a panoramic review.* Solar Energy Materials & Solar Cells, 2007. **91**: p. 1529-1598.
27. Spectra, A.S.f.T.a.M.T.R.
28. Gregg, B., S. Chen, and R. Cormier, *Coulomb forces and doping in organic semiconductors.* Chem Mater, 2004. **16**(23): p. 4586-4599.
29. Forrest, S.R., *The path to ubiquitous and low-cost organic electronic appliances on plastic.* Nature, 2004.
30. Baroni, S. and R. Resta, *Ab initio calculation of the macroscopic dielectric constant in silicon.* Physical Review B, 1986. **33**(10): p. 7017-1721.
31. Clarke, T.M. and J.R. Durrant, *Charge Photogeneration in Organic Solar Cells.* Chemical Review, 2010. **110**(11): p. 6736-6767.
32. Koster, L.J.A., S.E. Shaheen, and J.C. Hummelen, *Pathways to a New Efficiency Regime for Organic Solar Cells.* Adv. Energy Mater., 2012: p. n/a-n/a.
33. Faist, M.A., et al., *Competition between the Charge Transfer State and the Singlet States of Donor or Acceptor Limiting the Efficiency in Polymer: Fullerene Solar Cells.* Journal of the American Chemical Society, 2012. **134**: p. 685-693.
34. Huang, Y.-S., et al., *Electronic structures of interfacial states formed at polymeric semiconductor heterojunctions.* Nature Materials, 2008. **7**(6): p. 483-489.

35. Van Eersel, H., R.A.J. Janssen, and M. Kemerink, *Mechanism for Efficient Photoinduced Charge Separation at Disordered Organic Heterointerfaces.* Adv. Funct. Mater., 2012. **22**(13): p. 2700-2708.
36. Kohler, A., et al., *Charge Separation in Localized and Delocalized Electronic States in Polymeric Semiconductors.* Nat Lett., 1998. **392**: p. 903-906.
37. Schwenn, P.E., et al., *A Small Molecule Non-fullerene Electron Acceptor for Organic Solar Cells.* Adv. Energy Mater., 2010. **1**(1): p. 73-81.
38. Schubert, M., et al., *Influence of Aggregation on the Performance of All-Polymer Solar Cells Containing Low-Bandgap Naphthalenediimide Copolymers.* Adv. Energy Mater., 2012. **2**(3): p. 369-380.
39. Facchetti, A., *SPIE Talk*, in *SPIE*2012: San Diego.
40. Polyera. *5.2% All Polymer*. 2012; Available from: http://www.polyera.com/newsflash/polyera-achieves-5-2-all-polymer-organic-solar-cells.
41. Coffey, D.C., et al., *An Optimal Driving Force for Converting Excitons into Free Carriers in Excitonic Solar Cells.* J. Phys. Chem. C, 2012. **116**: p. 8916-8923.
42. He, Y., et al., *Indene– C60 Bisadduct: A New Acceptor for High-Performance Polymer Solar Cells.* J. AM. CHEM. SOC., 2010.
43. Erb, T., et al., *Correlation Between Structural and Optical Properties of Composite Polymer/Fullerene Films for Organic Solar Cells.* Adv. Funct. Mater., 2005. **15**(7): p. 1193-1196.
44. Kroeze, J.E., et al., *Contactless Determination of the Photoconductivity Action Spectrum, Exciton Diffusion*
*Length, and Charge Separation Efficiency in Polythiophene-Sensitized TiO2 Bilayers.* J. Phys. Chem. B, 2003. **107**: p. 7696-7705.
45. Luer, L., et al., *Oxygen-induced quenching of photoexcited states in polythiophene films.* Organic Electronics, 2004. **5**: p. 83-89.
46. Goh, C., S.R. Scully, and M.D. McGehee, *Effects of molecular interface modification in hybrid organic-inorganic photovoltaic cells.* J. Appl. Phys. , 2007. **101**: p. 1-13.
47. Shaw, P.E., A. Ruseckas, and I.D.W. Samuel, *Exciton Diffusion Measurements in Poly(3-hexylthiophene).* Adv. Mater., 2008. **20**(18): p. 3516-3520.
48. Yu, G., et al., *Polymer Photovoltaic Cells: Enhanced Efficiencies via a Network of Internal Donor-Acceptor Heterojunctions.* Science, 1995. **270**(5243): p. 1789-1791.
49. Delongchamp, D.M., R.J. Kline, and A. Herzing, *Nanoscale structure measurements for polymer-fullerene photovoltaics.* Energy Environ. Sci., 2012. **5**(3): p. 5980.
50. Guilbert, A.A.Y., et al., *Effect of Multiple Adduct Fullerenes on Microstructure and Phase Behavior of P3HT:Fullerene Blend Films for Organic Solar Cells.* ACS Nano, 2012. **6**(5): p. 3868.
51. Gao, Y., et al., *Understanding Morphology-Dependent Polymer Aggregation Properties and Photocurrent*

*Generation in Polythiophene/Fullerene Solar Cells of Variable Compositions.* J. Phys. Chem. C, 2010. **114**: p. 1521-1528.
52. Nardes, A.M., et al., *Photoinduced Charge Carrier Generation and Decay in Sequentially Deposited Polymer/Fullerene Layers: Bulk Heterojunction vs Planar Interface.* J Phys Chem C, 2012.
53. White, M.S., *Effects of charge carrier concentration in hybrid conjugated polymer/oxide photovoltaic devices*, in *CU Boulder Physics Dept.*2009, University of Colorado. p. 1-166.
54. Brabec, C.J., et al., *Origin of the Open Circuit Voltage of Plastic Solar Cells.* Adv. Funct. Mater. , 2002. **11**(5): p. 374-380.
55. Lloyd, M.T., et al., *Impact of contact evolution on the shelf life of organic solar cells.* J. Mater. Chem., 2009. **19**(41): p. 7638.
56. Reese, M.O., et al., *Optimal negative electrodes for poly(3-hexylthiophene): [6,6]-phenyl C61-butyric acid methyl ester bulk heterojunction photovoltaic devices.* Applied Physics Letters, 2008. **92**(5): p. 053307.
57. Cheun, H., et al., *Oriented Growth of Al2O3:ZnO Nanolaminates for Use as Electron-Selective Electrodes in Inverted Polymer Solar Cells.* Adv. Funct. Mater., 2012. **22**(7): p. 1531-1538.
58. Ratcliff, E.L., B. Zacher, and N.R. Armstrong, *Selective Interlayers and Contacts in Organic Photovoltaic Cells.* J Phys Chem Lett, 2011. **2**: p. 1337-1350.
59. Steim, R., F.R. Kogler, and C. Brabec, *Interface Materials for Organic Solar Cells.* J Mater Chem, 2010. **20**: p. 2499-2512.
60. Zhou, Y., et al., *A Universal Method to Produce Low-Work Function Electrodes for Organic Electronics.* Science, 2012. **336**(6079): p. 327-332.
61. Berry, J., et al., *Surface Treatment of NiO Hole Transport Layers for Organic Solar Cells.* Selected Topics in Quantum Electronics, IEEE Journal of, 2010. **16**(6): p. 1649 - 1655.
62. Liu, F., et al., *Efficient polymer photovoltaic cells using solution-processed MoO3 as anode buffer layer.* Solar Energy Materials and Solar Cells, 2010. **94**(5): p. 842-845.
63. Fang, G., et al., *Enhanced Performance for Polymer Solar Cells by Using Surfactant-Modified PEDOT:PSS as the Anode Buffer Layer.* Macromol. Chem. Phys., 2011: p. n/a-n/a.
64. Liao, H.-H., et al., *Highly efficient inverted polymer solar cell by low temperature annealing of Cs2CO3 interlayer.* Appl. Phys. Lett., 2008. **92**(17): p. 173303.
65. Im, H., et al., *Highly efficient organic light-emitting diodes fabricated utilizing nickel-oxide buffer layers between the anodes and the hole transport layers.* Thin Solid Films, 2007. **515**(12): p. 5099-5102.
66. Qian, L., et al., *Hybrid polymer-CdSe solar cells with a ZnO nanoparticle buffer layer for improved efficiency and lifetime.* J. Mater. Chem., 2011. **21**(11): p. 3814.

67. Han, S., et al., *Improving performance of organic solar cells using amorphous tungsten oxides as an interfacial buffer layer on transparent anodes.* Organic Electronics, 2009. **10**(5): p. 791-797.
68. Zhang, F., et al., *Influence of buffer layers on the performance of polymer solar cells.* Appl. Phys. Lett., 2004. **84**(19): p. 3906-3908.
69. Steirer, K.X., et al., *Ultrasonically sprayed and inkjet printed thin film electrodes for organic solar cells.* Thin Solid Films, 2009. **517**(8): p. 2781-2786.
70. Lim, Y.-F., et al., *Spray-deposited poly(3,4-ethylenedioxythiophene):poly(styrenesulfonate) top electrode for organic solar cells.* Appl. Phys. Lett., 2008. **93**(19): p. 193301.
71. Ely, F., et al., *Patterning quality control of inkjet printed PEDOT:PSS films by wetting properties.* Synthetic Metals, 2011. **161**(19-20): p. 2129-2134.
72. Wilson, P., C. Lekakou, and J.F. Watts, *A comparative assessment of surface microstructure and electrical conductivity dependence on co-solvent addition in spin coated and inkjet printed poly(3,4-ethylenedioxythiophene):polystyrene sulphonate (PEDOT:PSS).* Organic Electronics, 2012. **13**(3): p. 409-418.
73. Srichan, C., et al., *Inkjet Printing PEDOT:PSS using Desktop Inkjet Printer.* Electrical Engineering/Electronics, Computer, Telecommunications and Information Technology, 2009. ECTI-CON 2009. 6th International Conference on, 2009. **1**: p. 465-468.
74. Steirer, K.X., et al., *Enhanced Efficiency in Plastic Solar Cells via Energy Matched Solution Processed NiOx Interlayers.* Adv. Energy Mater., 2011. **1**(5): p. 813-820.
75. Lloyd, M.T., et al., *Influence of the hole-transport layer on the initial behavior and lifetime of inverted organic photovoltaics.* Solar Energy Materials and Solar Cells, 2011. **95**(5): p. 1382-1388.
76. Jeuris, K., et al., *Light stability of 3, 4-ethylenedioxythiophene-based derivatives.* Synthetic Metals, 2003. **132**: p. 289-295.
77. Duren, J.K.J.v., et al., *In-Situ Compositional and Structural Analysis of Plastic Solar Cells.* Adv. Funct. Mater., 2002. **12**(10): p. 665-669.
78. Jong, M.P.d., L.J.v. IJzendoorn, and M.J.A.d. Voigt, *Stability of the interface between indium-tin-oxide and poly (3, 4-ethylenedioxythiophene)/poly (styrenesulfonate) in polymer light-emitting diodes.* Appl. Phys. Lett., 2000. **77**(14): p. 2255-2257.
79. Voigt, M.M., et al., *Gravure printing inverted organic solar cells The influence of ink properties on film quality and device performance.* Solar Energy Materials and Solar Cells, 2012. **105**(C): p. 77-85.
80. Greiner, M.T., *Universal energy-level alignment of molecules on metal oxides.* Nature Materials, 2011. **11**(1): p. 76-81.
81. Hammond, S.R., et al., *Low-temperature, solution-processed molybdenum oxide hole-collection layer for organic photovoltaics.* J. Mater. Chem., 2012. **22**(7): p. 3249-3254.

82. Kouijzer, S., et al., *Efficient Inverted Tandem Polymer Solar Cells with a Solution-Processed Recombination Layer.* Adv. Energy Mater., 2012: p. n/a-n/a.
83. Waldauf, C., et al., *Highly efficient inverted organic photovoltaics using solution based titanium oxide as electron selective contact.* Appl. Phys. Lett., 2006. **89**(23): p. 233517.
84. White, M., D. Olson, and S. Shaheen, *Inverted bulk-heterojunction organic photovoltaic device using a solution-derived ZnO ….* Appl. Phys. Lett., 2006.
85. Zaumseil, J., K. Baldwin, and J. Rogers, *Contact resistance in organic transistors that use source and drain electrodes formed by soft contact lamination.* J. Appl. Phys., 2003. **93**(10): p. 6117-6124.
86. Girotto, C., et al., *Nanoparticle-based, spray-coated silver top contacts for efficient polymer solar cells.* Organic Electronics, 2009. **10**(4): p. 735-740.
87. Shockley, W. and H.J. Queisser, *Detailed balance limit of efficiency of p-n junction solar cells.* J. Appl. Phys., 1961. **32**(3): p. 510-519.
88. Ameri, T., et al., *Organic tandem solar cells: A review.* Energy Environ. Sci., 2009. **2**(4): p. 347.
89. Gilot, J., M.M. Wienk, and R.A.J. Janssen, *Measuring the current density - Voltage characteristics of individual subcells in two-terminal polymer tandem solar cells.* ORGANIC ELECTRONICS, 2011: p. 1-6.
90. Gilot, J., M.M. Wienk, and R.A.J. Janssen, *Measuring the External Quantum Efficiency of Two-Terminal Polymer Tandem Solar Cells.* Adv. Funct. Mater., 2010. **20**(22): p. 3904-3911.
91. Park, S., et al., *Bulk heterojunction solar cells with internal quantum efficiency approaching 100&percnt.* Nat Photonics, 2009. **3**(5): p. 297-302.
92. Nam, Y.M., J. Huh, and W.H. Jo, *A computational study on optimal design for organic tandem solar cells.* Solar Energy Materials and Solar Cells, 2011. **95**(4): p. 1095-1101.
93. Hoppe, H., et al., *Modeling the optical absorption within conjugated polymer/fullerene-based bulk-heterojunction organic solar cells.* Solar Energy Materials & Solar Cells, 2003. **80**: p. 105-113.
94. Chou, C.-H., et al., *A Metal-Oxide Interconnection Layer for Polymer Tandem Solar Cells with an Inverted Architecture.* Adv. Mater., 2010. **23**(10): p. 1282-1286.
95. Yang, J., et al., *A Robust Inter-Connecting Layer for Achieving High Performance Tandem Polymer Solar Cells.* Adv. Mater., 2011: p. n/a-n/a.
96. Sista, S., et al., *Highly Efficient Tandem Polymer Photovoltaic Cells.* Adv. Mater., 2010. **22**(3): p. 380-383.
97. Kim, J., et al., *Efficient tandem polymer solar cells fabricated by all-solution processing.* Science, 2007. **317**(5835): p. 222.
98. Centurioni, E., *Generalized matrix method for calculation of internal light energy flux in mixed coherent and incoherent multilayers.* Appl Optics, 2005. **44**(35): p. 7532-7539.

99. Pettersson, L.A.A., a.L.S. Roman, and O.I. s, *Modeling photocurrent action spectra of photovoltaic devices based on organic films.* JOURNAL OF APPLIED PHYSICS, 2009. **86**(1): p. 487-495.
100. Knittl, Z., *Optics of Thin Films (An Optical Multilayer Theory)*. 1976: John WIley & Sons.
101. Jorgensen, M., K. Norrman, and F.C. Krebs, *Stability/degradation of polymer solar cells.* Solar Energy Materials and Solar Cells, 2008. **92**(7): p. 686-714.
102. Granström, M., et al., *Laminated fabrication of polymeric photovoltaic diodes.* Nature, 1998. **395**(6699): p. 257-260.
103. Nakamura, M., et al., *High-performance polymer photovoltaic devices with inverted structure prepared by thermal lamination.* Solar Energy Materials and Solar Cells, 2009. **93**(9): p. 1681-1684.
104. Huang, J., G. Li, and Y. Yang, *A Semi-transparent Plastic Solar Cell Fabricated by a Lamination Process.* Adv. Mater., 2008. **20**(3): p. 415-419.
105. Hau, S.K., et al., *Air-stable inverted flexible polymer solar cells using zinc oxide nanoparticles as an electron selective layer.* Appl. Phys. Lett., 2008. **92**(25): p. 253301.
106. Yao, Y., et al., *Effects of Solvent Mixtures on the Nanoscale Phase Separation in Polymer Solar Cells.* Adv. Funct. Mater., 2008. **18**(12): p. 1783-1789.
107. Lee, J., et al., *Processing additives for improved efficiency from bulk heterojunction solar cells.* J. Am. Chem. Soc, 2008. **130**(11): p. 3619-3623.
108. Ouyang, J. and Y. Yang, *Conducting Polymer as Transparent Electric Glue.* Adv. Mater., 2006. **18**(16): p. 2141-2144.
109. Cravino, A., P. Schilinsky, and C.J. Brabec, *Characterization of organic solar cells: the importance of device layout.* Adv. Funct. Mater., 2007. **17**(18): p. 3906-3910.
110. Kim, M.-S., et al., *Choice of electrode geometry for accurate measurement of organic photovoltaic cell performance.* Appl. Phys. Lett., 2008. **92**(13): p. 133301.
111. Nardes, A., et al., *Conductivity, work function, and environmental stability of PEDOT:PSS thin films treated with sorbitol.* Organic Electronics, 2008. **9**(5): p. 727-734.
112. Ratcliff, E.L., B. Zacher, and N.R. Armstrong, *Selective Interlayers and Contacts in Organic Photovoltaic Cells.* J. Phys. Chem. Lett., 2011. **2**(11): p. 1337-1350.
113. Feltrin, A. and A. Freundlich, *Material considerations for terawatt level deployment of photovoltaics.* Renewable Energy, 2008. **33**: p. 180-185.
114. Xu, Z.-Q., et al., *Efficient inverted polymer solar cells incorporating doped organic electron transporting layer.* ORGANIC ELECTRONICS, 2012. **13**(4): p. 697-704.

115. Wang, J.-C., et al., *Highly efficient flexible inverted organic solar cells using atomic layer deposited ZnO as electron selective layer.* J. Mater. Chem., 2010. **20**(5): p. 862.
116. Bailey, B.A., et al., *Air-processed organic photovoltaic devices fabricated with hot press lamination.* ORGANIC ELECTRONICS, 2011. **12**(1): p. 108-112.
117. Nickel, F., et al., *Cathodes comprising highly conductive poly(3,4-ethylenedioxythiophene):poly(styrenesulfonate) for semi-transparent polymer solar cells.* Organic Electronics, 2010. **11**(4): p. 535-538.
118. Zhou, Y., et al., *Inverted and transparent polymer solar cells prepared with vacuum-free processing.* Solar Energy Materials and Solar Cells, 2009. **93**(4): p. 497-500.
119. Zhou, Y., et al., *Optimization of a polymer top electrode for inverted semitransparent organic solar cells.* Organic Electronics, 2011. **12**(5): p. 827-831.
120. Barnes, T.M., et al., *Carbon nanotube network electrodes enabling efficient organic solar cells without a hole transport layer.* Appl. Phys. Lett., 2010. **96**(24): p. 243309.
121. Blackburn, J.L., et al., *Transparent conductive single-walled carbon nanotube networks with precisely tunable ratios of semiconducting and metallic nanotubes.* Acs Nano, 2008. **2**(6): p. 1266-1274.
122. Tenent, R.C., et al., *Ultrasmooth, Large-Area, High-Uniformity, Conductive Transparent Single-Walled-Carbon-Nanotube Films for Photovoltaics Produced by Ultrasonic Spraying.* Adv. Mater., 2009. **21**(31): p. 3210-3216.
123. Rowell, M.W., et al., *Organic solar cells with carbon nanotube network electrodes.* Applied Physics Letters, 2006. **88**(23): p. 233506.
124. Zhou, Y., L. Hu, and G. Gruner, *A method of printing carbon nanotube thin films.* Applied Physics Letters, 2006. **88**(12): p. 123109.
125. Zou, J., et al., *Metal grid/conducting polymer hybrid transparent electrode for inverted polymer solar cells.* Appl. Phys. Lett., 2010. **96**(20): p. 203301.
126. Olson, D.C., et al., *Hybrid photovoltaic devices of polymer and ZnO nanofiber composites.* Thin Solid Films, 2006. **496**(1): p. 26-29.
127. Barnes, T.M., et al., *Reversibility, Dopant Desorption, and Tunneling in the Temperature-Dependent Conductivity of Type-Separated, Conductive Carbon Nanotube Networks.* Acs Nano, 2008. **2**(9): p. 1968-1976.
128. Chandra, B., et al., *Stable Charge-Transfer Doping of Transparent Single-Walled Carbon Nanotube Films.* Chem. Mater., 2010. **22**(18): p. 5179-5183.
129. Gaynor, W., J.-Y. Lee, and P. Peumans, *Fully Solution-Processed Inverted Polymer Solar Cells with Laminated Nanowire Electrodes.* Acs Nano, 2010. **4**(1): p. 30-34.
130. Albrecht, S., et al., *Light management in PCPDTBT:PC70BM solar cells: A comparison of standard and inverted device structures.* ORGANIC ELECTRONICS, 2012. **13**(4): p. 615-622.

131. Groep, J.v.d., P. Spinelli, and A. Polman, *Transparent Conducting Silver Nanowire Networks.* Nano Lett., 2012. **12**: p. 3138-3144.
132. Shrotriya, V., et al., *Transition metal oxides as the buffer layer for polymer photovoltaic cells.* Applied Physics Letters, 2006. **88**(7): p. 073508.
133. Tao, C., et al., *Role of tungsten oxide in inverted polymer solar cells.* Appl. Phys. Lett., 2009. **94**(4): p. 043311.
134. Zilberberg, K., et al., *Solution Processed Vanadium Pentoxide as Charge Extraction Layer for Organic Solar Cells.* Adv. Energy Mater., 2011. **1**(3): p. 377-381.
135. White, M.S., *Effects of charge carrier concentration in hybrid conjugated polymer/oxide photovoltaic devices*, in *Physics*2009, University of Colorado. p. 1-166.
136. Guan, Z.-L., et al., *Direct determination of the electronic structure of the poly(3-hexylthiophene):phenyl-[6,6]-C61 butyric acid methyl ester blend.* Organic Electronics, 2010. **11**(11): p. 1779-1785.
137. Olson, D.C., et al., *Band-offset engineering for enhanced open-circuit voltage in polymer-oxide hybrid solar cells.* Adv. Funct. Mater., 2007. **17**(2): p. 264-269.
138. Beek, W.J.E., et al., *Hybrid Solar Cells Using a Zinc Oxide Precursor and a Conjugated Polymer.* Adv. Funct. Mater., 2005. **15**(10): p. 1703-1707.
139. Bauer, A., et al., *ZnO:Al-based recombination layers for polymer tandem solar cells: Influence of acidic or pH-neutral poly(3,4-ethylenedioxythiophene):poly(styrenesulfonate) formulations.* ORGANIC ELECTRONICS, 2011: p. 1-5.
140. Gevaerts, V.S., et al., *Solution Processed Polymer Tandem Solar Cell Using Efficient Small and Wide bandgap Polymer:Fullerene Blends.* Adv. Mater., 2012: p. n/a-n/a.
141. Gilot, J., M.M. Wienk, and R.A.J. Janssen, *Optimizing Polymer Tandem Solar Cells.* Adv. Mater., 2010. **22**(8): p. E67-E71.
142. Plextronics. *www.plextronics.com*. Available from: www.plextronics.com.
143. Aldrich, S. *Sigma Aldrich*. Available from: http://www.sigmaaldrich.com.
144. Beek, W., et al., *Hybrid zinc oxide conjugated polymer bulk heterojunction solar cells.* J Phys Chem B, 2005. **109**(19): p. 9505-9516.
145. Janotti, A. and C.G. Van de Walle, *Native Point Defects in ZnO.* Phys. Rev. B, 2007. **76**(162502): p. 162502-1 - 162502-22.
146. Hau, S.K., et al., *High performance ambient processed inverted polymer solar cells through interfacial modification with a fullerene self-assembled monolayer.* Appl. Phys. Lett., 2008. **93**(23): p. 233304.
147. Jen, A.K.-Y., *Self-assembled monolayer modified ZnO/metal bilayer cathodes*

*for polymer/fullerene bulk-heterojunction solar cells* 2008: p. 1-3.
148. Brand, V., C. Bruner, and R.H. Dauskardt, *Cohesion and device reliability in organic bulk heterojunction photovoltaic cells.* Solar Energy Materials and Solar Cells, 2012. **99**(C): p. 182-189.

149. Kittel, C., *Introduction to Solid State Physics, 8th ed.* 8 ed. 2005: John Wiley & Sons, Inc.
150. Braun, S., W.R. Salaneck, and M. Fahlman, *Energy-Level Alignment at Organic/Metal and Organic/Organic Interfaces.* Adv. Mater., 2009. **21**(14-15): p. 1450-1472.
151. Hadziioannou, G. and G.G. Malliaras, *Semiconducting Polymers, Vol. 1*. 2007.
152. Xie, W., et al., *Structure and sources of disorder in poly(3-hexylthiophene) crystals investigated by density functional calculations with van der Waals interactions.* Phys. Rev. B, 2011. **83**(18): p. 184117.
153. Ma, W., et al., *Thermally Stable, Efficient Polymer Solar Cells with Nanoscale Control of the Interpenetrating Network Morphology.* Adv. Funct. Mater., 2005. **15**(10): p. 1617-1622.
154. Modig, K., B. Pfrommer, and B. Halle, *Temperature-Dependent Hydrogen-Bond Geometry in Liquid Water.* Phys. Rev. Lett., 2003. **90**(7): p. 075502.
155. Melnichenko, Y.B., et al., *Characterization of fullerenes and fullerene derivatives by small-angle neutron scattering and transmission measurements.* J. Chem. Phys. , 1999. **111**(10): p. 4724.
156. Lide, D.R., *Handbook of Chemistry and Physics, 84th ed.* 2003: CRC Press, Boca Raton, FL.
157. Smith, J.D., *Energetics of Hydrogen Bond Network Rearrangements in Liquid Water.* Science, 2004. **306**(5697): p. 851-853.
158. Israelachvili, J., *Intermolecular & Surface Forces, 2nd. Ed.* 2 ed. 1992: Academic Press, Inc.
159. Dean, J.A., *Lange's Handbook of Chemistry, 11th ed.* 1967: New York : McGraw-Hill.
160. Docoslis, A., R.F. Giese, and C.J. van Oss, *Influence of the water-air interface on the apparent surface tension of aqueous solutions of hydrophilic solutes.* Colloids and Surfaces B: Biointerfaces, 2000. **19**: p. 147-162.

## Appendix A: Tips, Tricks, Superstitions, Unfinished and Supplemental Work

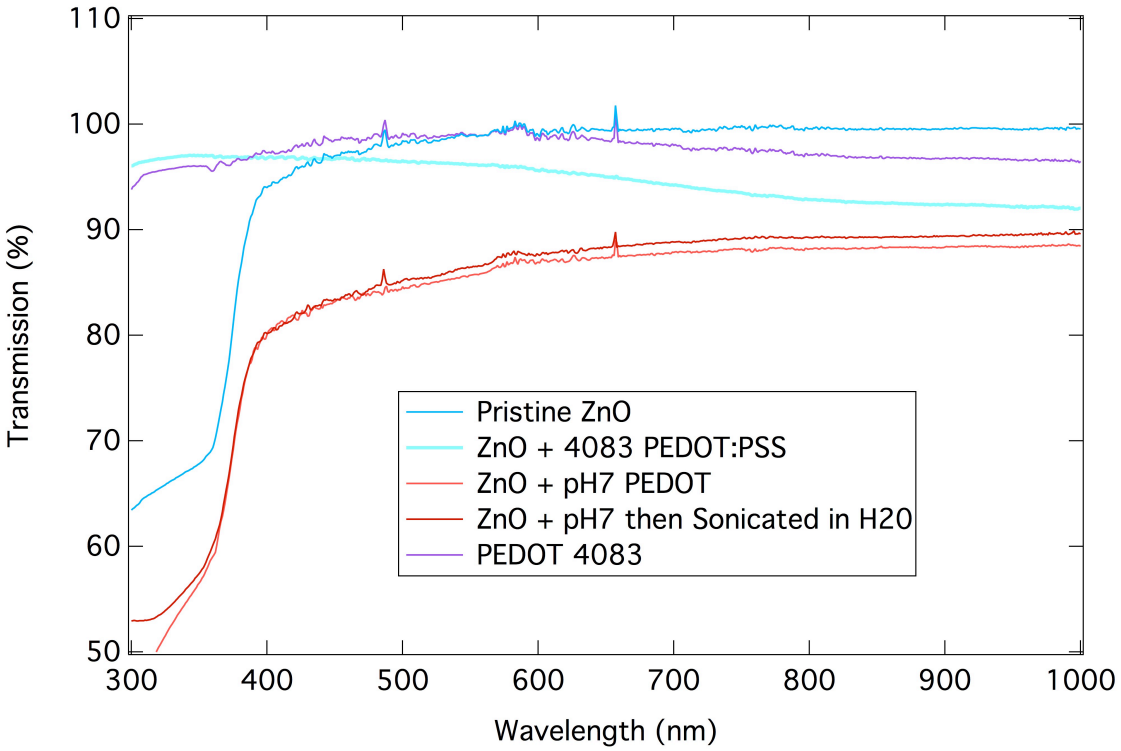


**Figure A.** UV-Vis Spectra of PEDOT:PSS over ZnO films. Note that the absorption cutoff associated with the band gap of ZnO at ~350 nm disappears when acidic PEDOT:PSS is spun over it, but remains intact when pH neutral PEDOT:PSS is used. Also note that PEDOT:PSS, when cured, is very resistant to sonication in water. This suggests useful barrier properties in terms of spinning subsequent layers.

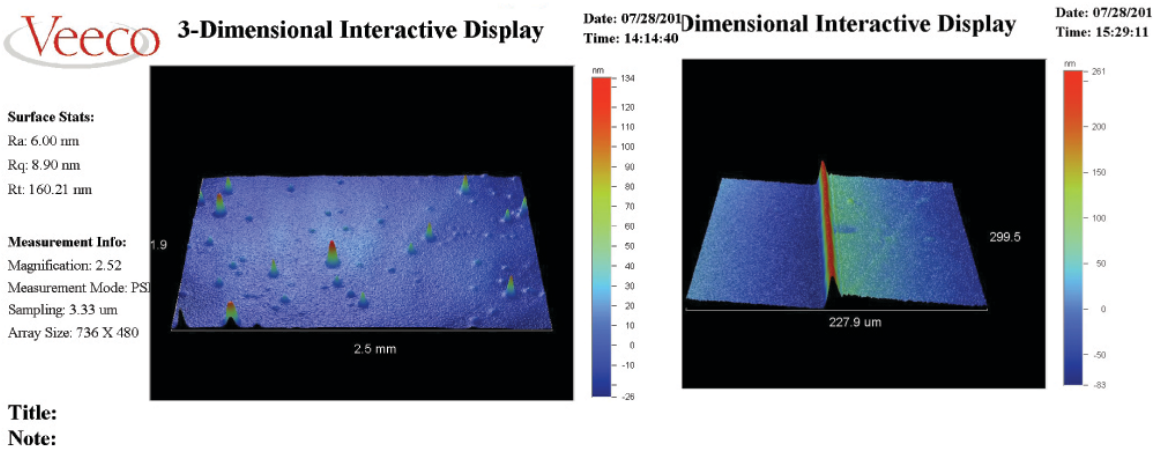


**Figure B.** Optical Profilometry of ZnO films with ~300 nm spikes and a ~ 300 nm ridge from wiping for patterning. These both caused shorting problems that were later solved with new precursors for ZnAc based ZnO and different patterning techniques (Razor and HCl after curing instead of ethanol before curing)

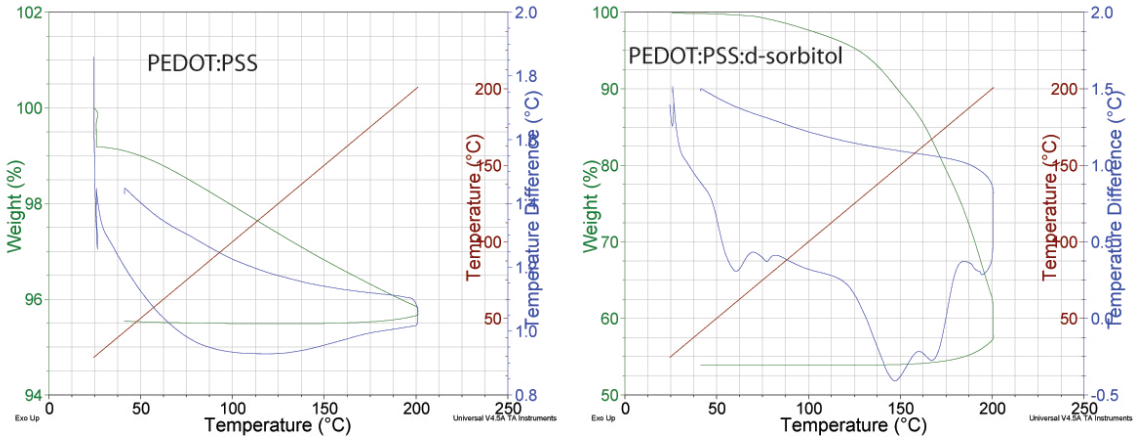


**Figure C.** TGA curves for PEDOT:PSS with and without 10% d-sorbitol added to the aqueous suspension. The PEDOT:PSS film loses ~ 5% of its mass, which is most likely water. The d-sorbitol added film loses ~53% of its mass although the film is 98% d-sorbitol by mass before heating. Mass loss accelerates at ~ 130 °C in the d-sorbitol film. The ramp process takes ~ 150 minutes to go from 30 °C to 200 °C, and back down to 50 °C, with ~ 60 minutes spent over 130 °C.

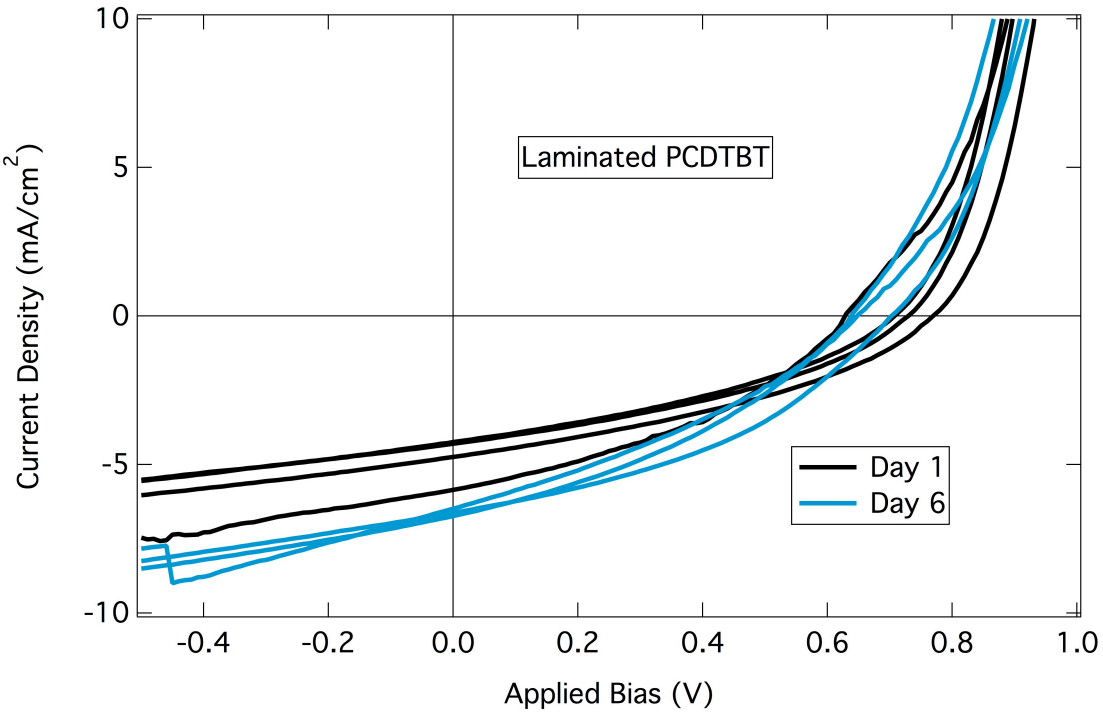


**Figure D.** Time evolution in dark ambient conditions for inverted laminated PCDTBT devices. Although controls were poor and a complete study wasn't done, PCDTBT devices were successfully made with lamination. Identical P3HT:PCBM devices and evaporated contact PCDTBT devices failed (most were shorted or <0.5% PCE) by comparison.

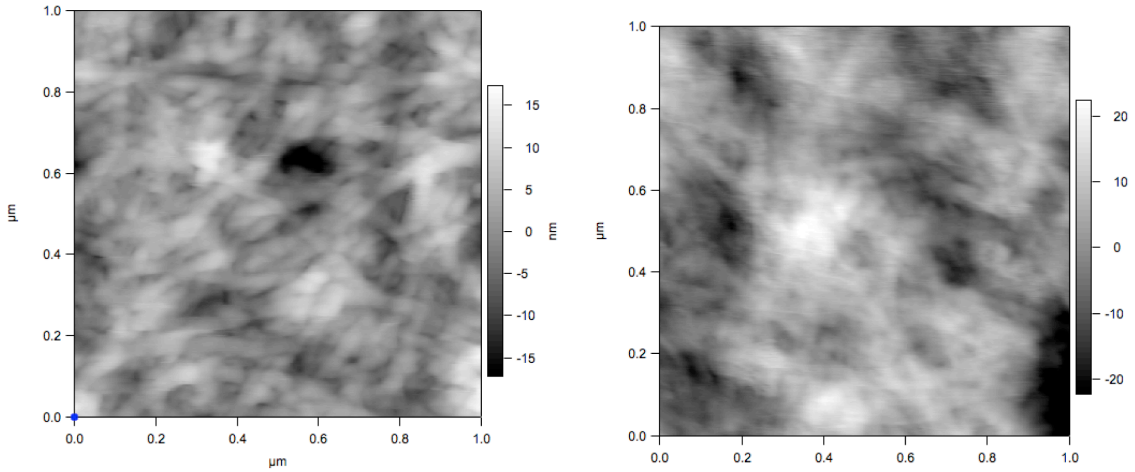


**Figure E.** AFM height traces of SWCNT electrodes without any adhesive (left) and coated with PEDOT:PSS:d-sorbitol (right)

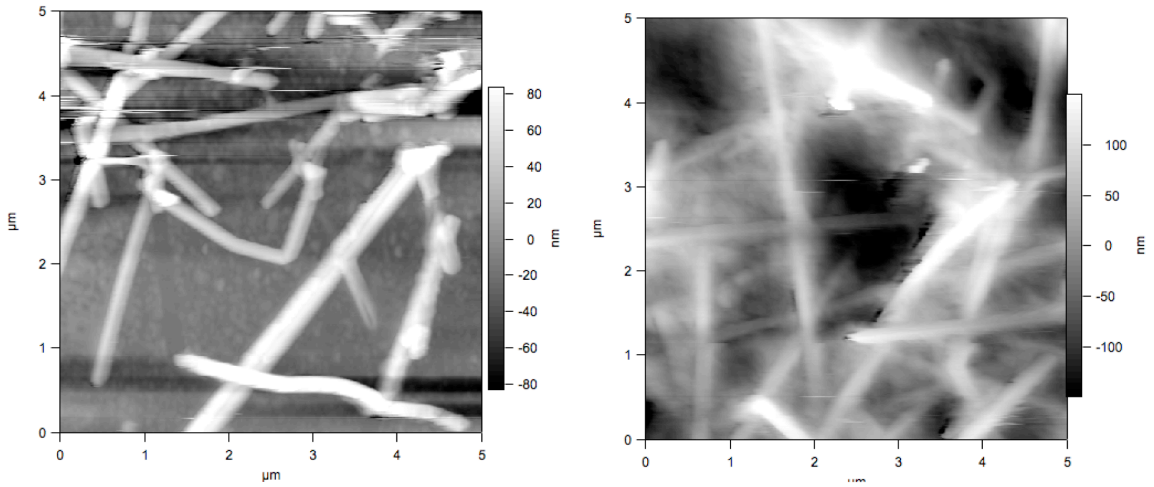


**Figure F.** AFM height traces of AgNW electrodes without any adhesive (left) and coated with PEDOT:PSS:d-sorbitol (right)

**Tips & Tricks:**

**1. Patterning of Highly Conductive PEDOT:PSS:d-sorbitol layers**

PEDOT:PSS:d-sorbitol is very conductive, conductive enough to act as an electrode as shown in this dissertation. As a result, the active area of the device has been defined by an aperture. Although aperturing reduces the light collecting area of the device, it does not change the dark area of the device or eliminate "crosstalk" between devices.

Increased dark area can negatively affect the $V_{oc}$ of the cell. Since $V_{oc}$ occurs when $J_{net} = 0$. This is at the balance between reverse photoinduced current and forward leakage current. Increasing the dark area relative to the light area allows for increased leakage current, and reduces the open circuit voltage of the device.

Crosstalk can cause one short on the substrate to ruin the performance of all 6 devices. The highly conductive PEDOT:PSS:d-sorbitol layer effectively shorts all of the devices to each other. This is not a large problem if the entire substrate is an effective diode, but it can one defect that is or is not part of a device can ruin the entire substrate of 6 devices.

One solution to the problems associated with highly conductive layers is to carefully pattern them to isolate devices from each other. Given the geometry used specifically in this work: If the conductive layer is on the PET, a very fine watercolor paintbrush dipped in water can be used to "paint" lines to remove PEDOT from between the electrodes. Using a digital multimeter to measure resistance between adjacent electrodes (ideally infinite), resistance values increase from tens of kΩ to hundreds of MΩ when this paintbrush method is used immediately after spinning PEDOT:PSS:d-sorbitol. If two spins are necessary, the paintbrush method is used after each spin, before annealing the film. If the conductive layer is on the ITO racetrack, a razor can be used to scrape lines to isolate the devices. Due to the layout of devices on the substrate, the pattern shown by red lines on the right side of figure E is the most effective way to isolate the devices while minimizing risk of running a razor through the active area of a device. Due to the alignment of the top and bottom substrates, one cannot tell if scraping the bottom substrate will harm a device until after the device is completed.

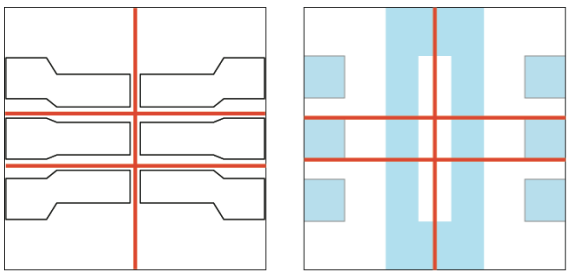

**Figure G.** Paintbrush wiping (left) and razor scraping (right) patterns for isolating devices with highly conductive layers.

**2. Lamination Procedure Step by Step**

1. Cut Squares of PET or PEN using a paper cutter. Both work about equally well, but our group's PET was quite scratched, while the PEN was much smoother. Make the squares slightly less than 1 inch square, so that they fit more easily in the evaporator spaces for 1 - inch samples. Try to maintain a "clean" and "dirty" side for the squares, so that scratches don't affect the quality of the silver film later.

2. Evaporate 150 nm of Ag onto the PET squares. The thicker film is more robust to the scraping and patterning that will follow. In order to keep the flexible substrates pressed against the shadow mask, place 1-inch aluminum blocks over the films in the evaporator substrate holder. If not, the flexible substrates will likely curve away from the mask, and edges will be hazy due to the distance between the mask and the substrate.

3. Mix 4083 PEDOT with 10% d-sorbitol by weight. This will dissolve overnight in the refrigerator. Spin this mixture over the Ag film twice at 2000 RPM. Wipe with a watercolor paintbrush dipped in water between spins and after the 2nd. Anneal at 115 °C for 10 minutes.

4. Before lamination cut 4 edges off of the plastic substrate. Draw 3 parallel lines on a sheet of paper that are each 0.42 inches apart. Place the substrate on the page with the centerline of the 6-finger pattern over the center line on the paper. Mark the edges of the substrate where the other 2 lines intersect the PET. Cut the edges off of the 6-finger mask based on these guides. Cut parallel to the ends of the 6 finger pattern as well. See figure E below.

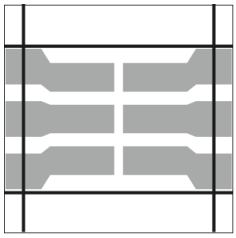

**Figure H.** Cutting guide for PET films for lamination. The vertical lines are 0.42 inches from the centerline. The horizontal lines are cut guided parallel to the edges of the evaporated electrodes.

5. Prepare the Glass/ITO substrate the same as for an evaporated device.

6. Lamination Step: Align the center finger of the 6 finger pattern with the center ITO pad on the ITO substrate and use thumb pressure to prevent the top substrate from shifting. Laminate between 2 silicon rubber pads with PTFE release films over each pad. Use a lamination press pre heated to 130 °C for 5 minutes at 275 pounds of force.

7. Use silver paint to paint over the intersection of the electrodes and the outside ITO pads on the glass substrate. This should allow for contact with a standard measurement puck.

### 3. Zinc Oxide from Zinc Acetate Superstitions

ZnO is a very complex material with many different parameters dictating its behavior in an OPV devie: Crystallinity, band structure, doping density, defect density, carrier density and doubtless others. Measuring and controlling these parameters is not the focus of this thesis, but producing consistent quality films is a necessary step to producing efficient and reproducible devices. Without performing a scientifically controlled study, it is the author's opinion that the following parameters are important for high quality and reproducible ZnO layers using the previously referenced zinc acetate sol-gel method for the purpose of making electron selective layers on ITO for OPV devices.

Precursors:

If stored in a desiccator, the zinc acetate crystals do not absorb a measurable amount of water. Even so, heating the powder to 120 °C before liquids are added may drive away any residual moisture from the glass vial or the zinc acetate. Measuring the weight of the crystals/vial before and after heating did not show any differences.

Monoethanolamine will turn yellow if exposed to air on the time scale of months. While the mechanism of this change is unknown to the author, using freshly purchased monoethanolamine eliminated problems of devices shorting, most likely due to ZnO chunks poking through other layers of the device. Preserving the airtight diaphragm on the stock container and opening the container minimally slowed the yellowing of the liquid.

2-Methoxyethanol does not show any visible changes over time, but it was replaced along with the monoethanolamine, and may also contribute to decreased device performance as it ages.

Preparation:

Vials are spun tightly sealed for ~ 1 hour before deposition. When spin coating, care is taken to reduce the occurance of bubbles in the solution. Bubbles can cause visible film defects upon spin coating, known as "comets" to some. Films are annealed on a hot plate preheated to 300 °C. Experience shows that ramping the temperature of the sample from 200 °C to 300 °C results in degraded device performance.

Patterning: See Figure A. Wiping with ethanol before annealing resulted in the ~300 nm ridges shown. Scraping with a razor both before and after the anneal helped solve problems associated with shorting, but no "after" images were taken.